2-D and 3-D tools for electrical imaging in environmental applications

POLITECNICO DI TORINO

Dottorato in Ambiente e Territorio

Georisorse e Geotecnologie

XXV Ciclo

TESI DI DOTTORATO

"2-D and 3-D tools for electrical imaging in environmental applications"

Tutore:

Prof. ALBERTO GODIO

Candidato:

Ing. Alessandro Arato

Aprile 2013

Acknowledgements

After these three years of PhD experience, there is a certain number of people I would like to thank.

Foremost, my gratitude goes to my advisor, Prof. Alberto Godio, for having shared his knowledge with me during these three years with patience, motivation and stimulating discussions. He accepted my application to the PhD program here at Politecnico di Torino, indirectly opening a very special period with all the fellows of the group of Applied Geophysics (and the department in general).

I would also to thank some important people, with whom I worked on most of the material presented in this thesis. In order of "appearance": Prof. Luigi Sambuelli, Dr. Andrea Borsic, Dr. Alberto Villa, Dr. Markus Wehrer and Prof. Borbala Biró. You will sometimes read, scrolling throughout the thesis, some sentences starting with "We tested...", "We performed...", "We have applied...". I intentionally decided to leave the plural form because I cannot attribute all the thoughts and work to myself and, in fact, most of the work presented in this thesis will be published in different forms with their co-authorship.

Of course, I can't omit the beautiful experience with all *SoilCAM* people I met during these years at meetings, conferences, and field activities. We shared poster sessions and focus groups, rain and sun, mud and oil, pizza and wine.

A huge GRAZIE goes to my colleagues, starting from Diego and all the field work we have done together (and, of course, all lunches at *Bella Riva*, some curious discussions with truckers at *le due pazze* and some polenta on the alpine glaciers), and going to Paolo, Flora, Roberto Bruno, Stefano, Daniele, Margherita, Corrado, Ema, Ken, Silvia, Erika, Sylvester, Federico, Prof. Valentina Socco and Dr. On. Cesare Comina. We shared an innumerable quantity of coffees and pauses, soccer matches, bottles of good and "aged" wine, a lot of laughs and, why not?, important advices on Matlab tools that were completely unknown to me.

The final part of the acknowledgements is for the most important people. ALL OF MY FRIENDS, my family and Roberta, who I literally share my life with. Their daily support is unconditional and selfless, and their love is the most important thing for me.

Summary

Introduction

This work is focused on the characterization of sedimentary soils affected by contamination, and on the monitoring of the evolution of contaminant distribution and properties over space and time. Within this initial purpose, geo-electrical and electromagnetic techniques have been used and analysed. More specifically, bi-dimensional (2-D), tri-dimensional (3-D) and time-lapse (4-D) geo-electrical methods make up the core of the work presented in this thesis.

The traditional electrical resistivity measurements originate in the 1910s, with the famous works on resistivity soundings by Schlumberger and Wenner. Since then, use of geoelectrical methods have increased, due to their effectiveness in providing useful information about subsoil in many different applications (e.g. mineral exploration, hydrogeological characterization at shallow depth).

Tomographic methods (i.e. Electrical Resistivity Tomography, ERT) hugely came up since the early 1980s (e.g. Barker, 1981) when proper instrumental devices and computing facilities were developed, allowing geophysicists to perform 2-D electrical resistivity surveys with reasonable effort, in terms of both time consumption and computation costs. The possibility to get more detailed information, and the further development of cross-hole methods, made ERT a desirable technique even for environmental applications. Hydrogeophysical studies have been conducted to monitor flow and transport of water and contaminants in the vadose zone (e.g. Cassiani et al., 2006), in aquifers and fractured rocks (e.g. Daily et al., 1992, Binley et al., 1996, Slater et al., 1996, 1997), to delineate contaminant plumes (e.g. Daily et al., 1995), and to follow the evolution of remediation processes in contaminated sites (e.g. Ramirez et al., 1993, LaBrecque et al., 1996c).

The joint use of electrical resistivity and Induced Polarization (IP) methods have been used in a variety of situations concerning contaminated cases (e.g. Mazác et al., 1990; Benson and Stubben, 1995; Grumman and Daniels, 1995; Atekwana et al., 2000), exploiting the possibility to detect contaminant as well-recognisable geophysical anomalies. In fact, the principal phenomena which underlie the physical phenomena of electrical conduction and polarization in soils are well known at present. Inversion algorithms for the inversion of complex resistivity data have been developed (e.g. Kemna, 2000, De Bacco, 2003) in the last decade, allowing to incorporate both the real and imaginary components of the resistivity, respectively related to conduction and to polarization phenomena in the investigated medium.

However, the need to improve the resolution of resistivity imaging technique without stressing the intrinsic under-determination of the geo-electrical problem, and to provide more robust results in integrated characterization approaches, guided the work presented in this thesis to works on both “static” 2-D and 3-D problems, and on the inversion of time-lapse data. In addition, joint characterization of contaminated site has been carried out together with chemico-physical and biological analysis.

Grid manipulation techniques have been explored and adapted to the inversion of geo-electrical data, in order to solve inversion of resistivity data set trying to improve space resolution without decaying the robustness of the inversion process. Furthermore, in order to provide a mathematically flexible algorithm for inversion of complex resistivity data, a software based on the Primal-Dual method, through which the user can decide to use either the L1- or the L2- norm on both the data and regularization term of the objective function, has been created and tested.

Strategies related to the inversion of electrical resistivity and IP data have been developed with the aim of improving the interpretability of the results both in space and in time. These activity are part of a common effort for achieving an integrated characterization of contaminated sites, jointly with chemico-physical analysis of soils and groundwater and with measures of presence and degradation activity of hydrocarbon-degrading biomass.

This thesis is aimed to provide a methodological approach to inversion of 2-D and 3-D electrical resistivity data, in a variety of possible situations. However, most of the experimental activity presented in the various chapters has been carried out on data coming from a hydrocarbon-contaminated site, within the framework of the EU FP7 SoilCAM project. The application to data coming from a challenging test-site strengthens the confidence in the techniques developed in this thesis.

Description of Trecate site

The contaminated site treated in this thesis is located near the town of Trecate, in North-West of Italy. The Trecate area is characterised by fluvio-glacial and fluvial deposits, made up of a thick sequence of poorly sorted silty sands and gravel in extensive lenses. An artificial layer of clayey-silty material, less than 1 m thick, which was originally placed as a rice paddy liner, covers most of the site.

The shallow aquifer at the Trecate site comprises an extensive, unconfined sand and gravel unit in excess of 60 m thick beneath the site. The regional groundwater flow is influenced by the

previously described local conditions, because of the recharge, which occurs through the water infiltration from irrigation channels and rice-paddies, and because of the horizontal outflow, which is influenced by the drainage taken by the Ticino river, located in the Eastern direction 20 m below the elevation of the surrounding areas.

In 1994, the site was subjected to a crude oil spill as a result of a well blow out from an ENI-Agip operated exploration well, designated Trecate 24 (TR24). Details of the incident, which resulted in approximately 15,000 cubic meters of middleweight crude oil being released onto the surface and which contaminated both the soil and groundwater, have been reported elsewhere, together with descriptions of the subsequent site remediation (Reisinger et al., 1996, Brandt et al., 2002). After the accident, most of the oil was quickly collected and disposed of, but some infiltrated into the subsurface and reached the groundwater table. The oil mainly infiltrated where the clay liner was weak or absent, particularly at some rice paddy infiltration pits. On-site washing and thermal treatment of the soil was performed to speed up the soil remediation.

A permanent monitoring network was installed for groundwater control. The temporal evolution of the soil and the groundwater pollution has been assessed by conducting two field surveys per year, using direct-push technology to collect soil samples.

NAPL lenses have been detected floating on the water table since the blow-out occurred. The main hydrocarbon contamination zone covers approximately 96,000 m^2 and is characterized by an anoxic, electrochemically reductive groundwater plume (Burbery et al., 2004).

High contamination has been found both in soil samples (with TPH concentration values up to 500 mg/kg) and in the groundwater (TPH concentration > 10 mg/l).

Organization of the thesis

The first chapter gives an introduction about the geo-electrical problems, both from a theoretical and a practical point of view. It introduces the physical laws which govern the electrical and electromagnetic phenomena discussed in the thesis, the possible interpretation of the results, the measure of field parameters and the theory on inversion of electrical resistivity data.

In the second Chapter a novel approach, called Staggered Grid Electrical Resistivity Tomography, is presented. It is based on the manipulation of Finite Element Model grids and it works in a different way over homogeneous resistivity zones and across zones of high resistivity gradient. Thus, the user can check for the reliability of the resulting resistivity image, and even detecting more accurately the presence of resistivity boundaries.

The third Chapter focuses on the development of a software for the inversion of 2-D and 3-D complex resistivity data. The code, developed jointly with Dr. A. Borsic (Dartmouth College, New Hampshire), is implemented on the Primal-Dual Interior Point Method (PDIPM), which gives the user a high mathematical flexibility and allows to reduce the sensitivity of the inversion process to the presence of outliers in the data and to preserve sharp resistivity edges, where present. Furthermore, adaptive Finite Element meshing with the possibility to model the electrodes with a finite size allows a more rigorous solution of the direct problem.

An extension of the SGERT method is presented in the fourth Chapter, which deals with time-lapse inversion of resistivity data. Static SGERT technique is combined with the Difference inversion method (LaBrecque and Yang, 2001) to improve the quality of time-lapse results and to give additional information on the reliability of time-lapse results.

The fifth Chapter shows the results of a long-term geo-electrical, chemico-physical and biological monitoring at the hydrocarbon-contaminated site of Trecate (NO, Italy). The geophysical 1-D and 2-D characterization is supported by direct measurements of the most important chemico-physical parameter of soil and groundwater samples, and by laboratory experiments to check the presence of biomass and its degrading activity.

References

Atekwana, E. A., Sauck,W. A., Werkema, D. D., 2000. Investigations of geoelectrical signatures at a hydrocarbon contaminated site. J. Appl. Geophys., 44, 167–180.

Barker, RD., 1981. The offset system of electrical resistivity sounding and its use with multicore cable. Geophy. Prosp., 29, 128-143.

Binley, A., Shaw, B. and Henry-Poulter, S., 1996. Flow pathways in porous media: electrical resistance tomography and dye staining image verification. Meas. Sci. Technol., 7, 384–390.

Benson, A. K., Stubben, M. A., 1995. Interval resistivities and very low frequency electromagnetic induction—An aid to detecting groundwater contamination in space and time: A case study. Environmental Geoscience, 2, 74–84.

Brandt, C.A., Becker, J.M., Porta, A., 2002. Distribution of polycyclic aromatic hydrocarbons in soils and terrestrial biota after a spill of crude oil in Trecate, Italy. Environ. Toxicol. Chem., 21, 1638–1643.

Burbery. L., Cassiani. G., Andreotti. G., Ricchiuto. T., Semple. K.T., 2004. Single-well reactive tracer test and stable isotope analysis for determination of microbial activity in a fast hydrocarbon-contaminated aquifer. Environ. Pollut., 129, 321–330.

Cassiani, G., Bruno, V., Villa, A., Fusi N., and Binley, A. M., 2006. A saline tracer test monitored via time-lapse surface electrical resistivity tomography. Journal of Applied Geophysics, 59, No. 3, 244-259.

Daily, W.D., Ramirez, A.L., LaBrecque, D.J., Nitao, J., 1992. Electrical resistivity tomography of vadose water movement. Water Resources Research, 28, 1429-1442.

Daily, W., Ramirez, A., LaBrecque, D., Barber W., 1995. Electrical resistance tomography experiments at the Oregon Graduate Institute. Journal of Applied Geophysics, 33, 227-237.

De Bacco, G., 2003. Tomografia di resistività complessa:soluzione del problema diretto e inversoper applicazioni ingegneristiche egeologico-ambientali. PhD thesis.

Grumman,D. L., Daniels, J. J., 1995. Experiments on the detection of organic contaminants in the vadose zone. Journal of Environmental and Engineering Geophysics, 0, 31–38.

Kemna, A., 2000. Tomographic inversion of complex Resistivity. Theory and application. PhD Thesis. Der Andere Verlag.

LaBrecque, D. J., Ramirez, A.L., Daily, W.D., Binley, A.M., Schima, S., 1996c. ERT monitoring of environmental remediation processes. Meas. Sci. Tech., 7, 375-383.

La Brecque, D. J., Yang, X., 2001. Difference inversion of ERT data: a fast inversion method for 3-D in situ monitoring. Journal of Environmental and Engineering Geophysics, 6, 83–89.

Mazác, O., Benes, L., Landa, I., Maskova, A., 1990. Determination of the extent of oil contamination in groundwater by geoelectrical methods. In Ward , S. H., Ed., Geotechnical and environmental geophysics **II**: Society of Exploration, Geophysicists, 107–112.

Ramirez, A.L., Daily, W.D., LaBrecque, D.J., Owen, E., Chesnut, D.,1993. Monitoring an underground steam injection process using electrical resistance tomography. Water Resources Res., 29, 73-87.

Reisinger, HJ., Mountain, SA., Andreotti, GD., Porta, A., Hullman, AS., Owens, V., Arlotti, D., Godfrey, J., 1996. Bioremediation of a major inland oil spill using a comprehensive integrated approach. Proceedings of the 3rd International Symposium of Environmental Contamination in Central and Eastern Europe Warsaw Florida State University.

1. Theoretical Background

1.1 Physical Principles

The theory behind electrical resistivity methods is based on the Maxwell's Equations. They provide a comprehensive description of the macroscopic electromagnetic behaviour of a medium.

The electric and magnetic fields are both described by their intensity, respectively:

$$\nabla \times \mathbf{E} = -\frac{\partial \mathbf{B}}{\partial t} \tag{1.1.a}$$

$$\nabla \times \mathbf{H} = \mathbf{J} + -\frac{\partial \mathbf{D}}{\partial t} + \mathbf{J_s} \tag{1.1.b}$$

where **E** and **H** are, respectively, the electric and magnetic field intensity, **B** is the magnetic induction, **J** the conduction current density, **D** the electric displacement and $\mathbf{J_s}$ a general current source into the medium.

Equations (1.1) are related each other and can be simplified under the assumption of a linear, isotropic and time-invariant medium, in frequency domain:

$$\mathbf{J} = \sigma(\omega) \cdot \mathbf{E} \tag{1.2.a}$$

$$\mathbf{D} = \varepsilon(\omega) \cdot \mathbf{E} \tag{1.2.b}$$

$$\mathbf{B} = \mu \cdot \mathbf{H} \tag{1.2.c}$$

where σ(ω) and ε(ω) are, respectively, the electric conductivity and the dielectric permittivity, function of angular frequency ω, and μ the magnetic permeability.

The electromagnetic field which is generated by an alternating current through a medium can be expressed as a function of the complex exponential $e^{i\omega t}$, resulting in:

$$\nabla \times \mathbf{E} = -i\omega\mu\mathbf{H} \tag{1.3.a}$$

$$\nabla \times \mathbf{H} = (\sigma(\omega) + i\varepsilon(\omega) \cdot \omega)\mathbf{E} + \mathbf{J}_s \tag{1.3.b}$$

At low frequencies, when f=ω/2π < 10 kHz as in the case of electrical resistivity surveys, the following condition is valid:

$$\frac{\omega|\varepsilon|}{\sigma} << 1 \tag{1.4}$$

Thus, electric conduction is the preponderant phenomenon and then the displacement current term **D** (in Equation 1.2.b), which regulates the propagation of electromagnetic waves at high frequency, can be neglected.

Conductivity σ, as the reciprocal of resistivity ρ, is then the physical property that governs current flow through the ground, as described by the Ohm's Law (Equation 1.2a).

Supposing **E** to be conservative, and in absence of magnetic perturbations, the electric field intensity is given as the gradient of the electric potential,

$$\mathbf{E} = -\nabla\Phi \tag{1.5}$$

and the Ohm's Law can be rewritten as:

$$\nabla \cdot (\sigma(\omega))\mathbf{E} + \nabla \cdot \mathbf{J}_s = 0 \tag{1.6}$$

1.2 Petrophysical interpretation of geo-electrical parameters

This section is aimed to give a brief introduction to the physical phenomena that influence the resistivity response in most common geological soils.

Soils can be considered as multi-phase systems, consisting of solid grains and pores, which could be partially or totally filled by various fluids. Each phase is responsible, through its individual electrical properties, of the bulk resistivity of the formation which is going to be measured in the field. An important contribution also comes from the geometric arrangement of the solid matrix and the (non-) aqueous solution filling the inter-connected pores.

The flow of electric charges through the soil depend on electrolytic conduction, interfacial conduction and polarization mechanisms. Each of this term will be briefly treated in the following.

1.2.1 Electrolytic conductivity

Electrolytic conduction pertains to the movement of ions which are dissolved in the pore-filling fluid(s).

According to Kemna (2000), electrolytic conduction can be expressed with the term σ_{el}, firstly described by Archie (1942) and dependent on conductivity of the pore fluid solution σ_w, porosity Φ and fluid saturation S_w :

$$\sigma_{el} = \frac{\Phi^m}{a} \cdot \sigma_w \cdot S_w^n \tag{1.7}$$

The empirical exponents “m” and “n” are related to pore cementation (thus to pore geometry) and to saturation, while “a” is a proportionality constant. $F=(\Phi^m/a)^{-1}$ is usually referred to as the Formation factor.

Dissolved ions are the main carriers of electrical charges, ionic concentration directly influences σ_w and, consequently, σ_{el}. Furthermore, the carrying capacity of the ions is influenced by their mobility and, thus, to temperature and viscosity of the pore-filling fluid(s).

1.2.2 Surface conductivity and membrane polarization

Electrolytic conduction has been shown, in the previous section, to be mostly influenced by pore volume properties. Another mechanism which contributes to the bulk conductivity is the surface conductivity, prevalently controlled by the physical and electrical properties of the interface between the pores and the soil matrix. More specifically, surface conductivity plays a significant role through the double electrical layer at the interface between grain surface and the electrolytic solution, both charged by the current flow.

The surface of most soil particles is surrounded by fixed electric charges, due to intrinsic properties of the minerals and even to depositional processes. A particularly important role is played by clay minerals, whose surface exhibit negative charges. The formation of the so-called double layer occurs from the attraction between negative surface charges on the grain surface and the cations dissolved in the liquid. The double diffused layer is then composed by the negative charged layer at the particle surface, a layer of adsorbed cations, and the diffused layer of mobile cations, whose concentration decreases exponentially with distance from the grain surface, as described by Grahame (1947). The distance between the diffused layer and the grain surface is sufficient for the cations to be mobilized and exchanged, adding charge carriers to the electrolytic solution and resulting in an additional ohmic conduction.

Besides the surface conduction part, the presence of the electrical double layer is responsible even for polarization mechanisms, also called membrane polarization. It occurs at the interface between interstitial fluid and grain surface, in correspondence of the double diffused layer. In normal conditions, ions are in casual movement into the fluid. When an electrical field is being applied to the ground, and in presence of fine-grained material such as silt and clay, the cation clouds of the diffused layer attract the free anions, acting as a selective membrane to the ion movement through the pores. This type of polarization, induced by the applied electric field, can be measured both in frequency and in time domain. Complex conductivity measurements are sensitive to surface electrical conductivity in their imaginary part, and they produce a phase delay (i.e. negative phase values) which depends on the capacity of the soil to store the electric charges (i.e. polarizability). The same phenomenon can be measured in time domain as the decay of the voltage after switching the current off. This decreasing voltage trend corresponds to a secondary flux of charges, that were previously "stored" by clay particles, following the mechanism explained above.

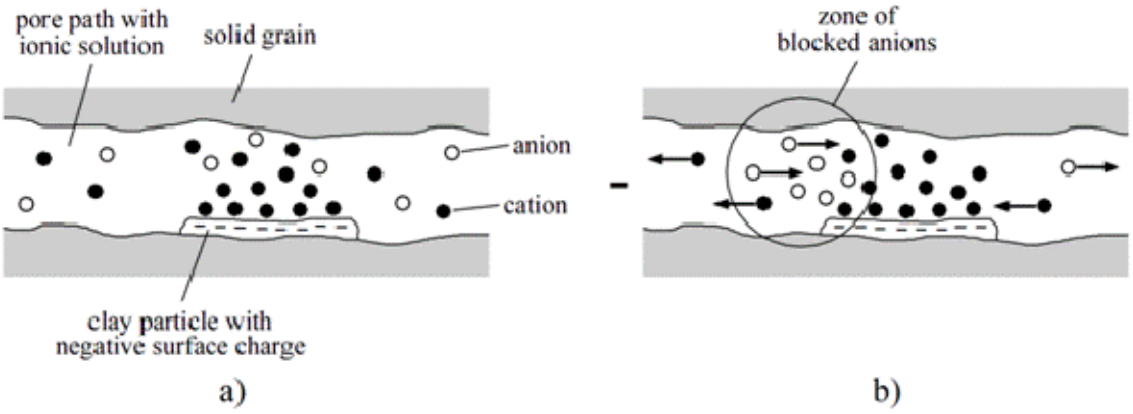

Fig. 1.1: Membrane polarization mechanism, with a) a double layer of cations around the clay particle. When an electric field is applied, b) the cation cloud blocks the anions, causing a polarization of the medium (after Kemna, 2000).

It is important to highlight that membrane polarization phenomena are not just a prerogative of clayey soils. According to Börner and Schön (1991), most common sedimentary soils containing fine particles produce analogous geophysical response, especially in presence of silicate minerals whose surface exhibits a negative surface charge.

Börner et al. (1996) defined the surface conductivity as a function of salinity $h(\sigma_w)$, pore specific surface S_s, formation factor F and fluid saturation S_w, through the following Equation:

$$\sigma_{int} = \frac{h(\sigma_w)S_{por}}{F} \cdot S_w^v \cdot (1 + il) \tag{1.8}$$

where $l=Im(\sigma_{int})/Re(\sigma_{int})$ varies in the range between 0.01 and 0.15 (Börner et al., 1996) and accounts for the separation between real and imaginary components of σ_{int}. The saturation exponent v has been found (Schopper et al., 1997; Kemna, 2000) to be correlated with the one of σ_{el} in Equation (1.5), via the relation $n-v\approx1$.

Waxman and Smits (1968) stated that the two conductivity component can be summed to obtain the measurable value of bulk conductivity $\sigma=\sigma_{el}+\sigma_{int}$. Although this assumption is supported by the description of the soil system as a parallel conductor circuit, a more realistic inference of the interfacial properties of the medium can be done by measuring the quadrature component of σ and, more in general, by measuring the occurring induced polarization phenomena.

1.2.3 Electronic conductivity

Another important phenomenon that should not be neglected is the possibility for solid matrix to play a role in the overall conduction. The presence of electrically conductive minerals such as, for instance, pyrite, magnetite, copper and iron from depositional activity, and graphite, causes electronic conduction, potentially increasing the bulk conductivity of the mineralized rock. The spatial distribution of metallic minerals can be distributed almost uniformly over the soil volume, forming preferential flow path for the free electrons, or can be concentrated in an isolated mass. In case of a well-disseminated arrangement of metallic particles, the charge carriers flow between grain to grain can only occur through the a double electrical layer which is formed between the metallic particles and the pore fluid. Marshall and Madden (1959) evidenced two main conduction mechanisms: the faradaic path, which guarantees the charge-transfer via oxidation and reduction reactions, and the non-faradaic path, which accounts for capacitive couplings between the grain surfaces. Caused by the application of an electric field, the interface between the mineral grain and the electrolyte fluid is involved in an accumulation of ions (Ward and Fraser, 1967), whose movement is directed to the diffused layer in the pore fluid. This produces a strong polarization effect, opposed to the applied electric field. This effect, referred to as electrode polarization, produces an IP response that is greater than the membrane polarization effect in most of the cases.

1.3 Field measurements and related geophysical parameters

Despite of the terminology used in the previous paragraphs, electrical resistivity is usually preferred to conductivity and will be used in the following. Field measurements of resistivity and induced polarization (IP) are carried out by a certain amount of quadripoles (i.e., four electrode arrangement), two of which used for current injection (i.e. current electrodes, or dipole), and the other two electrodes for measuring the potential drop (i.e. potential electrodes, or dipole) caused by the application of the electric field.

Resistivity and IP can be measured both in time- and in frequency domain. Both the methods allow to acquire datasets of electrical resistivity, the first one by relating the voltage response to the injected square wave current, whereas in the second method the voltage response to the application of a periodic sinusoidal current (frequency-modulated) is observed. Time-domain IP is obtained by measuring the voltage decay with time after switch-off of the injected current while, in frequency domain, soil polarization directly influence the phase shift between voltage and current signals.

1.3.1 IP measurements in time-domain

IP methods in time-domain refer to non-zero voltage response caused by switch off of an applied current into the ground. The observed voltage, depending on the polarization of the medium, does not immediately drop off to zero after shut-down of the primary voltage source, but to a value V_s (secondary voltage), lower than the primary voltage V_p being reached before current switch-off, but non-null. Seigel (1959) introduced the ratio between secondary and primary voltage as a descriptive quantity m, the chargeability:

$$m = \frac{V_s}{V_p} \tag{1.9}$$

Because of strong difficulty of determination of m in the field, m is preferred to the integral chargeability, that comes from:

$$M = \frac{1}{(t_2 - t_1)V_p} \cdot \int_{t_1}^{t_2} V(t)dt \tag{1.10}$$

where V_p is the primary voltage, and V(t) represents the voltage decay with time, to be integrated in the interval between t_1 and t_2.

M should be linearly related to the phase displacement from frequency domain resistivity measurements,

$$M \approx -\phi(\omega_0) \tag{1.11}$$

where φ is the phase shift between voltage and current signals measured at the reference frequency ω_0.

Kemna et al. (1997) deduced, on the basis of a constant-phase angle relaxation model with frequency exponent b, the following Equation:

$$V(t) \approx V_p \sum_{k=0}^{Np-1} (-1)^{N_p-k} \left[(t+2kT)^b - (t+T+2kT)^b \right] \tag{1.12}$$

This Equation gives the voltage response due to the application of N_p alternating current pulses, with 50% duty cycle and a pulse length equal to T.

1.3.2 IP measurements in frequency domain

A common method to describe IP effect in frequency domain refers to the dependence of electrical resistivity measure on the frequency, and is called frequency effect

$$FE = \frac{\rho_0 - \rho_\infty}{\rho_\infty} \tag{1.13}$$

where ρ_0 and ρ_∞ are the asymptotic magnitudes of complex resistivity at zero and infinite frequency, respectively. Since there are obvious physical limits in the determination of zero and infinite frequencies, ρ_0 and ρ_∞ are substituted with $\rho(\omega_0)$ and $\rho(\omega_1)$, being $\omega_0 < \omega_1$ two distinct and finite frequency, divided by at least a decade. Frequency effect can be also found under the form of a percentage frequency effect PFE

$$PFE = 100 \cdot FE \tag{1.14}$$

As described by Wait (1959), time- and frequency domain IP qualitative parameters m and FE can be related through

$$m = \frac{1+FE}{FE} = \frac{\rho(\omega_0) - \rho(\omega_1)}{\rho(\omega_0)} \tag{1.15}$$

Finally, as it was deduced by Wait (1984), the frequency effect can be related even to the phase angle at a reference frequency ω_R,

$$\mathrm{FE}(\omega_R) \approx -\phi(\omega_R) \tag{1.16}$$

where $\mathrm{FE}(\omega_R)$ is the incremental ratio of resistivity values measured at two different frequencies close to the reference one.

Another important parameter which contributes to explain IP phenomena il the so-called metal factor (MF), firstly introduced by Marshall and Madden (1959) as

$$\mathrm{MF} = \frac{\mathrm{PFE}}{\rho_0} \tag{1.17}$$

Hallof (1964) showed a reduced dependence of MF on electrolytic conduction phenomena within the medium, and this make it useful for mineral exploration. Knowing that, from Equation 1.16, PFE≈-φ, and φ ≈sinφ since usual measured angles in IP applications are around zero degrees,

$$\mathrm{MF} \approx |\sigma| \sin(-\phi) = \mathrm{Im}(\sigma) \tag{1.18}$$

As described in the previous paragraphs, imaginary component of complex conductivity is being attributed to IP phenomena regarding electronic conduction and electrode polarization and, hence, it doesn't belong to electrolytic conduction through the pore solution.

1.4 Inversion of electrical resistivity data

The solution of an inverse problem in geo-electrics is performed by specific inversion algorithms, through which the earth's subsurface is parameterized with a set of pixels (or voxels, in 3-D), each one being assigned of its individual resistivity value. By definition, inversion of electrical resistivity data is a ill-posed problem, which suffers from non-uniqueness of the solution and moreover by under-determination of the system of Equation to be solved. In the quasi-totality of the cases, the number of model elements (i.e., the pixels or voxels), which are the unknowns to be calculated, is much greater than the number of possible equations coming from the number of independent measured data.

Then, the inverse solution is obtained by adding physical or spatial constraints (sometimes from prior knowledge of geological, chemico-physical or geophysical features of the site), and resolving the system by the minimization of a model objective function that adequately describes the data.

2-D problems will be referred to as ERT (Electrical Resistivity Tomography) in the following, because of the spatial distribution of the electrodes which are usually placed to surround the target to be reconstructed. However, this is a pure simplification of the electric conduction phenomenon, that is influenced by the whole interested volume and is characterized by a diffusive behaviour (Kemna, 1996) and cannot be attributed to single paths, as it is usually done in common tomographic surveys.

The forward and inverse solution are implemented separately, the first one deals with the common differential equation through which the electric potential field, and thus injected currents and measured voltages, can be related to an arbitrary resistivity distribution in the subsoil

$$\nabla \cdot (-\sigma \nabla \Phi) - \lambda^2 \sigma \Phi = \mathbf{I}\left[\delta(r - r_{C^+}) - \delta(r - r_{C^-})\right] \tag{1.19}$$

where I is the input current, Φ the potential field, λ the Fourier transform along the y- direction, σ is the conductivity distribution in the subsoil, r_c^+ r_c^- are the positions of positive and negative current sources.

Usually the solution of this problem is given on a model of elements each one having a finite dimension, also referred to as Finite Element Model (FEM). Each element is attributed a constant electrical conductivity value.

The forward problem of Equation (1.19) is represented in matrix form as

$$\mathbf{G\Phi} = \mathbf{I} \tag{1.20}$$

where G is a NxN matrix (with N equal to the number of nodes in the FEM) representing the forward model, Φ is a vector containing the calculated potential at the nodes and I a vector of source currents.

Usually, Neumann and Dirichlet boundary conditions are applied, respectively, at ground surface and lateral and bottom boundaries of the model (e.g. LaBrecque et al., 1996; Kemna, 2000).

Since current really flows in 3-D, approximating it as a pure 2-D phenomenon results in a bad estimate of the potentials and thus to the final resistivity result.

Then, a “fictitious” extension of the potential distribution in the y- direction is done integrating over a set of λ (LaBrecque et al, 1996), the Fourier transform of the y- variable function of the distance from the survey line.

When formulating an inverse problem in geoelectrics the distribution of the electrical properties in a certain domain is discretized through a set of parameters, **m**, which is related to the measured data, **d**, through the relation:

d=*F(***m***)*, where *F* is the forward operator.

The goal of the inversion process is to find the resistivity distribution that is more consistent with the observed data, by means of the definition of an objective function to be minimized, usually with a least square formulation:

$$\boldsymbol{\Psi}_{\mathrm{d}} = \sum_{\mathrm{i}=1}^{\mathrm{N}} \left(\frac{\mathrm{F}_{\mathrm{i}}(\mathbf{m}) - \mathbf{d}_{\mathrm{i}}}{\varepsilon_{\mathrm{i}}} \right)^2 = \left\| \mathbf{W}_{\mathrm{d}} (\mathrm{F}_{\mathrm{i}}(\mathbf{m}) - \mathbf{d}_{\mathrm{i}}) \right\|^2 \tag{1.21}$$

where *N* is the number of measurements, d_i is the *i-th* observed resistance, F_i(**m***)* is the *i-th* resistance obtained through the forward solution and ε_i the variance of the *i-th* data (which is used to build the weight matrix $\mathbf{W}_d$).

In addition to the data objective function of Equation (1), a model objective function is then defined in order to incorporate a-priori information on geology of the area, introducing penalties for departure from an initial model and for anisotropy in the reconstruction:

$$\boldsymbol{\Psi}_{\mathrm{m}} = \alpha_{\mathrm{s}} \left\| \mathbf{W}_{\mathrm{s}} (\mathbf{m} - \mathbf{m}_0) \right\|^2 + \alpha_{\mathrm{x}} \left\| \mathbf{W}_{\mathrm{x}} (\mathbf{m} - \mathbf{m}_0) \right\|^2 + \alpha_{\mathrm{y}} \left\| \mathbf{W}_{\mathrm{y}} (\mathbf{m} - \mathbf{m}_0) \right\|^2 \tag{1.22}$$

where the first element is the penalty for the deviation from a starting model m_0, the second and third terms are penalties for roughness in *x*- and *y*- direction, and the α's are the smoothing factors.

Then, the total objective function can be expressed as:

$$\boldsymbol{\Psi} = \boldsymbol{\Psi}_{\mathrm{d}} + \boldsymbol{\Psi}_{\mathrm{m}} \tag{1.23}$$

and the search for the distribution of **m** that better suits the data is done iteratively, minimizing the following Equation with a Gauss-Newton approach:

$$\left(\mathbf{J}_{\mathrm{k}}^{\mathrm{T}} \mathbf{W}_{\mathrm{d}}^{\mathrm{T}} \mathbf{W}_{\mathrm{d}} \mathbf{J}_{\mathrm{k}} + \alpha \mathbf{W}_{\mathrm{m}}^{\mathrm{T}} \mathbf{W}_{\mathrm{m}} \right) \Delta \mathbf{m}_{\mathrm{k}} = \mathbf{J}_{\mathrm{k}}^{\mathrm{T}} \mathbf{W}_{\mathrm{d}}^{\mathrm{T}} \mathbf{W}_{\mathrm{d}} \left[\mathbf{d} - \mathrm{F}(\mathbf{m}_{\mathrm{k}}) \right] - \alpha \mathbf{W}_{\mathrm{m}}^{\mathrm{T}} \mathbf{W}_{\mathrm{m}} \left(\mathbf{m}_{\mathrm{k}} - \mathbf{m}_0 \right) \tag{1.24}$$

where *J* is the Jacobian, or "sensitivity" matrix, and $m_{k+1}=m_k+\Delta m_k$ is the updated model.

The solution of the problem is affected by a resolution of the model that is not constant throughout the investigated domain. The elements of the sensitivity matrix, $\mathrm{J}_{\mathrm{jk}} = \frac{\partial \mathrm{F}_{\mathrm{j}}(\mathrm{m})}{\partial \mathrm{m}_{\mathrm{k}}}$, quantify the change in the *j-th* forward-calculated resistance which is due to a unit change of the

k-th model parameter. The cells located near the electrodes are obviously very sensitive, in the sense that a variation in those resistivity parameter have a great influence on the measured data. This comes from the rapid changes of the electric field in there. Far from the electrodes the model becomes less sensitive, and the data vector cannot significantly change after a change in the resistivity of those cells.

A way to take into account for the variation of the sensitivity in the investigated domain is to refer to the model resolution matrix **R**, which relates the parameter vector **m** to the true parameter vector $\mathbf{m}_{true}$ through: $\mathbf{m}=R\cdot\mathbf{m}_{true}$, and can be expressed as:

$$\mathbf{R} = \left(\mathbf{J}_k^T\mathbf{W}_d^T\mathbf{W}_d\mathbf{J}_k + \alpha\mathbf{W}_m^T\mathbf{W}_m\right)^{-1}\mathbf{J}_k^T\mathbf{W}_d^T\mathbf{W}_d\mathbf{J}_k \tag{1.25}$$

In an ideal case, where **m** equalizes $\mathbf{m}_{true}$, *R* corresponds to the identity matrix.

Due to smoothing and in case of poor sensitivity, the terms on the diagonal are less than the unity and non-diagonal terms of **R** are no longer equal to zero. Thus, the final reconstructed model is a smoothed approximation of the true model.

Calculating **R** requires great computational expense so that other way to get information about the sensitivity of the model were evaluated, like the quantity *s* (Kemna, 2000):

$$\mathrm{s} = \mathbf{J}_k^T\mathbf{W}_d^T\mathbf{W}_d\mathbf{J}_k \tag{1.26}$$

which presents large values in correspondence to high sensitivity zones.

1.4.1 2-D inversion

2-D inversion of electrical resistivity for near surface data is a well known technique; different inversion schemes have been adopted over the years and adapted to tackle specific tasks in hydrogeophysics and in near surface investigation (e.g. Godio and Naldi, 2003, Kemna et al., 2004). Moreover, 2D inversion softwares for ERT data processing have been previously used in other special contexts: Sambuelli et al. (2003) inverted data from an ERT survey performed on living trees to search for inner wood decays and Comina and Sambuelli (2012) inverted fast ERT data acquired across a water stream in order to detect fluoresceine flow within an agricultural canal section. Coupled or joint inversion of resistivity and electromagnetic data is also becoming a viable approach in surveying near surface features (e.g. Godio and Naldi, 2009, Godio et al. 2010, Bastani et al., 2012, Bouchedda et al., 2012). The reliability of application of 2D and 3D modeling and inversion via time-lapse electrical resistivity tomography in monitoring the hydrologic soil parameters is discussed by several authors (e.g. Godio and Ferraris, 2005, Cassiani et al., 2006,

Cassiani et al., 2009). On the other hand, high resolution geophysical surveys are a well promising tool in complex environments (e.g. marine investigation) and require careful analysis of sensitivity and control of meshing in the inversion process (Strobbia et al., 2006).

In a 2-D problem, the resistivity parameters correspond to the resistivity value of each cell, or group of cells, in the considered finite-element discretization. The parameter in each cell is assumed to be constant. For this reason, the choice of a good discretization of the domain is a critical aspect and the reliability of the result is affected even by the chosen mesh. The traditional approach used for the inversion process consists of selecting a single grid of finite elements that is supposed to be "the best" one, and inverting the dataset on it. This grid can either be regular or irregular, or it can be set in accordance with the different sensitivity of the model, increasing the cell size while going farther from the electrodes (i.e. in the middle of the section between boreholes). The optimal solution would be to invert on an ultra-fine grid, in order to get a super-resolution image of the resistivity distribution in the subsoil. This type of approach can introduce ambiguities due to the non-uniqueness of the solution of the non-linear, and highly under-determined, problem, as usually happens for inverse geo-electrical problem. A conventional way to minimize the non-uniqueness in solving ill-posed inverse problems is to damp or smooth the solution (e.g. Tikhonov and Arsenin, 1977). The damping factor and the smoothing operator are either chosen by trial and error or based on the relationship between the model variance and the solution variance (Inman, 1975; Lines and Treitel, 1984). These schemes deform the model resolution and make the inverse procedure biased since they affect not only the zones that are inadequately constrained by the data but the whole model. Application of conventional schemes for inversion of electrical data in 2D and 3D are well known (e.g. Godio and Naldi, 2003; Cassiani et al. 2009). Alternative approaches based on grid manipulation and on adaptive meshing (e.g. Rucker et al., 2010; Davis and Li, 2011; Godio et al., 2011) have been proposed to decrease the mismatch between the data distribution and the adopted parameterization in the tomographic procedure.

1.4.2 3-D inversion

The most complete characterization of the subsurface with electrical resistivity techniques can be achieved via the execution of three-dimensional Electrical Resistivity tomography. A full 3-D survey needs the acquisition of a huge number of measurements, extending the concept of in-line measurements with several cross-line measurements. Obviously, this type of survey requires a large experimental set-up, with a sufficient number of electrode to cover the survey area with enough spatial resolution. For this reason, and due to the challenging computational demand of a

large scale problem, full 3-D surveys gained popularity just in the last decade. A surrogate of the full 3-D method is the so-called pseudo 3-D resistivity imaging, which is done by inverting the resistivity data coming from several 2-D parallel acquisition lines as a unique 3-D dataset. The pseudo 3-D result can have a resolution comparable to the one from full 3-D method if the inter-spacing between the 2-D lines is not greater than the electrode spacing (Yang and Lagmanson, 2006). Since they are governed by the same physical laws, solution of 3-D resistivity problems are similar to the commonly used 2-D tomography. The most critical problem to be solved is the computation of the sensitivity matrix (i.e. the Jacobian), whose dimensions come from the number of model elements and the number of datum points, both great in 3-D problems. Among many works, Sasaki (1994), Ellis and Oldenburg (1994b), developed finite-element 3-D algorithms for inversion of 3-D resistivity data, approaching the inverse problem as a non-linear optimization problem to be solved with conjugate gradient method.

1.5 Use of a-priori information in electrical resistivity problems

A-priori information can be defined as all the information of a certain site which has been obtained independently by the results of our analysis. The use of previous knowledge into the inversion of electrical resistivity data is usually made with the aim of reducing the intrinsic non-uniqueness of the solution of the inverse problem. Any a-priori information about soil structure, positivity constraints, expected lower and upper parameter boundaries, can be incorporated into the objective function by appropriate weighting matrices. The use of a-priori information into the geophysical data inversion can bring a significant improvement in robustness of results and interpretation. On the other hand, it is worthy to remember that a-priori information, when available, needs to be the most accurate possible. Otherwise, by adding rough or imprecise information can obviously bring to instability of the inversion process and/or to a misleading of the results.

Taking Electrical Resistivity Tomography (ERT) as an example, it is necessary to say that all information available from other (non-)geophysical characterization techniques have to converted in an a-priori resistivity distribution. This a-priori resistivity can come from:

- geological stratification;

- porosity and pore fluid saturation;

- pore fluid(s) chemico-physical composition;

- results from previous ERT surveys or from other geophysical techniques.

Since electrical properties of a porous medium are a weighed sum of all the properties listed above, there are analytical Equations which can be used to obtain an initial value of bulk resistivity. Archie's Law (Archie, 1942) provides an estimate of bulk resistivity of sedimentary soils taking into account pore fluid resistivity, porosity and saturation, tortuosity of the pores and adding two coefficients, the exponents for pore cementation and fluid saturation. Archie's Law doesn't account for grain surface conductivity, and then it is valid on medium-coarse grained sediments. Other methods (Waxman and Smits, 1968; Rhoades and van Schilfgaarde., 1976, Rhoades, 1993) have been developed to consider also the surface conductivity, in case finer material are present (silt and clay). A specific term is added for the presence of clay and organic matter, which play a significant role in surface ion conduction and even in polarization effects.

A geological characterization is then necessary, and can be provided from laboratory analysis (granulometric curve definition, estimate of porosity value and cementation factor to be used in the analytical models) and from different geophysical method. Since laboratory analysis of soil samples can provide information on a vertical spot, lateral (even 3-D) variation of geological boundaries can be followed by Ground Penetrating Radar (both in single offset mode and in multiple offset mode), EM soundings (at shallow depth), nuclear magnetic resonance profiles and other geo-electrical data.

When having a cross-hole set up, apparent or real resistivity from in-hole logs can be interpolated in a 2-D section to provide a preliminary information of the vertical distribution of the electrical properties, even dough this information is punctual and the interpolation doesn't take into account the possible heterogeneities that can be present between the two holes.

From a chemico-physical point of view, a-priori information for the inversion (and even ground-truthing for the results) can be given by analysis of specific electrical resistivity of groundwater (or a mixture of water and miscible or non-miscible contaminant) in situ, on-site or in laboratory measurements. Furthermore, with the laboratory assessment of Cation Exchange Capacity (CEC) it is possible to investigate the capability of the soil to play a role itself in ion conduction, through cation exchange between double-diffused layer of clayey particles and the pore fluid. If high values of CEC are measured, then the soil has a significant grain surface conductivity, which comes from the presence of very fine soil types or organic matter. In laboratory estimation usually the CEC values are derived from the measurement of ion concentration on the soil sample (amount of H, Na, Mg, K, Ca ions). This can introduce an over-estimate of CEC in alkaline soils, where most of Na and Ca ions are not in correspondence of the exchange sites.

At hydrocarbon-contaminated sites the presence of a third phase (fourth within the vadose zone) increases the complexity of the problem to be assessed. Past studies (e.g. Sauck 2000; Marcak and Golebiowski 2008) showed that the distribution of LNAPL contamination into the subsurface can be divided into four main parts:

- dissolved phase within the saturated zone, corresponding to a contaminant plume that undergoes flow and transport processes into the aquifer;

- free phase within the partially saturated layer of the so-called smear zone (that corresponds to the zone of fluctuation of the piezometric surface);

- residual phase within the upper smearing zone (unsaturated);

- vapour phase within the vadose zone.

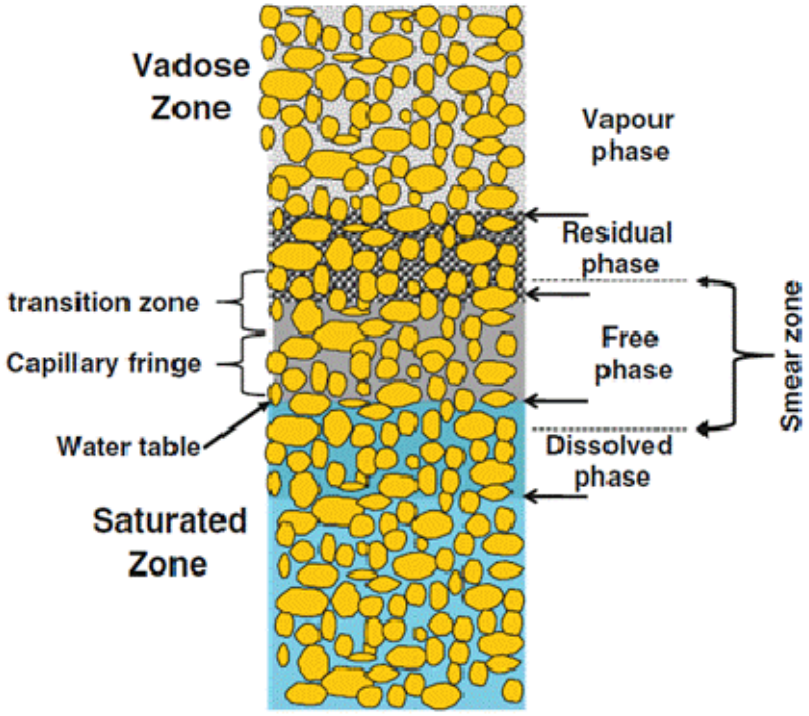

Fig. 1.2: Vertical distribution of soil moisture in presence of a LNAPL-contamination (after Atekwana et al. 2009)

The effect of the vapour phase can be neglected from a merely geo-electrical point of view, since it tends to migrate towards the surface and to be removed quite rapidly in the atmosphere. Anyhow, all the other three phases of the contamination have to be considered. The occurrence of a hydrocarbon contamination in a sedimentary soil produces a distinctive geo-electrical anomaly, since the Light Non-Acqueous Phase Liquid (LNAPL) components are characterized by extremely high resistivity values, in a broad range between 10^6 and 10^9 Ωm (Lucius et al., 1992;

Olhoeft, 1992). Therefore the presence of hydrocarbon phase should origin resistive anomalies at NAPL-contaminated sites.

However, in case of long-term contamination, the mature hydrocarbon could undergo bio-degradation, generating a conductive plume where ionic species and degradation by-products can be found. Most of the literature studies agree that aged hydrocarbon undergoing degradation results in a conductive plume, but there are some studies that associate strong NAPL contamination to resistive feature into the subsoil.

Quantitative information on the role of biomass degrading activity is difficult to obtain, and expecially to be converted in a useful parameter for geophysical data inversion. Studies on the effect of microbial activity at hydrocarbon-contaminated sites have shown decrease in bulk resistivity in correspondence to the contaminated locations and to the conductive plumes detected downstream. Interacting with the contaminant on the grain surface, degradation process is responsible for surface alteration and increase in surface conduction, effecting the resistivity and even more the induced polarization response (both in time-domain and in frequency domain).

Then, a valid model that explains the geophysical response accounting also for the presence of NAPL (and for biodegradation activity) has yet to be developed, because of the problems explained above and even because the smearing process increases the complexity of fluid distribution and saturation into the pore spaces, creating isolated blobs of NAPL and enhancing the spatial heterogeneity at the contaminated locations.

1.6 Application of Electrical Resistivity and Induced Polarization methods for contamination mapping and (bio-)degradation assessment

In the last decade, geophysicists have started to deal with influence of bacterial activity on the geophysical signature at contaminated sites. Thus, a new branch of geophysics has been developed, called “biogeophysics”, aimed at considering the biological activity as a source of alteration of the geophysical properties of a contaminated medium. A very comprehensive review of bio-geophysical methods and real cases experience was provided by Atekwana et al. (2010) with particular attention on sites that suffer from a Light Non-Acqueous Phase Liquid (LNAPL) contamination.

Being LNAPL a good organic source for biomass to grow, LNAPL contaminated sites can be considered as optimal situations for studying the geophysical response (mainly with electromagnetic methods) in presence of bacteria. However, the great variety of literature studies provides quite a high grade of disagreement about the results, leaving a open discussion about the relationships between the observed anomalies and the presence of contamination.

1.6.1 Hydrocarbon contamination of sedimentary soils

At hydrocarbon-contaminated sites, the NAPL phase (fourth within the vadose zone) can play a significant role in altering the global electrical properties of the affected soil. Immediately after the spill, the LNAPL tends to be partitioned into a vapour phase in the upper vadose zone, a residual phase and a free phase above the water table, and a dissolved phase in the saturated zone. A long-term contamination, where the LNAPL moves according with water table fluctuations, is characterized by entrapment of the free phase LNAPL in isolated pockets in the saturated zone and in the region of residual phase, with consequent origin of the so-called smear zone.

Although LNAPL contamination should be detected as a resistive anomaly, many recent studies have proved that the hydrocarbon contaminants can be an optimal source of organic matter for biomass (Atekwana et al., 2000; Atekwana et al., 2002; Werkema et al., 2003). At long-term contaminated sites, the mature hydrocarbon could undergo bio-degradation, generating a conductive plume where ionic species and degradation by-products can be found. In fact, in case of favourable subsoil conditions for bacterial growth, the presence of an organic contaminant can enhance the proliferation of NAPL-degrading biomass colonies. Many recent works (e.g. Atekwana et al., 2000, 2002; Atekwana et al., 2004a, b, c, d; Abdel Aal et al., 2006; Bradford, 2007; Cassidy, 2007, 2008; Allen et al., 2007) have showed good correlation between low resistivity anomalies and strongly contaminated zones where biodegradation was taking place. This alteration in the geophysical signature has been attributed to the formation of metabolic by-products, such as organic acids, gases and bio-surfactants, leading to an enhanced mineral dissolution and to changes in pore-fluid specific electrical conductivity. Since the microbial cells are attached to the grain surface, the biological activity influences the surface resistivity, resulting in a general decrease of the bulk resistivity. Common DC resistivity methods are sensitive to global conduction properties, but they are not able to discriminate between electrolytic and surface conduction processes. Induced Polarization methods are sensitive to changes in grain surface properties, and hence to changes surface electrical properties as a result of mineral alteration and dissolution due to biodegradation of the contaminant (e.g., Abdel Aal et al., 2004, 2006; Slater and Lesmes, 2002).

Most of the literature studies agree that aged hydrocarbon undergoing degradation results in a conductive plume, but there are some studies that associate strong NAPL contamination to resistive feature into the subsoil (e.g. Benson et al., 1998, Tezkan et al., 2005, Frohlich et al., 2008).

Therefore, hydrocarbon contamination is still an open task for the (bio-)geophysical researchers.

References

Abdel Aal, G., Atekwana, E.A., Slater, L.D., 2004. Effects of microbial processes on electrolytic and interfacial electrical properties of unconsolidated sediments. Geophys. Res. Lett., 31, L12505.

Abdel Aal, G.Z., Slater, L.D., Atekwana, E.A., 2006. Induced-polarization measurements on unconsolidatedsediments from a site of active hydrocarbon biodegradation. Geophysics, 71, H13–H24.

Allen, J.P., Atekwana, E.A., Atekwana, E.A., Duris, J.W., Werkema, D.D., Rossbach, S., 2007. The microbial community structure in petroleum-contaminated sediments corresponds to geophysical signatures. Appl. Environ. Microbiol., 73, 2860–2870.

Archie, G. E., 1942. The electrical resistivity log as an aid in determining some reservoir characteristics. Transactions of the American institute of Mining, Metallurgical and Petroleum Engineers, 146, 54–62.

Atekwana, E.A., Sauck, W.A., Werkema, D.D., 2000. Investigations of geoelectrical signatures at a hydrocarbon contaminated site. J. Appl. Geophys., 44, 167–180

Atekwana, E.A., Sauck, W.A., Abdel Aal, G.Z., Werkema, D.D., 2002. Geophysical investigation of vadose zone conductivity anomalies at a hydrocarbon contaminated site: implications for the assessment of intrinsic bioremediation. J Environ Eng Geophys, 7, 103–110

Atekwana, E.A., Atekwana, E., Werkema, D.D., Duris, J.W., Rossbach, S., Sauck, W.A., Cassidy, D.P., Means, J., Legall, F.D., 2004°. In situ apparent conductivity measurements and microbial population distribution at a hydrocarbon-contaminated site. Geophysics, 69, 56–63.

Atekwana, E.A., Atekwana, E., Rowe, R.S., Werkema, D.D., Legall, F.D., 2004b. The relationship of total dissolved solids measurements to bulk electrical conductivity in an aquifer contaminated with hydrocarbon. J Appl Geophys, 56, 281–294.

Atekwana E.A., Atekwana, E., Legall, F.D., Krishnamurthy, R.V., 2004c. Field evidence for geophysical detection of subsurface zones of enhanced microbial activity. Geophys. Res. Lett., 31:L23603.

Atekwana, E.A., Atekwana, E., Werkema, D.D., Allen, J.P., Smart, L.A., Duris, J.W., Cassidy, D.P., Sauck, W.A., Rossbach, S., 2004d. Evidence for microbial enhanced electrical conductivity in hydrocarbon-contaminated sediments. Geophys. Res. Lett., 31:L23501

Atekwana, E.A., Atekwana, E.A., 2010. Geophysical signatures of microbial activity at hydrocarbon contaminated sites: a review. Surv. Geophys., 31, 247–283.

Bastani, M., Hubert, J., Kalscheuer, T., Pedersen, L., Godio, A., and Bernard, J., 2012. 2D joint inversion of RMT and ERT data versus individual 3D inversion of full tensor RMT data. An example from Trecate site in Italy. Geophysics, 77, WB233-WB243, DOI: 10.1190/GEO2011-0525.1.

Benson, A.K., Payne, K.L., Stubben, M.A., 1997. Mapping groundwater contamination using dc resistivity and VLF geophysical methods — a case study. Geophysics, 62, 80–86.

Bouchedda, A., Chouteau, M., Binley, A., Giroux, B., 2012. 2-D Joint structural inversion of cross-hole electrical resistance and ground penetrating radar data. Journal of Applied Geophysics, 78, 52-57.

Börner, F.D., Schön, J.H., 1991. A relation between the quadrature component of electrical conductivity and the specific surface area of sedimentary rocks. The log analyst, 32, 612-613.

Börner, F.D., Schopper, J.R., Weller, A., 1996. Evaluation of transport and storage properties in the soil and groundwater zone from induced polarisation measurements. Geophysical Prospecting, 44, 583-601.

Bradford, J.H., 2007. Frequency-dependent attenuation analysis of ground-penetrating radar data. Geophysics, 72, J7–J16. doi:10.1190/1.2710183

Cassiani, G., Bruno, V., Villa, A., Fusi N., and Binley, A. M., 2006. A saline tracer test monitored via time-lapse surface electrical resistivity tomography. Journal of Applied Geophysics, 59, No. 3, 244-259.

Cassiani G., Godio, A., Stocco, S., Villa, A., Deiana, R., Frattini, P., Rossi, M., 2009. Monitoring the hydrologic behaviour of a mountain slope via time-lapse electrical resistivity tomography. Near Surface Geophysics, 7 , 475-486.

Cassidy, N.J., 2007. Evaluating LNAPL contamination using GPR signal attenuation analysis and dielectric property measurements: practical implications for hydrological studies. J. Contam. Hydrol., 94, 49–75.

Cassidy, N.J., 2008. GPR attenuation and scattering in a mature hydrocarbon spill: a modeling study. Vadose Zone J., 7, 140–159.

Comina, C., Sambuelli, L., 2012. Geoelectrical measurements for agricultural canal seepage detection. Proceedings Near Surface Geoscience 2012 -18th Meeting on Environmental and Engineering Geophysics - Paris, 3-5 Sep., paper n. C.34, 5pp.

Davis, K., Li, Y. 2011. Fast solution of geophysical inversion using adaptive mesh, space-filling curves and wavelet compression. Geophysical Journal International, 185, 157–166.

Ellis, R.G., Oldenburg, D.W., 1994. Applied geophysical inversion. Geophysical Journal

International, 116, 5-11.

Frohlich, R.K., Barosh, P.J., Boving, T., 2008. Investigating changes of electrical characteristics of the saturated zone affected by hazardous organic waste. J. Appl. Geophys., 64, 25–36.

Godio A., Naldi M., 2003b. Two-dimensional electrical imaging for detection of hydrocarbon contaminants. Near Surface Geophysics, 1, 131-137.

Godio A., Naldi, M., 2009. Integration of Electrical and Electromagnetic Investigation for Contaminated Site. American Journal of Environmental Sciences, 5, 561-568, ISSN: 1553-345X.

Godio, A., and Ferraris, S., 2005. Time lapse geophysics for monitoring an infiltration test in vadose zone. Bollettino di Geofisica Teorica e Applicata, 46, 201-216.

Godio, A., Arato, A., Stocco, S., 2010. Geophysical characterization of a nonaqueous-phase liquid–contaminated site. Environmental Geosciences 17, pp. 141-162.

Godio, A., Borsic, A., Arato, A., Sambuelli, L., 2011. On the inversion of cross-hole resistivity data. Geophysical Research Abstracts, 13, EGU2011-7950.

Grahame D.C., 1947. The electrical double layer and the theory of electrocapillarity. J. Electrochem. Soc., 99, 370-385.

Hallof, P.G., 1964. A comparison of the various parameters employed in the variable frequency induced-polarisation method. Geophysics, 29, 425-433.

Kemna, A., Binley, A. M., 1996. Complex electrical resistivity tomography for contaminant plume delineation. Proc. 2nd Mtg. in Environmental and Engineering Geophysics. Environ. and Eng. Geophys. Soc. – Eur. section, 196-199.

Kemna, A., Räkers, E., Binley, A. M., 1997. Application of complex resistivity tomography to field data from a kerosene-contaminated site. Proc. 3rd Mtg. Environmental and Engineering Geophysics, Environ. Eng. Geophys. Soc., Eur. Section, 151-154.

Kemna, A., 2000. Tomographic inversion of complex Resistivity. Theory and application. PhD Thesis. Der Andere Verlag.

Kemna, A., Binley, A., Slater, L., 2004a. Crosshole IP imaging for engineering and environmental applications. Geophysics, 69, 97–107.

LaBrecque, D. J., Miletto, M., Daily, W., Ramirez, A., Owen, E., 1996. The effect of noise on Occam's inversion of resistivity tomography data. Geophysics, 61, 538–548.

Lucius, J., Olhoeft, G.R., Hill, P.L., Duke, S.K., 1992. Properties and hazards of 108 selected substances, 1992 edn. United Staes geological survey open file report, 92-527, 560 pp.

Marcak, H., Golebiowski, T., 2008. Changes of GPR spectra due to the presence of hydrocarbon contamination in the ground. Acta Geophys, 56, 485–504.

Marshall, D.J., Madden, T.R., 1959. Induced polarisation, a study on its causes. Geophysics, 24, 790-816.

Olhoeft, G.R., 1985. Low frequency electrical properties. Geophysics, 50, 2492–2503.

Rhoades, J.D., van Schilfgaarde, J., 1976. An electrical conductivity probe for determining soil salinity. Soil Sci. Soc. Am. J. 40:647-650.

Rhoades, J.D., 1993. Electrical conductivity methods for measuring and mapping soil salinity. Adv. Agron. 46:201-251.

Rücker, C., Günther, T., 2011. The simulation of finite ERT electrodes using the complete electrode model. Geophysics, 76, 4, 227-238. DOI: 10.1190/1.3581356.

Sambuelli, L., Socco, L. V., Godio, A., Nicolotti, G., Martinis, R., 2003. Ultrasonic, electric and radar measurements for living trees assessment. Bollettino di Geofisica Teorica ed Applicata, 44, No. 3-4, 253-279.

Sasaki, Y., 1994. 3-D resistivity inversion using the finite-element method. Geophysics,

59, 1839–1848.

Sauck, W.A., 2000. A model for the resistivity structure of LNAPL plumes and their environs in sandy sedments. Journal of Applied Geophysics, 44, 151-165.

Schopper, J. R., Kulenkampff, J. M., Debschüts, W. G., 1997. Grenzflächenleitfähigkeit. In Knödel, K., Krummel, H., Lange, G., Eds. Handbuch zur Erkundung des Untergrundes von Deponien und Altlasten, Band 3 – Geophysik: Springer-Verlag Berlin, 992-995.

Seigel, H. O., 1959. Mathematical formulation and type curves for induced polarization. Geophysics, 24, 547–565.

Slater, L.D., Lesmes, D., 2002. IP interpretation in environmental investigations. Geophysics, 67, 77–88.

Strobbia C., Godio, A., and De Bacco, G., 2006. Interfacial waves analysis for the geotechnical characterization of marine sediments in shallow water. Bollettino di Geofisica Teorica e Applicata, 47, 145-162.

Tezkan, B., Georgescu, P., Fauzi, U., 2005. A radiomagnetotelluric survey on an oil-contaminated area near the Brazi Refinery, Romania. Geophys. Prospect., 53, 311–323.

Tikhonov, A. N., Arsenin, V. Y., 1977. Solutions of Ill-Posed Problems: Winston & Sons Washington D.C.

Wait, J.R., 1959. The variable-frequency method. in Wait, J.R., Overvoltage research and geophysical applications. Pergamon Press.

Ward, S. H., Fraser, D. C., 1967. Conduction of electricity in rocks. In Hansen, D. A., Heinrichs, Jr., W. E., Holmer, R. C., McDougall, R. E., Rogers, G. R., Sumner, J. S., Ward, S. H., Eds., Mining Geophysics, II: Soc. Expl. Geophys., 197-223.

Waxman, M. H., Smits, L. J. M., 1968. Electrical conductivities in oil-bearing shaly sand. Soc. Petr. Eng. J., 8, 107-122.

Yang, X., Lagmanson, M., 2006. Comparison of 2D and 3D Electrical Resistivity Imaging Methods. Symposium on the Application of Geophysics to Engineering and Environmental Problems, 585-594,

2. Staggered grid inversion of cross hole resistivity tomography

This chapter is centred on the development of a novel technique based on FEM grid manipulation, with the aim of alleviate the intrinsic under-determination and non-uniqueness of common geo-electrical inverse problems.

It will go through a brief introduction on grid manipulation for image quality enhancement, then a description of the proposed methodology, and its application to both synthetic and real datasets of electrical resistivity.

2.1 Introduction

The use of staggered grid to increase resolution and minimize the inversion ambiguities and instability was evaluated by several authors in seismic applications (Michelini, 1995; Vesnaver, 1996; Bohm et al., 2000; Vesnaver and Böhm, 2000; Louis et al., 2005), in non destructive testing (Sambuelli et al., 2011) and in optical engineering problems (Ur and Gross, 1992; Poletto and Nicolosi, 1999). The optical works showed that a super-resolution image can be obtained by shifting and merging a certain number of low resolution images. Since the pixels can be equally resolved in every part of the image, the grid shift and the merging of the staggered images permits to enhance the resolution, but approaching several well-posed problems instead of solving one highly under-determined problem. These considerations can be transferred to the inversion of geo-electrical problems, even though it has to be taken in account that not every zones of the domain of interest are equally resolved, and resolvable. This is due to the intrinsic limitation of the method to solve the problem in the zones characterized by a poor model resolution. The analysis of the importance of an accurate meshing shows that, although the data predicted nearby the electrodes from a forward model are affected by an acceptable error, the field calculated in the farthest cells, which is often of great interest, may contain errors that will result in image artefacts or lead to in-correct resistivity reconstruction.

The reconstructed images using staggered grids provide a smoothed version of the true model since they operate as a moving average filter on the model (Vesnaver and Böhm, 2000). On the other hand the final solution, as a result of the grid shifting, shows high accuracy and resolution since both the geometry and the properties values throughout the model are better determined. Conventional high-resolution grid inversion fails to properly image regions of reduced information, and in general a considerably blurred image is generated. This aspect becomes relevant especially when geophysical data are used to infer the hydrological properties of the soil (e.g. water content changes), and even more when dealing with time-lapse analysis.

With grid staggering the image quality is enhanced, in the sense that the result is obtained by averaging the results of several inversions carried out on coarsely gridded models. The reduction of model element number contributes to limit the under-determination of the problem. Furthermore, the possibility to average the various solutions and to check the dispersion of the resistivity distribution cell-by-cell can be useful in reducing the possible non-uniqueness of the solutions without imposing any a-priori constraining conditions that, sometimes, are unknown. Therefore a greater deal of information from the data without the risk of misleading to a preferred result can be retrieved. We apply the SGERT to electrical resistivity survey in cross-hole configuration, both on synthetic and real data set. The main objectives of this study are to demonstrate its effectiveness in reducing the formation of artefacts from the inversion procedure, in detailing the reliability of the final reconstructed model, and in detecting the resistivity boundaries. In order to reach these objectives, after a brief overview of the theoretical background and a description of the method, we apply the SGERT to two synthetic cross-hole cases and we present an application of SGERT to a real case, inverting a set of resistivity data from a hydrocarbon-contaminated site.

2.2 The Staggered Grid method applied to 2-D Electrical Resistivity Tomography

The SGERT is based on the reiteration of a 2D tomographic inversion using several grid meshing by averaging the resistivity values obtained from every inversion at the same given point. The different meshes are usually given by shifting the nodes of a selected mesh along vertical and horizontal direction. The vertical boundaries in correspondence of the boreholes, where the electrodes are installed, remain fixed, in order to guarantee that the electrodes coincide with

nodes of the mesh through which the potential field is calculated. The inner cells (within the imaging region) can be shifted, yielding to a deformation of the cell size along the boundaries of the imaging region, while the total number of cells and the size of the cells not confining with the imaging region boundaries are preserved.

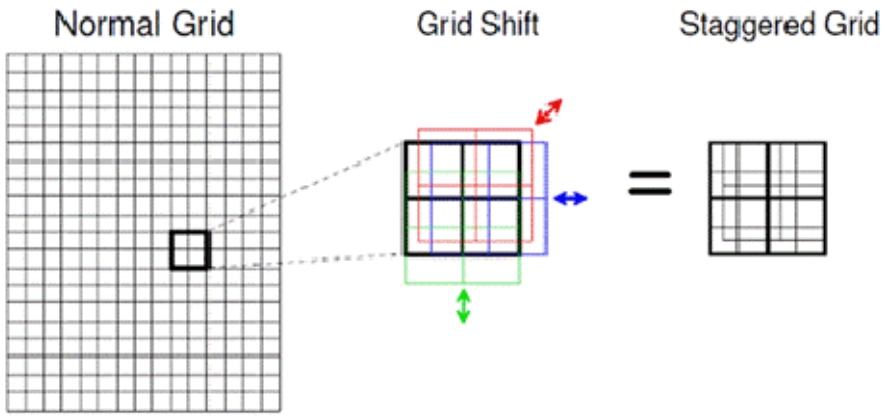

Fig. 2.1: the staggered grid process involves the grid shift and provides different images of the same target (after Louis et al. 2005).

We adapt the staggered grid process suggested and applied to seismic data processing (Figure 1) by Louis et al. (2005) according to the following steps:

1. A starting mesh grid is defined. It can be either regular irregular or adapted according to the sensitivity distribution over the model. The tomographic problem is thus solved for the said mesh.

2. The nodes are horizontally and vertically shifted according to a fixed amount, as depicted in Figure 1. Assuming a regular grid (within the imaging region between boreholes), being *dx* and *dz* the horizontal and vertical cell sizes, and being *sub_size* the final smallest size of the sub-cells from the SGERT, we have to perform N_x and N_z shifts, in horizontal and vertical direction, respectively:

$$N_x = 2 \cdot \left(\frac{dx}{sub\_size} - 1 \right) \tag{2.1}$$

$$N_z = 2 \cdot \left(\frac{dz}{sub\_size} - 1 \right) \tag{2.2}$$

where the factor 2 means that the shift has to be performed along the same direction but in the two different verses, with a shift that is proportional to *N*sub_size*.

The size of the elements remains the same in the central part of the imaging region, and in some cases the cell boundaries can coincide, even though the cells confining with the imaging region boundaries change their volume as a consequence of the shift.

3. Then we get $N=N_x+N_z$ new meshes where the same dataset has to be inverted on. N doesn't have to be too large, in order to avoid quasi-coincident meshes and to decrease the computational time. The dataset from the forward model is inverted by using R2 code. The algorithm is based on the inversion technique reported in the introduction. The inversion domain is approximately ten times larger than the imaging region both in *x*- and *z*- direction, in order to apply Neumann condition to the boundaries. We set the error variance model parameter as a percentage of each resistance measure, and the data weights are allowed to be modified at each iteration. The smoothing factor is updated by the code at each iteration.

4. We solve the tomographic problem for each new position of the shifted mesh, obtaining *N* new tomographic solutions.

5. We obtain the final solution by averaging the resistivity values of the cells having the same spatial coordinates in all the solutions. This procedure is performed by re-sampling in sub-cells each single solution image according to the minimum spacing used in the mesh shifting (in our case 1/8 of the horizontal cell size) considering that the resistivity values inside each cell of the resulting images are constant.

6. The standard deviation of the averaged resistivity values for each sub-cell is then computed.

2.2.1 Application to synthetic data

We analyse the performance of SGERT on synthetic cross-hole resistivity data. The geometry of the model and the position of the electrodes simulate the field condition of two boreholes spaced of about 6 m; each one is addressed with 24 electrodes from 1 to 17.1 m in depth, with an electrode spacing of about 0.7 m. The section delimited by the boreholes and by the presence of the electrodes is what we refer to as the imaging region. We assume a pole-dipole configuration. The starting mesh grid is designed according to the dimensions of the imaging region. Each cell in the imaging region has dimensions of 0.4 x 0.35 m in horizontal and vertical direction respectively. Far from the imaging region the mesh becomes progressively coarser.

As explained above, the starting mesh grid is shifted horizontally of a fixed amount of 0.05 to 0.35 m in both horizontal direction, obtaining fourteen new meshes, and of 0.05 to 0.3 m in both vertical direction, obtaining twelve more meshes. On the whole we have to invert the same dataset on 27 mesh grids.

We generate the synthetic data sets of resistivity values using the forward model of the R2 code (courtesy of A. Binley – Lancaster University). This software is designed for cross-borehole problems, and allows to build a finite element model of the subsurface, with a generalized quadrilateral mesh, by which forward modeling and real data inversion can be performed. We discretize the model space with a fine mesh of 0.1 m x 0.05 m, in horizontal and vertical direction respectively, and we obtain the resistance values for 1200 independent array configurations both in in-hole and in cross-hole arrangements.

Synthetic model n. 1

With reference to Figure 2a, we select a model with a background of 500 ohm m in the upper part of the section, and 100 ohm m in the lower part of the section. Within the lower part we insert a 1000 ohm m (3 in log scale) body. The model simulates a sharp boundary between the vadose zone, the uppermost part, and the saturated zone of a shallower aquifer. In the saturated zone the high resistive body simulates the inclusion of a low-porosity and low-permeability feature with high resistivity values.

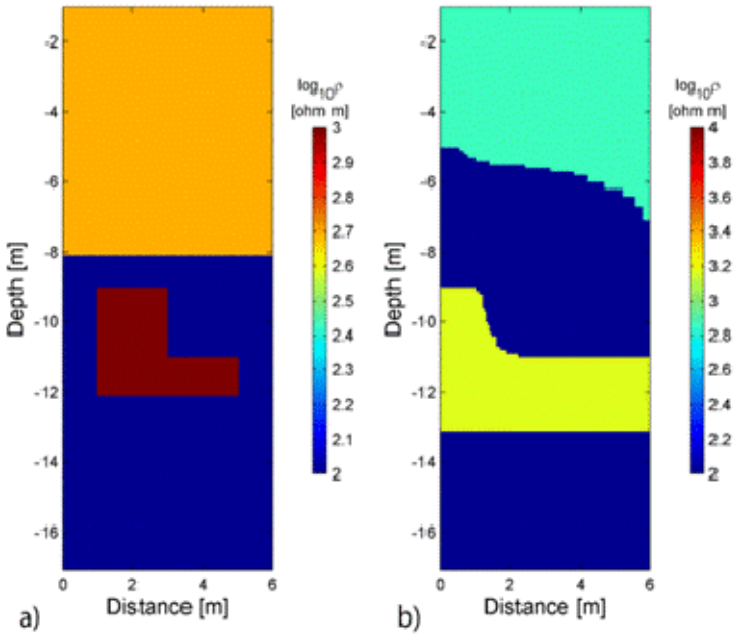

Fig. 2.2: a) synthetic model n.1; b) synthetic model n.2.

Synthetic model n. 2

As shown in Figure 2.2b , the second synthetic model represents a four-layer model in which the layers have a laterally varying thickness. The upper layer has a resistivity of 700 ohm m, while the intermediate layer is characterized by a resistivity value of 1500 ohm m. The other two layers are characterized by a low resistivity of 100 ohm m. The model simulates a geologically stratified soil, with superficial poorly-saturated sand overlying a silty layer, and then a level of gravel over a sand aquifer.

We invert the synthetic dataset using the R2 code fixing an error variance parameter of the model to be consistent with the noise level imposed to the data. We choose the maximum number of iteration to be equal to 10. The optimal smoothing factor is updated by the code at each iteration, and it was properly set to have a lightly smooth model along the horizontal direction, as it is usually done to follow the horizontal geological layers.

Firstly we invert the synthetic datasets discretizing the imaging region with a regular mesh of 0.1 m x 0.1m in size so that we obtain the result with a single inversion. This grid will be called “fine regular grid” afterwards. Another inversion of the same dataset is carried out on a grid that qualitatively reflects the sensitivity distribution over the model, having horizontal cell dimension that range between 5 cm close to the boreholes to 1 m in the middle of the section in the imaging region. We will refer to this grid as the “coarse irregular grid”. Gridding used for SGERT will be referred to as “coarse regular grid”. Details of the grid geometry are given in Figure 2.3.

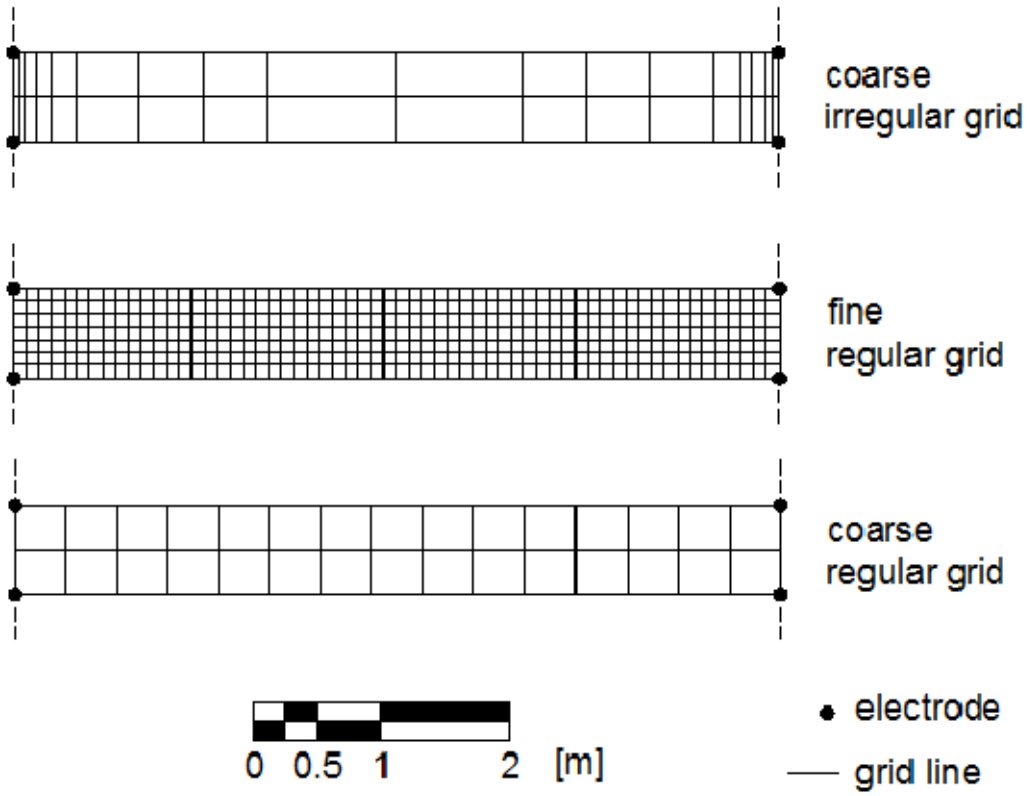

Fig. 2.3: different discretization for the three grids used in the comparison between traditional inversion schemes and SGERT method.

Then we apply the SGERT to the synthetic dataset, inverting the 27 different grids described above (uniform size of 0.4 x 0.35 m), taking into account the initial grid and the 26 shifts; each resulting matrix is re-sampled, with a nearest neighbour interpolation, in sub-cells with 0.05 m x 0.05 m in size and the average resistivity section within the imaging region is obtained, together with its associated relative standard deviation (RSD). This parameter, expressed as the ratio between the standard deviation and the average resistivity value at the corresponding node, is preferred to the absolute standard deviation and permits to compare in a clearer way the different results.

Furthermore, we add to the synthetic dataset for the model n.2 two different levels of Gaussian noise: each resistance measure is considered as the average of a normal distribution, with variance equal to 5% and 20% of the average resistance. From each distribution we randomly pick up a new resistance value, thus originating three new synthetic dataset to be inverted as described above.

Finally, we compare the results of the two methods (standard single grid inversion and SGERT inversion performed on the model n.2 at both noise levels) analyzing the discrepancy between

the results and the synthetic model in each cell over the imaging region. In each cell, the resistivity of the synthetic model in is compared to the estimated one, and the relative percentage error (RPE) is computed according to the Equation (7):

$$\mathrm{RPE} = \frac{\rho_i - \rho_m}{\rho_m} \cdot 100 \tag{2.3}$$

where ρ_i is the inverted resistivity, either from single inversions or from SGERT process, and ρ_m is the model resistivity.

The RPE gives information on the quality of the results for each cell. To get also a single indicator of the quality of the result we calculate the mean absolute difference (MAD) between the inverted and the model resistivity, expressed in [Ω·m]:

$$\mathrm{MAD} = \frac{1}{n}\sum_{j=1}^{n}\left|\rho_{i,j} - \rho_{m,j}\right| \tag{2.4}$$

where n is the number of resistivity cells into the imaging region, $\rho_{i,j}$ is the j^{th} resistivity value from the inversion process and $\rho_{m,j}$ is the j^{th} resistivity value of the model.

2.2.2 Application to real data

An application of the SGERT was carried out on a set of field AC resistivity data, collected at the hydrocarbon contaminated site of Trecate, Northern Italy. Both the two part of the complex resistivity (resistance and phase between voltage and current sinusoidal signals) were measured with the AC georesistivimeter Polares, developed by PASI Geophysics Ltd. Jointly with Politecnico di Torino, which is designed to measure complex resistivity data in the frequency range between 0.1 to 100 Hz. In this context, just the real part of the complex resistivity is considered, and the inversion is carried out on resistivity data collected at a frequency of 1.79 Hz. The Trecate site has been the scene of an inland crude oil spill in 1994, after an accident at an oil well during the drilling phase. In the most contaminated area, a test site was set up for cross-hole Ground Penetrating Radar (GPR) and Electrical Resistivity Tomography (ERT). The test site consists of two boreholes, B-S3 and B-S4, 6 m spaced, drilled down to a depth of 18 m and completed with 2” PVC screened casing. A general overview of the preliminary geophysical characterisation of the area is given in Godio et al. (2010). The boreholes were drilled in a superficial silty material accumulation zone hosted above an unconfined gravel or sand aquifer. Each borehole is addressed with 24 graphite electrodes, integrated along the cable. The electrodes are 0.7 m spaced, from the depth of 1 m to 17.1 m. The boreholes are available both for geophysical investigations and for geo-chemical surveys.

The cross-hole electrical survey involved the data acquisition with electrode located both in the vadose zone and saturated zone, where a gradual downward increase in fluid saturation, through the capillary fringe was observed. Saturation and de-saturation processes at Trecate site are predominantly controlled by infiltration from the surface and by regional recharge at a large scale, and a process of smearing of the free phase of the hydrocarbon is observed within the oscillation range of the water table during the year. The smearing zone is delimited by the lowest and highest groundwater level, which fluctuates over a range of 5 m during the year, from the depth of 6 m to 11 m.

2.3 Results and discussion

2.3.1 Synthetic model n.1

The results from the single inversion on the coarse irregular grid (Figure 2.4a), on the fine regular (Figure 2.4b) and from the SGERT (Figure 2.4c), show how the global aspect of the final images reflects the shape of the model. The SGERT better reconstructs the upper resistive layer with values closer to the model, points out the anomaly, but underestimates its resistivity value. Inversion on the coarse irregular grid shows quite homogeneous values in the upper and lower levels, but the anomaly is horizontally spread, due to the large elements in the middle of the imaging region. Inversion on the regular fine grid reconstructs the anomaly with more accuracy, in terms of both shape and values, but fails in imaging the upper homogeneous layer.

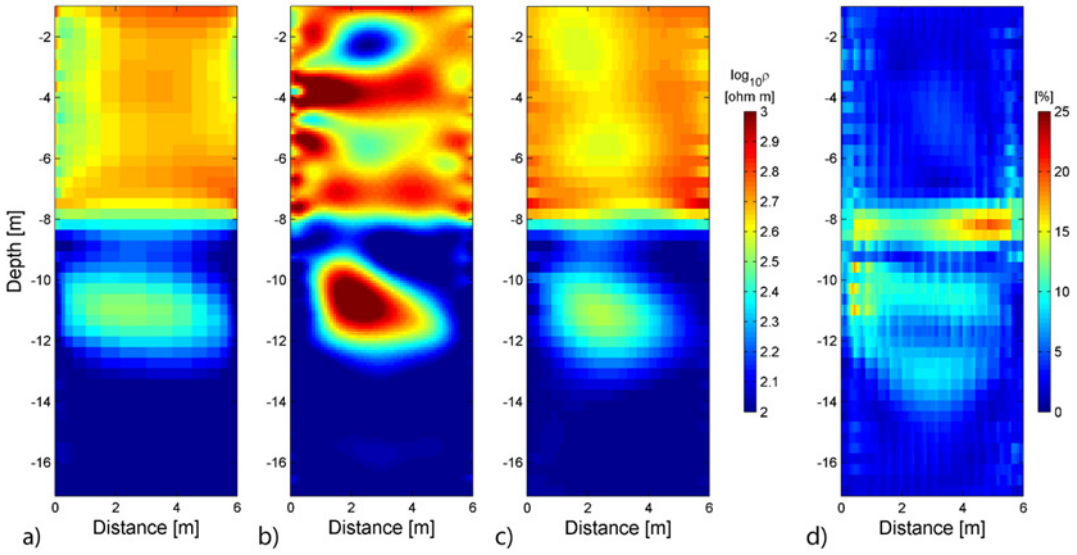

Fig. 2.4: synthetic model n.1: resistivity image from inversion of a) coarse irregular grid b) fine regular grid and c) image of averaged resistivity from SGERT; d) relative standard deviation image from the SGERT inversion.

The standard deviation image (Figure 2.4d) shows quite low values over all the image, except in those zones where the grid shift can produce some differences in the single results (i.e. resistivity boundaries and zones with very high sensitivity near the boreholes).

2.3.2 Synthetic model n.2

We show the results of the three inversions on model n.2 referring to the synthetic data with 5 % (Figure 2.5) and 20 % (Figure 2.6) of Gaussian noise added.

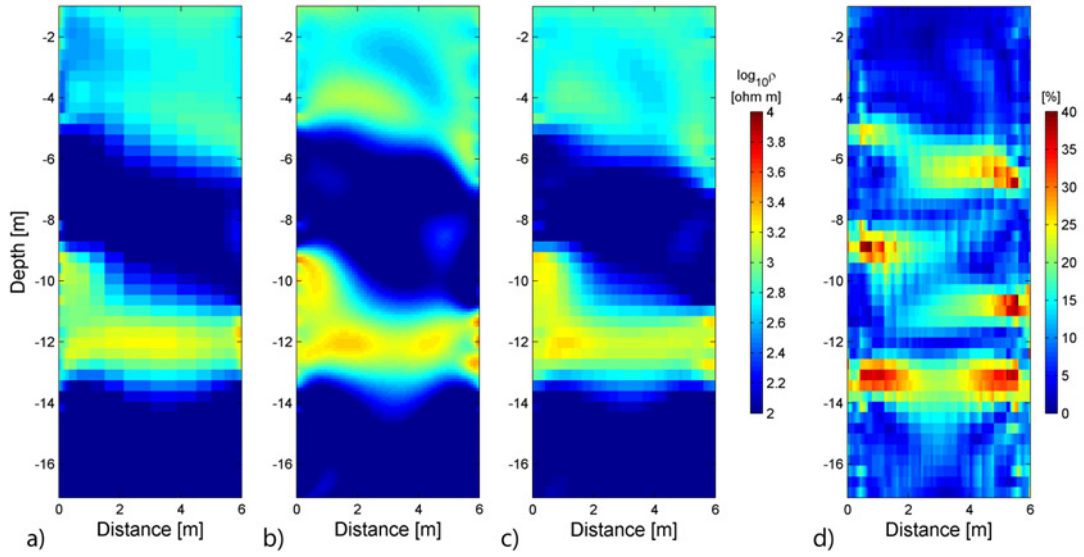

Fig. 2.5: synthetic model n.2, data with 5% noise; resistivity image from inversion of a) coarse irregular grid b) fine regular grid and c) image of averaged resistivity from SGERT; d) relative standard deviation image from the SGERT inversion.

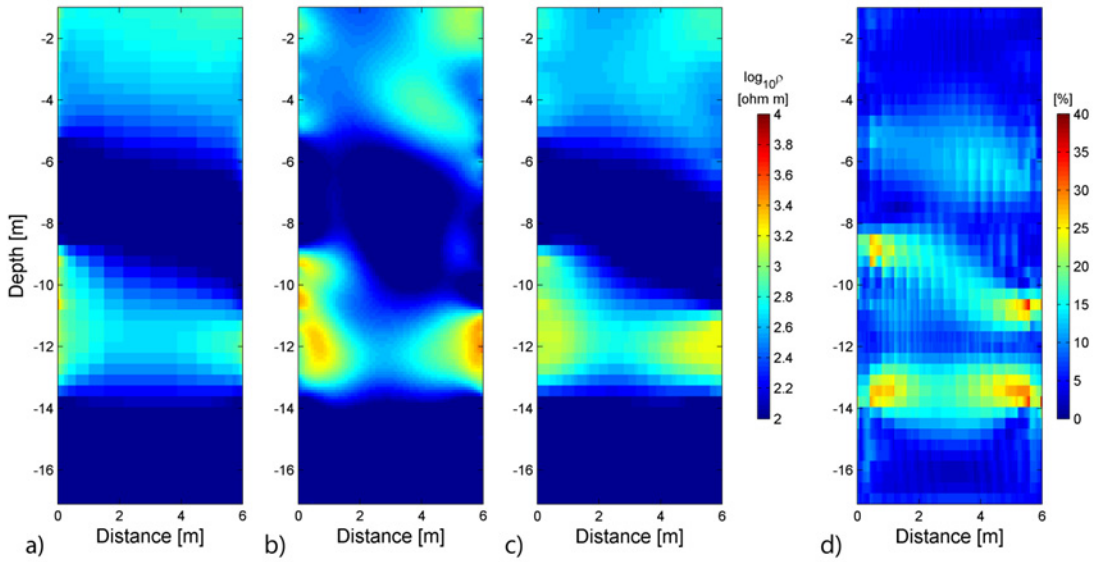

Fig. 2.6: synthetic model n.2, data with 20% of noise; resistivity image from inversion of a) coarse irregular grid b) fine regular grid and c) image of averaged resistivity from SGERT; d) relative standard deviation image from the SGERT inversion.

Comparing again the three methods, it can be seen how the SGERT tends to limit the formation of inversion artefacts at all the noise levels, obtaining smoother images that result to be more similar to the synthetic model. For model n.2 too, the standard deviation map shows the highest values in correspondence of the resistivity boundaries and within the high sensitivity areas close to the boreholes.

Figure 2.7 (model 1), Figure 2.8 (model 2, 5% noise) and Figure 2.9 (model 2, 20% noise) respectively show the RPE images, obtained for both the single grid and SGERT results, with reference to Equation (2.3).

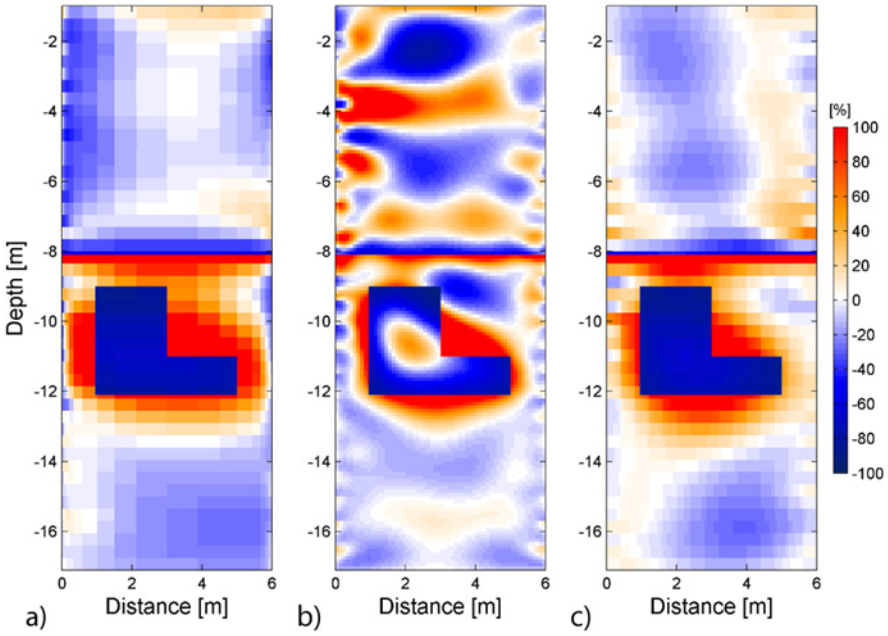

Figure 2.7: RPE calculated between the inversion result on the coarse irregular grid (a), on the fine regular grid (b) and SGERT result (c) on model 1.

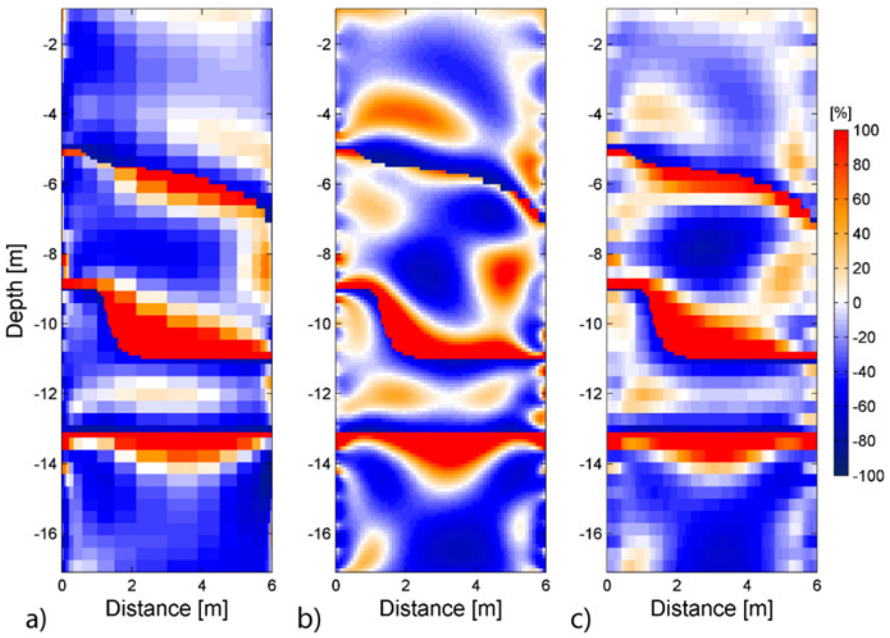

Figure 2.8: RPE calculated between the inversion result on the coarse irregular grid (a), on the fine regular grid (b) and SGERT result (c) on model 1 (data with 5% noise).

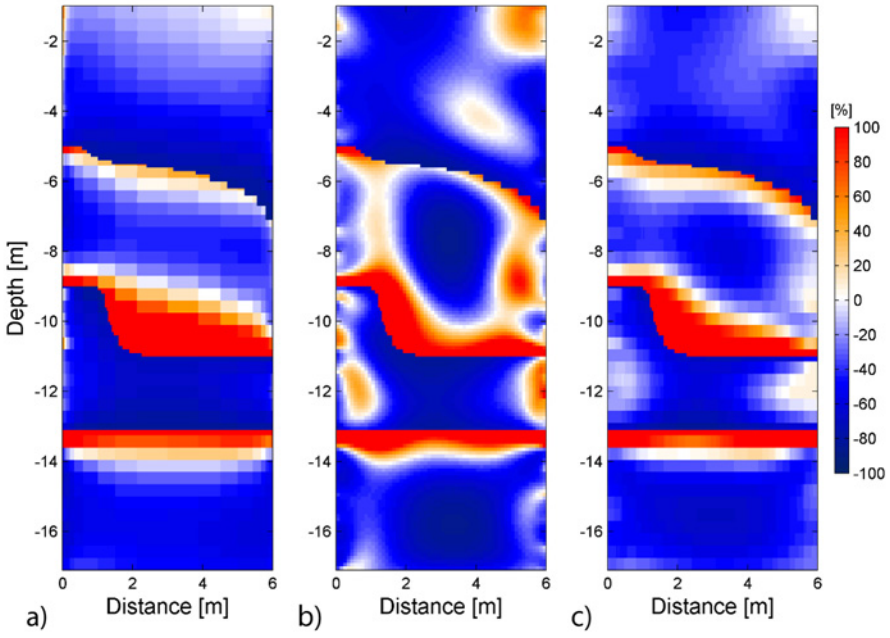

Figure 2.9: RPE calculated between the inversion result on the coarse irregular grid (a), on the fine regular grid (b) and SGERT result (c) on model 2 (data with 20% noise).

RPE images show the accuracy of the inversions, where white corresponds to perfect reconstruction, blue colours and red colours respectively stand for under- and over-estimation of

the model resistivity. Even though all the methods show similar RPE distribution, SGERT appears to be more accurate than single grid inversions in reconstructing the real value from the synthetic model. This is reflected also from MAD values, from Equation (2.4), reported in Table 1. It can also be observed that the RPE values are high in the zones of high standard deviation (i.e. in correspondence of the resistivity boundaries).

Tab. 2.1: MAD values for the three inversion results on the three different synthetic datasets

MAD [ohm m]	Fine regular grid	Coarse irregular grid	Staggered grid
Model 1	123.8654	112.6647	106.9666
Model 2 noise 5%	149.43	163.14	134.3269
Model 2 noise 20%	238.6005	270.9866	225.6439

2.3.3 Field dataset

Figure 2.10 reports the result from the single inversion on the coarse irregular grid (Figure 2.10a), on the regular fine grid (Figure 2.10b), the average resistivity result of SGERT inversion (Figure 2.10c) and the related standard deviation matrix (Figure 2.10d). The white line indicates the groundwater level.

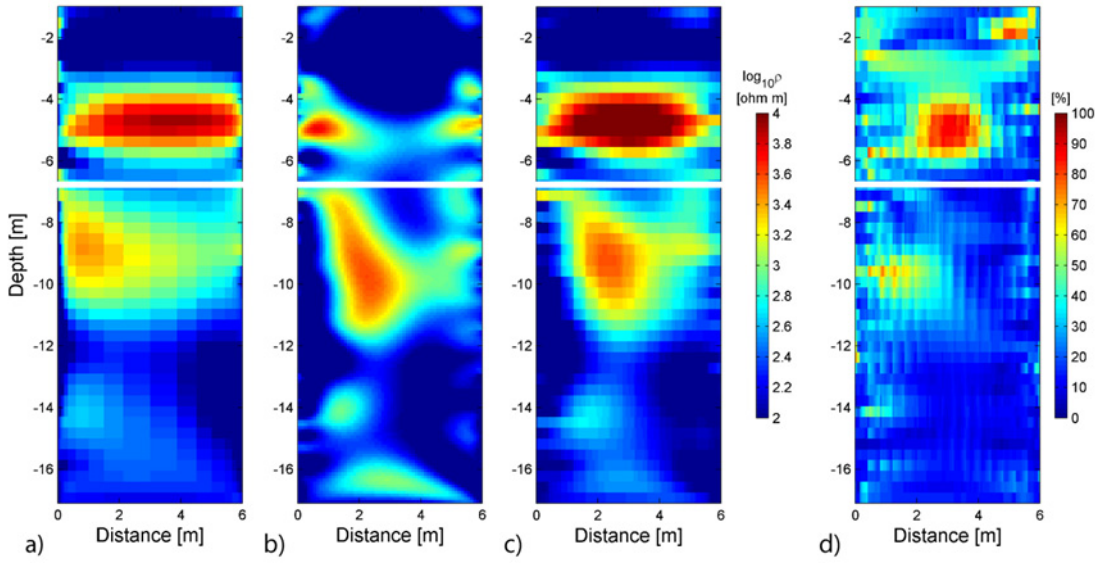

Fig. 2.10: Field dataset from Trecate site; a) resistivity image from a grid reflecting the sensitivity distribution; b) resistivity image from single grid inversion; c) image of averaged resistivity from SGERT; d) relative standard deviation image from the SGERT inversion.

This application of the SGERT on a real dataset improves the result if compared to the ones obtained with the single inversions. The inversion on the coarse irregular grid tends to spread the high resistive anomaly located in the depth range between 8 to 11 m, but it well reconstructs the rest. The inversion on the fine regular grid points out the anomaly but the whole image is blurred and affected by the presence of artefacts. The tomographic image from the application of SGERT shows, like the one from the coarse irregular grid, the alternance of conductive and resistive layers within the vadose zone and the resistivity anomaly in the saturated zone. The relative standard deviation values are higher in correspondence of the resistivity boundaries and in the middle of the resistive superficial layer.

We validate the SGERT results with some geological information of the Trecate site (Figure 2.11a), and to the results of the spectral analysis on a GPR Zero Offset Profile (ZOP) (Figure 2.11b); the GPR data was collected in the same day. The groundwater level is represented by the horizontal blue line. The resistive anomaly observed within the depth range of 8 m to 10 m is well related to the stratigraphy sequence (presence of sand and gravels). The tomographic image also agrees with the cross-hole ZOP data. The trend of the spectrum of the received signal at each depth is pointed out in Figure 10c. Data were collected at depth step of 25 cm. Each amplitude spectrum is computed by windowing each radar trace using the same time-window (160 ns). The peak of energy is observed just below the groundwater level. This founds an interpretation in the presence of a trapped hydrocarbon emulsion within the smear zone. The behaviour of the trapped NAPL, which is characterized by high resistivity and low permittivity, is somehow analogous to that explained in Glaser et al. (2012). In this work, which is about a controlled GPR lab-scale test, a controlled release of ethanol in a tank was monitored with a series of GPR acquisition over time. The highest peaks in the power spectra were observed just below the water table.

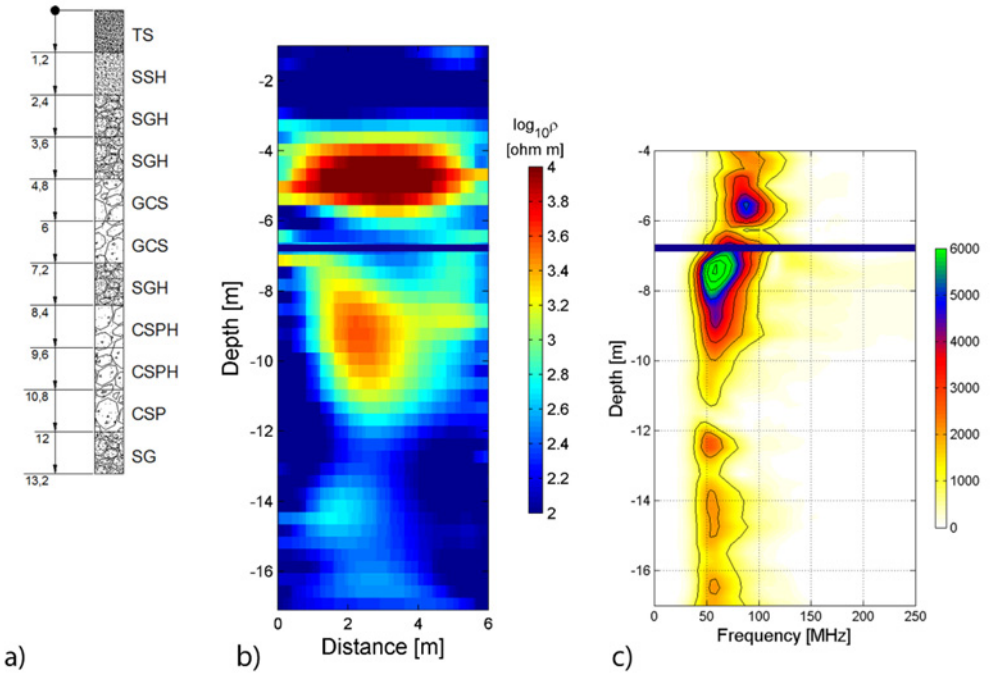

Fig. 2.11: a) subsoil stratigraphy at Trecate site (TS: top soil, SSH: silty sand w/ hydrocarbon, SGH: sand and gravel w/ hydrocarbon, GCS: gravel and coarse sand, CSPH: coarse sand w/ pebbles and hydrocarbon, CSP: coarse sand w/ pebbles, SG: sand and gravel); b) resistivity image from SGERT at Trecate site, values in log scale; c) trace-by-trace spectrum of the ZOP profile at Trecate site.

The conductive layer between the groundwater level and the resistive layer should correspond to the level where the hydrocarbon oxidation and bio-degradation is enhanced by the presence of fresh air, as the water table rise in summer and is followed by a part of the oil trapped in the pores. This very thin layer is evidenced also by the high values of standard deviation at the depth of 8 m, which indicates the presence of two resistivity boundaries, as explained above for the synthetic cases.

Finally, the conductive superficial layer corresponds to a zone of silt and sand accumulation, as evidenced by GPR profiles and ERT obtained from previous studies (Godio et al., 2010).

2.4 Conclusions

A procedure for resistivity data inversion which includes the staggered grid method was herein discussed. The main goal is to improve the reliability of the inversion by enhancing the S/N ratio and preserving, in the largest part of the domain, the conditioning of the selected inversion scheme. Furthermore, we obtain good results inverting several well-conditioned (or slightly under-determined) problems.

We tested the staggered grid procedure on both synthetic and field dataset. The results confirmed that the SGERT method can be a useful and powerful tool in the inversion of cross-hole resistivity data, where sensitivity problems and the presence of noise in the data cannot be overcome by a traditional single grid inversion and when a-priori conditions are not available. The procedure has a different effect on high gradient, e.g. near electrical interfaces, and on homogeneous zones, e.g. within a layer. In fact by shifting the mesh, the SGERT virtually increases the resolution and outputs sharper boundaries at the interfaces while, by the averaging operation, SGERT gives smoother images in the homogeneous zones provoking a reduction of inversion artefacts. As a consequence of the staggering, we estimate the standard deviation related to each pixel of the solution allowing for the evaluation of the precision of the final model. The image of the standard deviation is useful to detect resistivity boundaries in zones of poor model resolution. The main drawback is the need of performing many inversions which implies an increase in computational time even though this increase doesn't depend linearly on the number of inversion to be carried out. In fact, while performing a single inversion of a real dataset on a very fine mesh grid takes from 5 to 30 minutes (depending on the complexity of the problem and on the number of elements in the model), the completion of SGERT process requires from 30 to 90 minutes on a commercial laptop PC, with a 2.2 GHz processor and a 4 GB RAM. The strengths of the method are, besides the possibility to check the reliability of the solution over the interested area of the model, to reduce the artefacts and detect more accurately the resistivity boundaries. The possibility to overcome these problems encourages us to apply the SGERT to the time-lapse inversion of electrical resistivity data.

References

Binley A., 2010. Resistivity Software R2 profile Version 2.6 (November 2010).

Böhm, G., Galuppo, P., Vesnaver, A., 2000. 3D adaptive tomography using Delaunay triangles and Voronoi polygons: Geophysical Prospecting, 48, 723-744.

Cassiani, G., Godio, A., Stocco, S., Villa, A., Deiana, R., Frattini, P., Rossi, M., 2009. Monitoring the hydrologic behaviour of a mountain slope via time-lapse electrical resistivity tomography, Near Surface Geophysics, 7, 475-486.

Davis, K., Li, Y. 2011. Fast solution of geophysical inversion using adaptive mesh, space-filling curves and wavelet compression, Geophysical Journal International, 185, 157–166.

Glaser, D.R., Werkema, D.D., Versteeg, R.J., Henderson, R.D., Rucker, D.F., 2012. Temporal GPR imaging of an ethanol release within a laboratory-scaled sand tank. Journal of Applied Geophysics, 86, 133-145.

Godio, A., Naldi, M., 2003. Two dimensional electrical imaging for detection of hydrocarbon contaminants. Near Surface Geophysics, 1, 131-137.

Godio, A., Arato, A., Stocco, S., 2010. Geophysical characterization of a nonaqueous-phase liquid–contaminated site. Environmental Geosciences 17, pp. 141-162.

Godio, A., Borsic, A., Arato, A., Sambuelli, S., 2011. On the inversion of cross-hole resistivity data. Geophysical Research Abstracts Vol. 13, EGU2011-7950.

Kemna, A., 2000. Tomographic inversion of complex resistivity—Theory and application, PhD Thesis, Bochum Ruhr-Univ., Germany.

Lines, L. R., Treitel, S., 1984. A review of least-squares inversion and its applications to geophysical problems, Geophys. Prosp., 32, 159-186.

Louis F. I., Makropoulos, K. C., Louis, I. F., 2005. Image enhancement in seismic tomography by grid handling: Synthetic simulations with fault-like structures, Journal of Balkan Geophysical Society, 8, 4, 139-148.

Michelini, A., 1995. An adaptive-grid formalism for travel-time tomography: Geophys. J. Int., 121, 489-510.

Inman, J. R., 1975. Resistivity inversion with ridge regression, Geophysics, 40, 798-817.

Poletto L., Nicolosi, P., 1999. Enhancing the spatial resolution of a two-dimensional discrete array detector, Opt. Eng. 38, 1748-1757.

Sambuelli L., Bohm G., Capizzi P., Cardarelli E., Cosentino P. (2011). Comparison between GPR measurements and ultrasonic tomography with different inversion algorithms: an application to the base of an ancient Egyptian sculpture . Journal of Geophysics and Engineering, 8, 106-116.

Tezkan, B., Georgescu, P., Fauzi, U., 2005. A radiomagnetotelluric survey on an oil-contaminated area near the Brazi Refinery, Romania. Geophys. Prospect., 53:311–323.

Tikhonov, A. N., Arsenin, V. Y., 1977. Solutions of Ill-Posed Problems, Ed. Fritz, J.,Wiley & Sons.Ur, H., Gross, D., 1992. Improved resolution from subpixel shifted pictures. Graphical Models and image Processing, 54 (2), 181-186.

Vesnaver, A., 1996. Irregular grids in seismic tomography and minimum time ray tracing: Geophys. J. Int., 126, 147-165.

Vesnaver, A., and Böhm, G., 2000. Staggered or adapted grids for seismic tomography: The Leading Edge, 19, 944-950.

3. Forward modeling and inversion for 2-D and 3-D real/complex electrical resistivity data

This chapter presents the formulation of a forward/inverse code for 2-D and 3-D electrical resistivity data.

This code has been developed jointly with Dr. A. Borsic (Dartmouth College, Dartmouth, NE) within the activities of FP7 European Project SoilCAM, and is based on the numerical framework developed by Borsic and Adler (2012). It can be used on 2-D and 3-D Finite-Element models for both modelling and inversion of resistivity data, given an arbitrary geometric disposition of the current sources.

We present preliminary results related to the development of a novel package for 2D and 3D inversion (called NES-GeoElectric), for 2D and 3D inversion of electrical resistivity data. The approach is based on a core of functionalities, as computing the forward solution and the sensitivity matrix, that are optimized for speed of execution on single-core and multi-core computing platforms. These functionalities have been customized, within the SoilCAM EU FP7 project, for the specific application to subsurface imaging, including functions for automatic mesh generation given a description of the geometry of the site.

The inversion scheme is based on a Primal Dual-Interior Point Method (PD-IPM) framework which allows using either the L1-norm or the L2-norm on the data term and on the regularization term of the inverse formulation (Borsic and Adler, 2012). Use of the L1-norm on the data term corresponds to a Least Absolute Values formulation, which is particularly robust to the presence of outliers in the data, while use of the L1-norm on the regularization term corresponds to Total Variation formulation, which results in sharper reconstructed profiles. Besides the aforementioned approach, we implemented strategies to improve the accuracy in the forward model formulation and to reduce the errors that can arise from using simplified models, given that Electrical Resistivity Tomography (ERT) is an ill-posed inverse problem. Adaptive meshing or staggering grid are strategies that can minimize the ambiguities in most ill-pose problems as well; Arato et al. (2012, submitted) modified the original staggering grid approach (Michelini, 1995, Bohm and Vesnaver, 1999) to adapt the multi-inversion procedure to cross-hole resistivity data.

In processing of cross-hole resistivity data, with particular attention towards the monitoring of dynamic processes in contaminated sites, modelling electrodes with a finite extent covers a noteworthy importance, as the electrode size is usually not negligible compared to their distance. Modelling electrodes therefore as point source results in appreciable approximations, and contributes to poorer reconstructed images. The approach we adopted is focused on building accurate 2D and 3D forward meshes that account for the presence of the borehole and for the extent of the electrodes. These are described with a boundary condition known as Complete Electrode Model (CEM), as it has been taken from previous studies (e.g. Cheng et al., 1989, Somersalo et al., 1992, Hyvonen, 2004, Rücker and Günther, 2011).The CEM accounts for the finite size of the electrode and for the non-uniformity of the current density flow underneath the surface of the same electrode. This model has been shown experimentally to be able to predict measured data on electrodes of extended surface to 0.2% accuracy (Borsic, 2002).

The computation of the Jacobian matrix, the most intensive step in our implementation, has been implemented using calls to the Intel Math Kernel Library (MKL), a multithreaded BLAS and LAPACK implementation, highly optimized for modern PC architectures. This results in gains in the order of 30 times compared, for example, to the use of plain MATLAB. The forward solution, which requires solving a sparse linear system, and is the second most expensive step in our algorithm, has been implemented using the MKL PARDISO (PARAllel DIrect SOlver) solver, which in our tests is about 10 times faster compared to MATLAB's sparse solver on modern multicore PCs. These optimizations are particularly useful in 3D, as accurate modeling of electrodes and of the domain results in meshes with typically 100,000 to 300,000 nodes, and 500,000 to 1,500,000 tetrahedral elements.

Finally, the approach allows reconstructing complex resistivity data, when spectral electrical resistivity data are available and information on the induced polarization over the investigated medium is required. Both the real and imaginary values of the complex resistivity can be reconstructed.

3.1 Mesh Generation

In ERT imaging of the subsurface electric fields are applied to the ground by injecting current through electrodes. The concept behind resulting electric field has very strong spatial variations in proximity of the electrodes, while it is smooth at a distance. The use of adaptive refinement schemes is therefore promising in terms of forming meshes that are fine only where needed. As, particularly in 3D, using dense meshes (e.g. 500,000 nodes) results in a significant computational

effort, optimizations have been made, developing adaptive mesh approaches which guarantee a good forward accuracy and reduce computing time. We are currently implementing adaptive mesh refinement schemes, where, given an initial forward solution, a posterior error is estimated on each element of the mesh and worse elements are refined, leading to a reduction of the overall forward error. In such a context, Plattner et al. (2012) transfer the adaptive wavelet approach presented in Cohen et al. (2003) for well posed problems into the realm of underdetermined electrical resistivity tomography. This allows to generate initial meshes that are relatively coarse and to refine them only where needed, obtaining significant savings in computations. Figure 3.1 shows results from tests designed to verify those elements of the mesh that are correctly split.

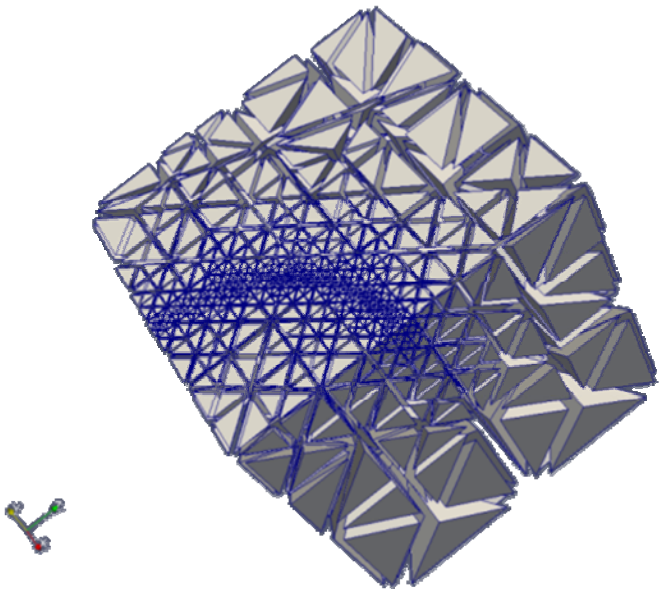

Fig. 3.1: Imaging test on adaptive mesh refinement.

We incorporate a series of routines for mesh generation considering a polygonal model of the imaging domain, of the electrodes, and of any borehole which might be present. Electrodes can be modelled as points or cylindrical sources, for the latter the Complete Electrode Model (CEM) is used. Given this geometric representation external mesh generators are used for creating 2D and 3D FEM meshes. We adopt, respectively the public domain software Triangle (http://www.cs.cmu.edu/~quake/triangle.html) for generating 2D meshes, and TetGen (http://tetgen.berlios.de/) for generating 3D meshes. As these two mesh generators are distributed in binary and source code form (C/C++ language), we developed ad-hoc MATLAB mex-files to interface and exchange mesh data with these packages.

The mesh generation provides two different models for the electrodes, in terms of their geometry. The simplest model is the *point electrode*. A second model is the *cylindrical electrode*, as the ones usually mounted on boreholes. The user specifies the location and the type of electrode model and an appropriate mesh representative of the geometry and electrode models is automatically generated. A second customization regards the boundary conditions to be applied to the mesh, which account for non uniform current density on the surface of electrodes (CEM). Meshes are extended to a distance from the imaging area, and impedance boundary conditions are used to simulate an infinite domain. The 2D and 3D mesh generation process allows to model an arbitrary number and location of boreholes, an arbitrary number of electrodes, considering their height, diameter and position along the borehole. The coarseness or fineness of the mesh can be adjusted as well in terms of:

- max volume of elements in the background region ;
- max volume of elements in the imaging region;
- max area of the facets that constitute electrodes.

With respect to Figure 3.2, we refer to the *background region* as the coarser mesh region which is used to model the soil volume at a distance from the electrodes. This volume, where a coarser mesh is generated, allows to approximate, with opportune boundary conditions, an infinite half-space. The *imaging region* presents a finer mesh, as it is the volume limited by the electrodes array, where the field has faster spatial variations, and where the resistivity is imaged. The adoption a finer mesh in this region provides for accurate forward solutions. Boreholes are modelled accounting for the diameter of the borehole and for the true extent of the electrodes.

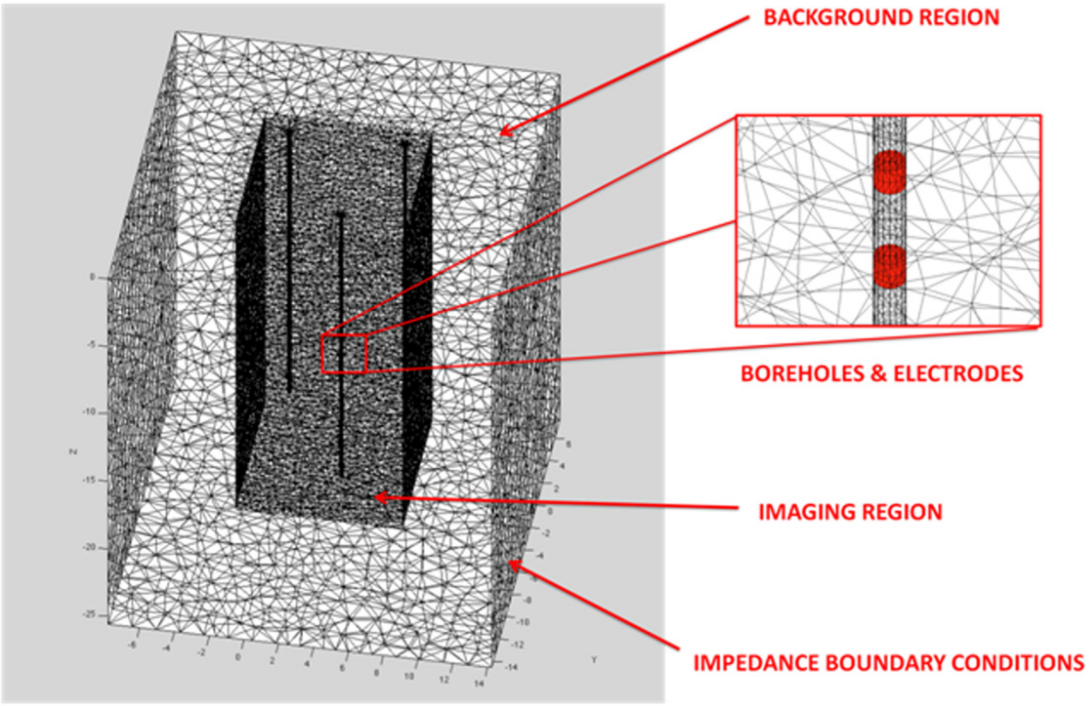

Fig. 3.2: Example of automatically generated mesh for a 3-D cross-hole problem.

3.2 Inversion of complex resistivity datasets

Since resistivity can be considered a function of frequency of the electric field applied into the ground, it is a naturally complex quantity. It has two contributions: one given by the real valued ground resistivity, and the second dependent on the polarization characteristics of the soil. Measuring the complex resistivity of a soil means to collect measurements of spectral data, e.g. amplitude and phase, at different frequencies in the desired frequency range. Resistivity (ρ) can be considered frequency-dependent and complex, defined as:

$$\rho(\omega) = \rho'(\omega) + i \cdot \rho''(\omega) \tag{3.1}$$

where ω is equal to 2π·f, and f is the frequency of the injected electrical field.

Recovery of both real and imaginary part of the complex resistivity can give additional information both regarding the soil constituents and pollutants such as hydrocarbons, which show induced polarization effects. The method works with real and complex valued field data, recovering modulus and phase of the complex resistivity, where phase information is available.

The reconstruction routines allow processing complex resistivity datasets, gathered from frequency domain AC georesistivimeters. The phase and amplitude component of the measured data can be inverted, reconstructing a tomographic image of the complex resistivity in the domain of interest, or recovering separately the real and imaginary part of the complex resistivity.

We provide four different inverse formulations for the reconstruction of the resistivity data:

$$\rho_{rec}=\text{argmin}\left\|W\left(Z(\rho)-Z_{meas}\right)\right\|^2+\alpha\left\|L\left(\rho-\rho^*\right)\right\|^2 \tag{3.2}$$

$$\rho_{rec}=\arg\min\sum_i\left|W_i(Z_i(\rho)-Z_{imeas})\right|+\alpha\left\|L\left(\rho-\rho^*\right)\right\|^2 \tag{3.3}$$

$$\rho_{rec}=\arg\min\left\|W\left(Z(\rho)-Z_{meas}\right)\right\|^2+\sum_j\left|L_j\left(\rho-\rho^*\right)\right| \tag{3.4}$$

$$\rho_{rec}=\arg\min\sum_i\left|W_i(Z_i(\rho)-Z_{imeas})\right|+\sum_j\left|L_j\left(\rho-\rho^*\right)\right| \tag{3.5}$$

where ρ_{rec} is the reconstructed resistivity vector (real or complex valued); W is a data covariance matrix; $Z(\rho)$ are the simulated apparent impedances, functions of the current model resistivity distribution ρ; Z_{meas} is the vector holding the measured apparent impedances; α is the Tikhonov factor; L is a regularization matrix and ρ^* is a prior resistivity distribution (a uniform background in case no prior information is available).

Formulation (3.1) is the classic formulation commonly used, resulting in a non-linear regularized Least Squares problem, which is solved using Gauss Newton algorithms. Formulation (3.2) involves instead the L1-norm on the data term, resulting in a Least Absolute Values formulation. Being the sum of absolute values a non-smooth function, non-differentiable on the entire domain, special optimization techniques are required to solve efficiently (2). The Gauss Newton method, in these conditions, in fact does not converge, or converges extremely slowly (Borsic, 2002). The Primal Dual Interior Point framework can be an effective alternative as it converges quadratically (Borsic and Adler, 2012). The benefit in considering formulation like (3.2) is that the use of the L1-norm on the data term makes them particularly robust to data outliers, as shown in Borsic and Adler (2012). Formulation (3.3) instead uses the L1-norm on the regularization term, an approach that leads to Total Variation regularization, and which results in sharper reconstructed profiles. Formulation (3.4) incorporates the L1-norm both on the data and regularization terms. The choice of any of the above 4 formulations depends on the data noise and smoothness of the model distribution: formulations (3.1) and (3.3), which use the L2-norm on the data term, are optimal when there are no outliers on the data, and data errors follow mostly a Gaussian distribution, while formulations (3.2) and (3.4), which use the L1-norm on the data term, are optimal if outliers are present in the data. Formulations (3.1) and (3.2), which use the L2-norm on the regularization term, are optimal when the spatial distribution of resistivity is expected to be smooth, while formulations (3.3) and (3.4), which use the L1-norm on the regularization term, are optimal when the resistivity profile presents sharp spatial changes.

Depending on the characteristics of the data and of the resistivity profile therefore one of the four formulations is optimal, and can be chosen by the user. A detailed description of the Primal Dual Interior Point Method framework used for solving (3.2), (3.3), and (3.4) is given in (Borsic and Adler, 2012).

In the above formulations the covariance matrix of the measurements W is used to account for the uncertainties in the measured apparent impedances, and is built from the users' specified standard deviation for each data point. The regularization matrix L is a discretization of a first order differential operator. When used in conjunction with the L1-norm on the regularization term, this corresponds to Total Variation regularization. The matrix can be anisotropic (horizontal or vertical) and specified by the user, in order to better reconstruct resistivity profiles that are stratified along one direction.

An early release of this approach has been successfully applied to process impedance data of several controlled experiments on laboratory scale (Borsic et al., 2005), where the electrodes effect on the final inversion results required a rigorous modelling, and also in processing of data sets collected in the field.

3.3 Application to synthetic data

To illustrate the effect of these choices on the norms to be used we report a series of simulations, which for simplicity are 2D, but the same results apply in 3D. In 3. 3 a 2D resistivity profile with a background of 100Ωm and two inclusions of 50 Ωm is shown. A 48 electrodes array was simulated and placed at the top of the domain and 545 simulated measurements (apparent impedances) were generated.

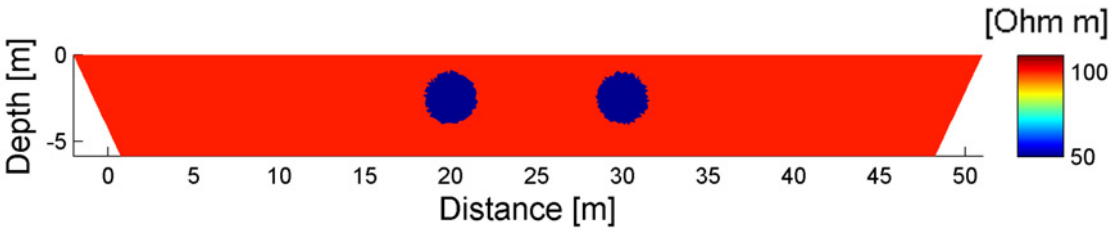

Fig. 3.3: Test resistivity profile used for generating synthetic data.

Original noiseless measurements are shown on the left of Figure 3.4. A 5% Gaussian noise was generated, as well as 20 outliers each one with amplitude of 50 Ω and random sign. These outliers have been added to the original dataset, as shown in the bottom part of Figure 3.4.

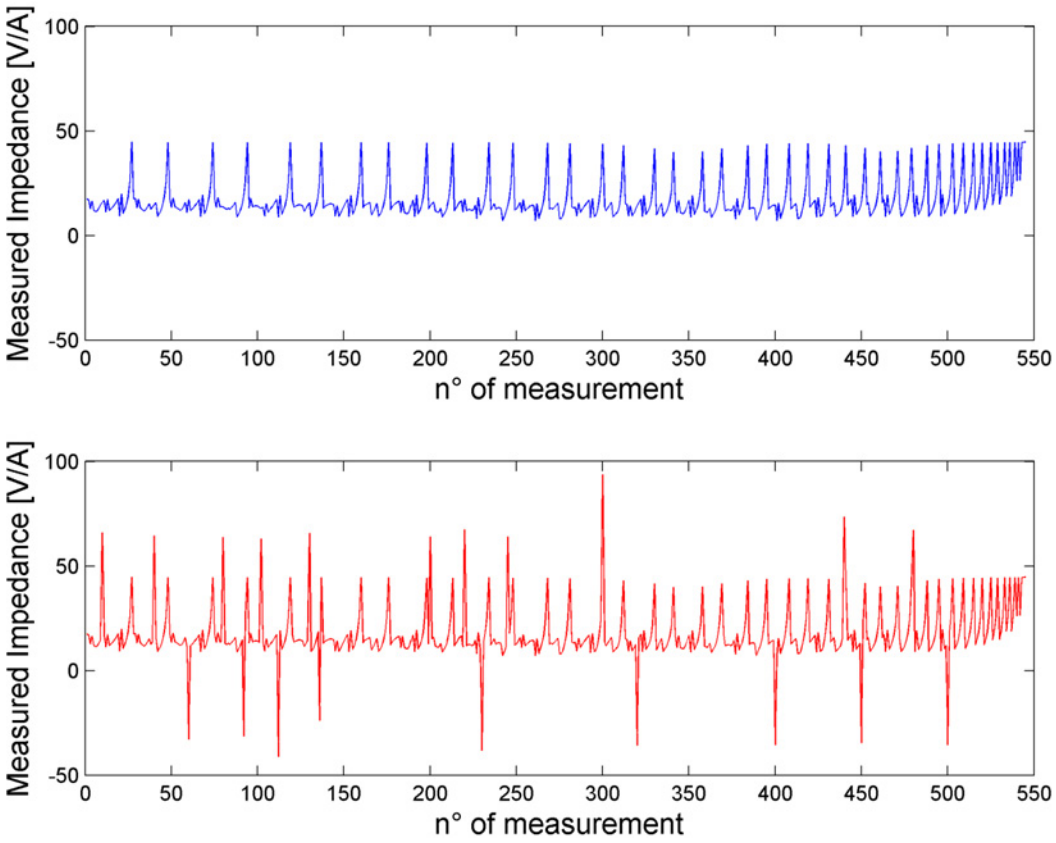

Fig. 3.4: Up) unperturbed synthetic data, bottom) data plus Gaussian noise and 20 outliers.

Figures 3.5 and 3.6 report reconstruction results respectively for data affected only by Gaussian noise and for data with Gaussian noise and outliers. The figures are organized in 2x2 tables, showing reconstructions for the four possible combinations on the L1 and L2 norms on the data and regularization terms of the inverse problem, as in Equations (1), (2), (3), and (4). In the presence of the Gaussian noise only (Figure 3.5) all formulations work correctly, and the two reconstructions in the right column, using the L1-norm as regularization, show a sharp estimation of the contrasts. When outliers are present, as in simulations of Figure 3.6, inversions based on the L2-norm on the data (top row of the table) are sensitive to the outliers, and the estimation is disrupted by these data errors. The resulting images depend on the value of the Tikhonov factor, and in all experiments we have optimized the Tikhonov factor in such a way to minimize the RMS difference between the reconstructed image and the original profile. For each case the reconstructions represent therefore the best possible result. Reconstructions using the L2-norm on the data show therefore how, even optimizing the value of the Tikhonov factor, it is a challenge to reconstruct the original contrasts. Inversion results based on the L1-norm on the data term (bottom row of the table) are instead insensitive to the presence of the outliers. The bottom

left reconstruction (L1 norm on the data and L2 norm on the regularization) can correctly identify the contrasts and reconstruct, even dough in a smooth way. The reconstruction on the bottom right (L1 norm on the data and L1 norm on the regularization) can correctly identify the contrasts and reconstruct them in a sharp manner.

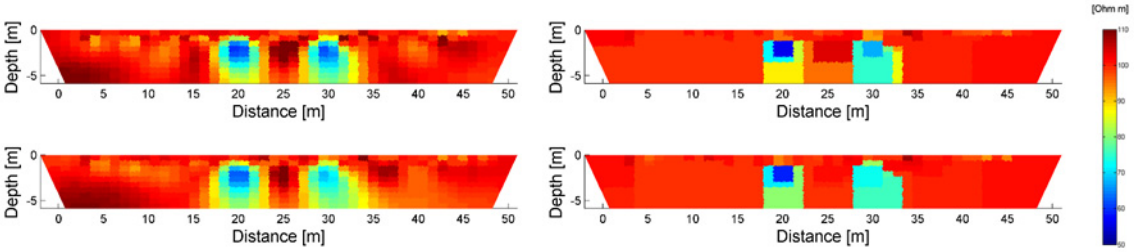

Fig. 3.5: Reconstructions of synthetic data, corrupted only by Gaussian noise for the four possible combinations of norms in the inverse formulations.

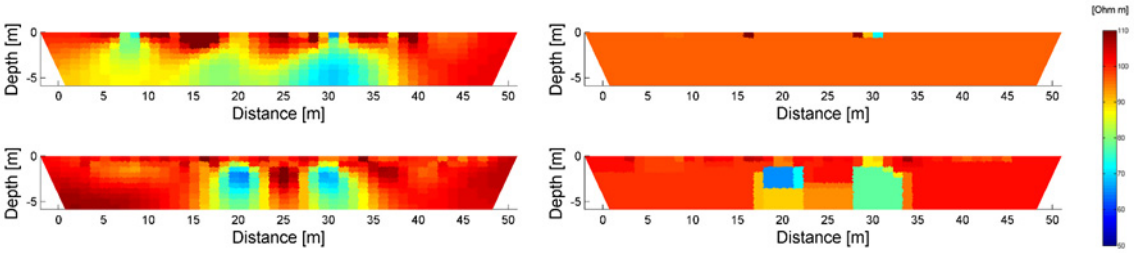

Fig. 3.6: Reconstructions of synthetic data, corrupted by Gaussian noise and outliers for the four possible combinations of norms in the inverse formulations.

A challenging case concerns a test on a synthetic 3-D model, which is showed in Figure 3.7 in the upper and lower figures on the left. Four boreholes are embedded in a homogeneous resistive half-space, with a high resistivity anomaly in the middle of the volume delimited by the boreholes. A 3D triangular mesh is used to simulate the presence of 4 boreholes (two visible and two hidden in the volume of the mesh itself). A set of synthetic measurements of complex resistivity is obtained for a dipole-dipole configuration. We show in Figure 3.7 simulations regarding the separate recovery of the real and imaginary part of the resistivity.

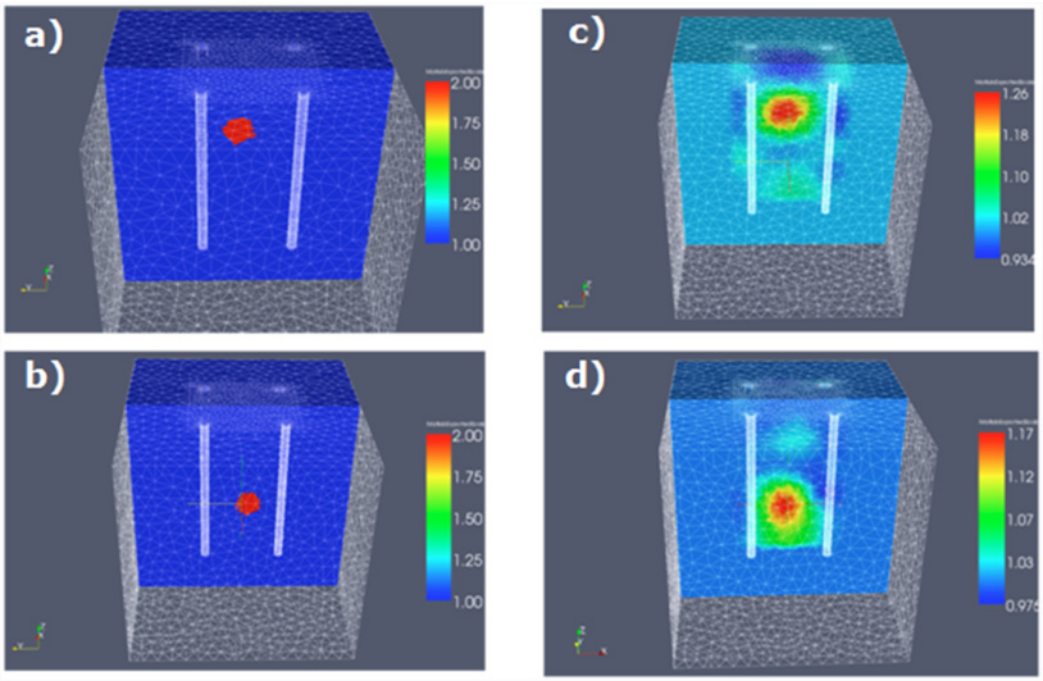

Fig. 3.7: Synthetic simulation of 3-D complex resistivity data (model and reconstruction are shown for the real part and the imaginary part on the top and on the bottom, respectively)

The top left picture shows a purely real contrast present in the top portion of the simulated cross-borehole region. The bottom left picture shows an imaginary valued contrast. The two contrasts where used for simulating complex valued measurements, and fed into the reconstruction routines. The top right image shows to the real part of the reconstructed resistivity, and the bottom right picture shows the reconstructed imaginary part of the resistivity. Clearly the real/imaginary contrasts are well separated and reconstructed. Presently the application to field data of complex reconstruction is challenging, as for typical values of permittivity of the soil and of measurement frequencies, the imaginary part of the measured impedances is very small in value and results in a very poor signal-to-noise ratio.

3.4 Application to real cases

The performance of the code has been tested on a series of datasets coming from various real applications. We chose four possible cases, considering 2-D and 3-D measurements with electrode deployments both on ground surface and in cross-hole fashion. Measurements were carried out on test-sites with known characteristics in terms of resistivity distribution.

A set of 2-D resistivity data has been acquired in 2010 at a research site of the National Research Council in Torino (Italy). As it can be seen in Figure 3.8, the site mainly consists of a resistivity

anomaly embedded in a homogeneous soil. The anomaly is a real 3-D feature, a basin filled with well-sorted coarse sand (Giubbolini and Sambuelli, 2000). It is highly permeable and mostly dry, providing high resistivity values if compared with the ones of the surrounding soil, which is mostly characterized by silty-sand.

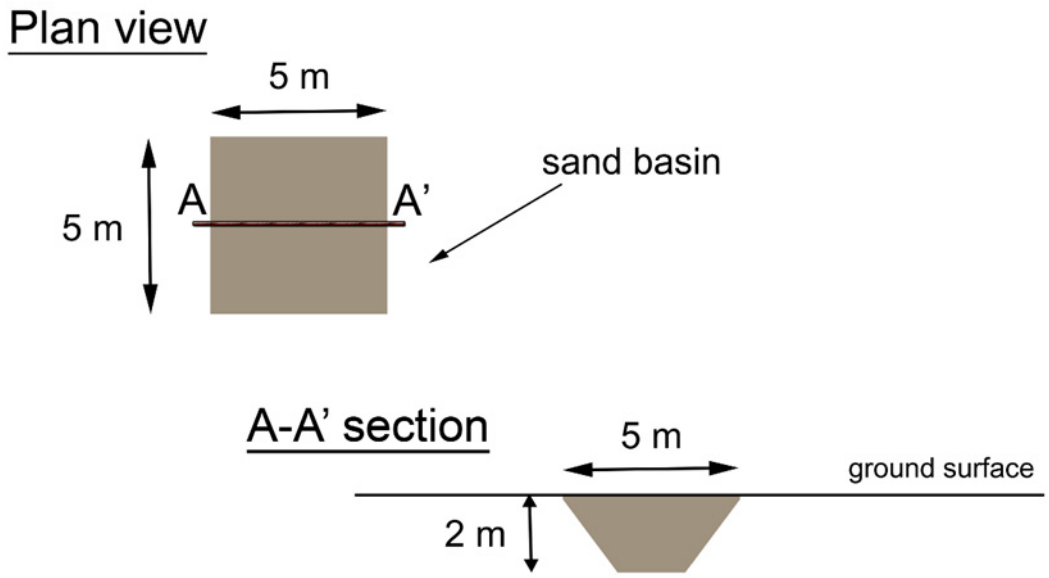

Fig.3.8: Description of the test site the National Research Council (CNR), Turin.

The data were acquired with a 48 electrode array, 1 m spaced, centered on the anomaly. In-line electrodes 21 and 26 have been placed at 21 and 26 m, respectively, at the boundaries between the sand basin and the soil around. A Wenner-Schlumberger configuration with 545 independent measures was selected.

For the 2-D case, we inverted the same dataset using all the four possible combination for the norms to be used.

The results are presented in Figure 3.9, respectively by solving the problem with Formulation 3.1 (Figure 3.9a), Formulation 3.2 (Figure 3.9b), Formulation 3.3 (Figure 3.9c) and Formulation 3.4 (Figure 3.9d).

The first two images show a smooth representation of the resistive basin, with the second one without the lateral tail besides the basin, meaning that the L1-norm has been insensitive to the presence of some outliers. The L1-norm on the regularization term gives very sharp results, as shown in (9c) and (9d).

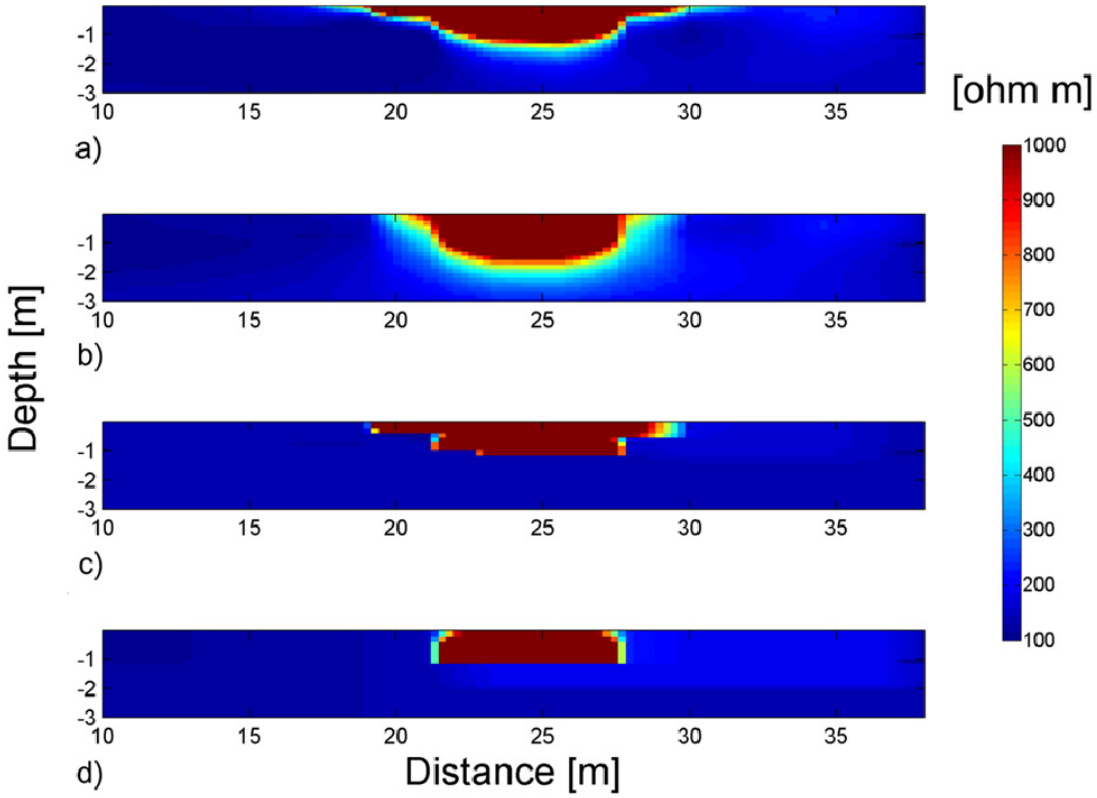

Fig.3.9: Resistivity images at the CNR tes site, surface 2-D acquisition. Results coming from Formulation 3.1 (a), 3.2 (b), 3.3 (c) and 3.4 (d), respectively.

The 3-D dataset was acquired at the same site described above, with a 144 electrode array, which were disposed as in Figure 3.10, centered on the anomaly. We used a pole-dipole array, placing the remote electrode 170 m far from the anomaly in the eastern direction. A data set of 6696 measurements was obtained by considering forward and reverse schemes along x- and y-direction, and furthermore along the two diagonals.

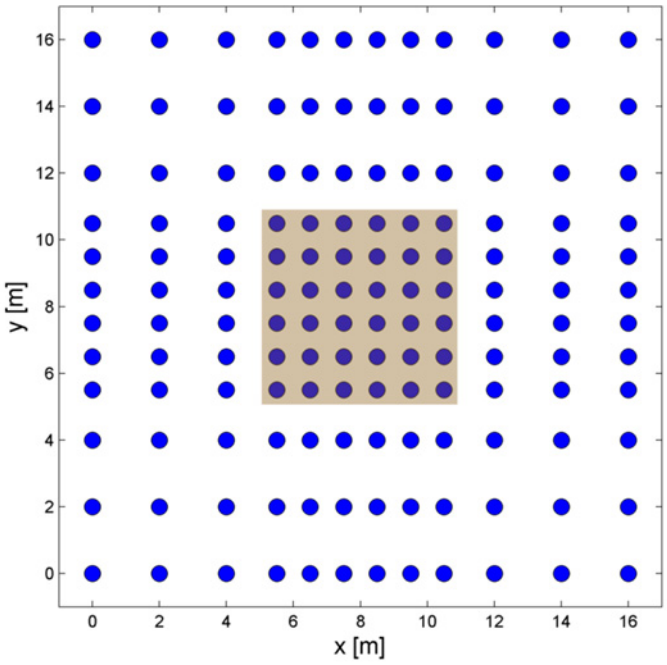

Fig.3.10: Electrode array for the surface 3-D survey, with a pole-dipole configuration, at the CNR test site, Turin.

In Figure 3.11 the results of the inversion on the surface 3-D dataset over the sand basin are presented. This result has been obtained by using the common Least Square implementation, then assuming Gaussian distribution of the errors over the dataset and a smooth regularization. The basin is well identified, and we observed high resistivity values down to 2 m, corresponding to the bottom of the basin. Even the global shape of the anomaly is preserved. On the right side of the figure some cut-through slices of resistivity at increasing depth are shown (from the top-left corner to the down-right corner).

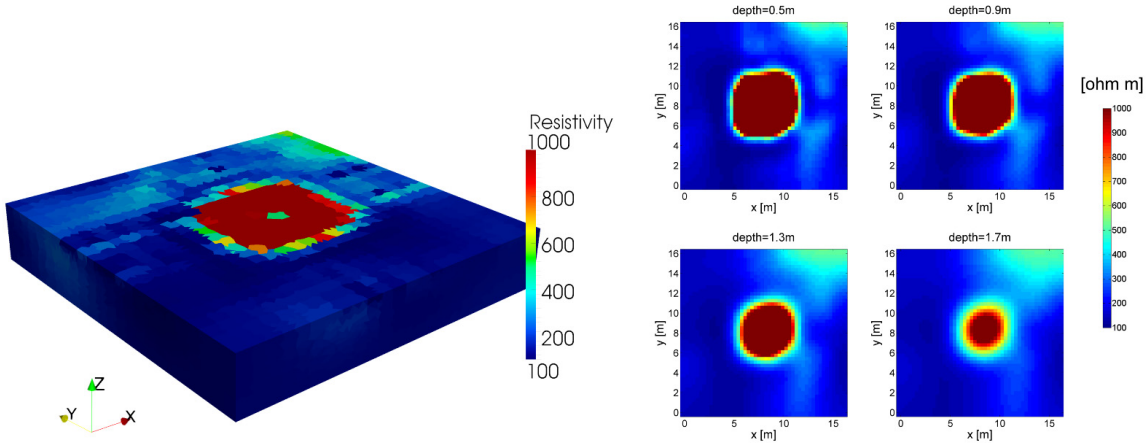

Fig. 3.11: Resistivity distribution for the surface 3-D case, CNR-Turin test-site, obtained with a common Least square formulation (L-2 norm both on the data and regularization term).

Sharper results on the same dataset were obtained by using the L-1 norm on the regularization term. The high contrast in resistivity values between the basin and the soil around permitted to regularize considering the absolute values on the "model" term, or Total Variation, of the objective function. In Figure 3.12 it is clear how the sharpness of the resistivity boundaries is preserved by the inversion, even though the reconstruction doesn't point out the real depth of the basin bottom, which is placed at 1.5 m instead of 2 m.

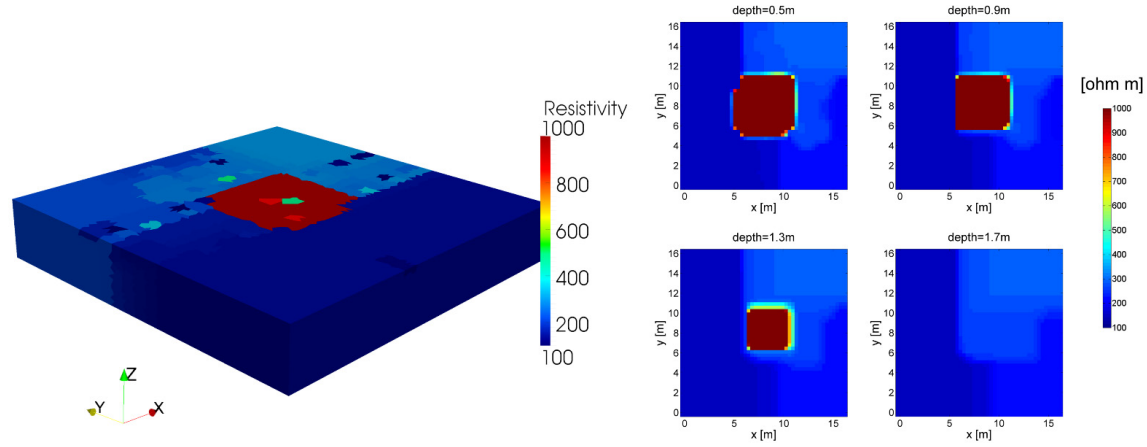

Fig.3.12: Resistivity distribution for the surface 3-D case, CNR-Turin test-site, obtained with the application of the L-2 norm on the data term and of the L-1 norm on the regularization term.

We tested the inversion code to a 3-D dataset coming from a test-site which is located in Gorgonzola, near Milan (Italy). The site belongs to the University of Milano Bicocca (Italy), and it is made up by three boreholes (b-A, b-B and b-C) which were installed in 2004 (see plan view in Figure 3.13). Each borehole is equipped with 24 electrodes 0.8 m spaced, in the depth range between 1.6 to 20 m from ground surface. One additional borehole (b-D), with no electrodes, was further installed for monitoring fate and transport processes during pumping tests and infiltration experiments.

The acquisition has been carried out in January 2011, by utilizing a dipole-dipole generalized array; the geological stratification of the site is reported in Figure 3.13.

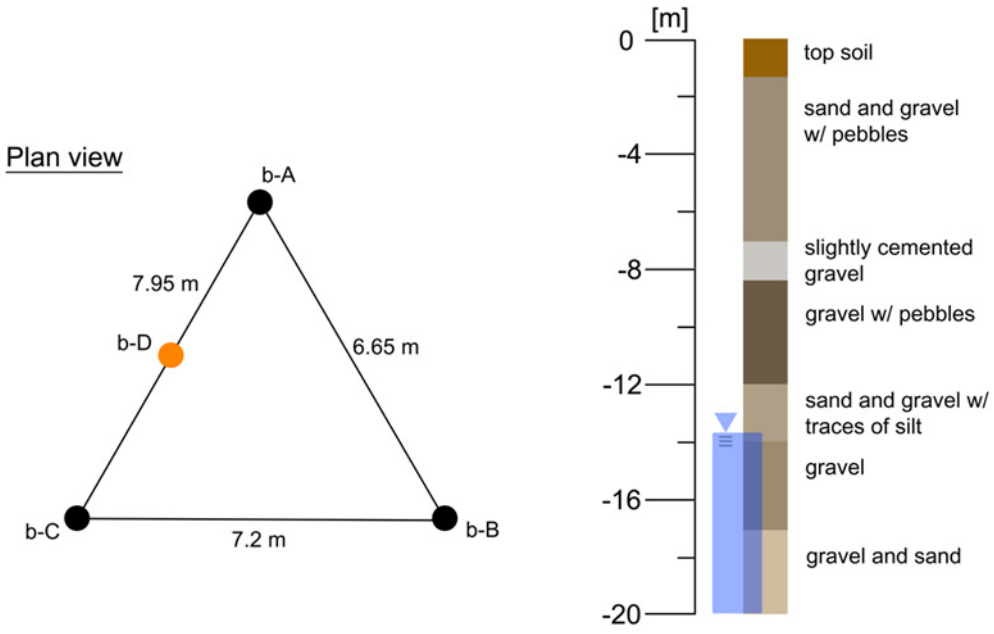

Fig. 3.13: Description of the geometry (left) and the soil stratigraphy (right) at the Gorgonzola test site.

Figure 3.14 shows the results of the inversion of resistivity data from the cross-hole 3-D case. This result has been achieved by using the common least square inversion, with slight horizontal anisotropy ratio. A tri-dimensional rendering of the resistivity distribution is shown on the left, indicating a resistive layer in the depth range between 6 and 11 m and corresponding to the layer of gravel with absence of finer material. The superficial and less resistive layer can be related to the presence of finer sand, while below 12 m a gradual transition towards low resistivity values indicates the presence of the saturated unconfined aquifer.

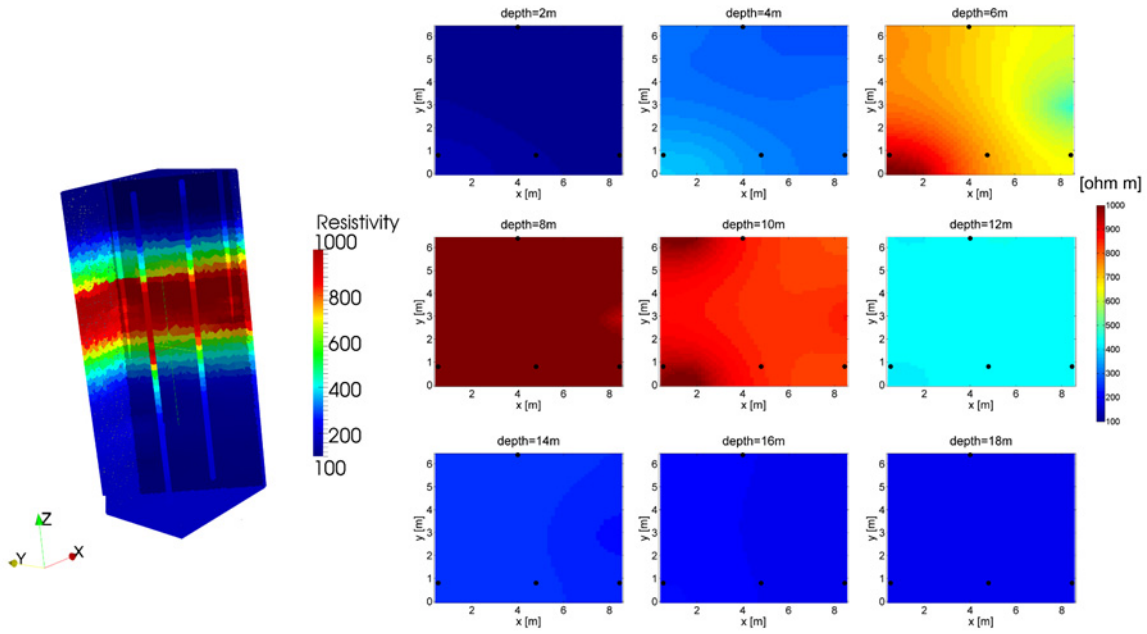

Fig. 3.14: Resistivity distribution for the cross-hole 3-D case, Gorgonzola test-site, obtained with a common Least square formulation (L-2 norm both on the data and regularization term).

3.5 Discussion and conclusions

A general limitation of ERT is the ill-posedness that image reconstruction presents. Ill-posedness can be limited by complementing reconstruction with data available from other sources (constrained reconstruction, use of prior information) and by using regularization techniques. On this front different solutions have been adopted in research work and in the software packages available in the public domain.

Cardarelli et al. (2006), for example, presented a 2D strategy based on an iterative smoothness-constrained least-squares algorithm; their approach ensures flexibility in resolution, by taking into account an initial arbitrarily defined model. They also introduced a priori information in different regions of the domain, using inequality constraints. Moreover they provided strategies to refine the mesh, to control the inversion procedure by a smoothness matrix and for controlling the regularization parameter (damping) at each iteration. Amongst the available non-commercial code, a well known package developed by Andrew Binley (Binley, 2010) performs forward/inverse solution 2D and 3D solutions using triangular and tetrahedral meshes. The inverse solution is based on a regularised objective function combined with weighted least squares, the so called Occam's type solution (Binley and Kemna, 2005). In comparison to the Binley's package, our approach provides a different flexibility in modeling the boreholes effects, allowing the user to

control the mesh density in 2D and 3D and provides several inversion schemes, allowing to choose the L1 or L2 norm of the data and regularization terms.

Smoothness constrains may lead to bias in the ERT inversion image (Friedel, 2003, Day-Lewis et al., 2005). The survey design (quantity and spatial arrangement of measurements), the distribution of electrical conductivity and the data error are the factors affecting the most the bias of the inverted image (Day-Lewis et al., 2005). Methods for solving 3-D problems often require significant computational efforts, in solving the sparse linear Equations resulting from the FEM model (Friedel, 2003; Day-Lewis et al., 2005) and in the parameter estimation (Yeh et al., 2002): these methods provide a rather qualitative measure of regions prone to bias, such as sensitivity analyses (Kemna et al., 2002). The so-called volume of investigation index (Oldenborger et al., 2007) may be an alternative to reduce these efforts. The package we presented in this paper aims at dealing efficiently with the computational cost of 3D solutions, but using 3D meshes that are adaptive, and by best exploiting modern PC architectures, which are multicore. When the L1 norm is used, a Primal Dual - Interior Point Method is employed for solving the resulting optimization problem, a method which is particularly efficient for L1 norm optimization.

The developing of an inversion approach of amplitude and phase of electrical data, including strategies to model the effects of boreholes and electrodes (in boreholes) represent an improvement with respect to the conventional approaches, allowing a more rigorous control of the electrodes and borehole effects on the inversion process with appreciable advantages when the electrodes' size is no longer negligible with respect to their distance, as this often occur in cross-hole survey.

The overall approach presented in this chapter is implemented in a software package based on the NES-GeoElectric library, that allows reconstruction of 2D and 3D electric impedance data optimized for speed and for parallel operation on multi-core computing architectures. NES-Geo-Electric has been coded as a Matlab toolbox, with core routines written in C language and optimized for performance. Our intention is to release soon the NES-GeoElectric package under a public domain licence.

References

Arato, A., A. Godio and L. Sambuelli, Staggered grid inversion of cross-hole resistivity data; submitted to Journal of Applied Geophysics, July, 2012.

Bastani, M., J. Hubert, T. Kalscheuer, L. Pedersen, A. Godio, and J. Bernard, 2012, 2D joint inversion of RMT and ERT data versus individual 3D inversion of full tensor RMT data. An example from Trecate site in Italy: Geophysics, 77, WB233-WB243, DOI: 10.1190/GEO2011-0525.1.

Binley, A., 2010, Free Resistivity Software R2 version 2.6 Generalised 2-D Inversion of Resistivity Data. http://www.es.lancs.ac.uk/people/amb/Freeware/freeware.htm

Binley, A., and A. Kemna, 2005, Electrical Methods, In: Hydrogeophysics by Rubin and Hubbard (Eds.), 129-156, Springer.

Bohm, G. and A. Vesnaver, 1999, In quest of the grid: Geophysics, 64, no. 4, 1116–1125.

Borsic, A., and A. Adler, 2012, A Primal Dual - Interior Point Framework for Using the L1-Norm or the L2-Norm on the Data and Regularization Terms of Inverse Problems: Inverse Problems, 28, No. 9, 095011, DOI:10.1088/0266-5611/28/9/095011.

Borsic, A., C. Comina, S. Foti, R. Lancellotta and G. Musso, 2005, Imaging heterogeneities in sand samples with Electrical Impedance Tomography: laboratory results: Geotechnique, 55, 539-647.

Borsic A., 2002, Regularization methods for imaging from electrical measurements. PhD Thesis, Oxford Brookes University, October 2002.

Bouchedda, A., M. Chouteau, A. Binley, B. Giroux, 2012, 2-D Joint structural inversion of cross-hole electrical resistance and ground penetrating radar data: Journal of Applied Geophysics, 78, 52-57.

Cassiani, G., V. Bruno, A. Villa, N. Fusi and A. M. Binley, 2006. A saline tracer test monitored via time-lapse surface electrical resistivity tomography, Journal of Applied Geophysics , 59, No. 3, 244-259.

Cassiani G., A. Godio, S. Stocco, A. Villa, R. Deiana, P. Frattini and M. Rossi, 2009, Monitoring the hydrologic behaviour of a mountain slope via time-lapse electrical resistivity tomography: Near Surface Geophysics, 7 , 475-486.

Cardarelli E., and F. Fischanger, 2006, 2D data modelling by electrical resistivity tomography for complex subsurface geology: Geophysical Prospecting, 54, No. 2, 121–133, DOI: 10.1111/j.1365-2478.2006.00522.x

Cheng K. S., D. Isaacson, J. C. Newell, and D. G.Gisser, 1989, Electrode Models for Electric Current Computed Tomography: IEEE Transactions in Biomedical Engineering, 36, No. 9, 918-924.

Cohen, A., W. Dahmen, and R. DeVore, 2003, Adaptive wavelet schemes for nonlinear variational problems: SIAM J. Numerical Analysis, 41, No. 5, 1785–1823.

Comina, C., and L. Sambuelli, 2012, Geoelectrical measurements for agricultural canal seepage detection: Proceedings Near Surface Geoscience 2012 -18th Meeting on Environmental and Engineering Geophysics - Paris, 3-5 Sep., paper n. C.34, 5pp.

Day-Lewis, F. D., K. Singha, and A. M. Binley, 2005, Applying petrophysical models to radar travel time and electrical resistivity tomograms: Resolution-dependent limitations: Journal of Geophysical Research, 110, B08206, DOI:10.1029/2004JB003569.

Friedel, S., 2003, Resolution, stability and efficiency of resistivity tomography estimated from a generalized inverse approach: Geophysical Journal International, 153, 305–316.

Giubbolini L., and L. Sambuelli, 2000, New developments in ground probing radar: the possibility of reconstruction of a holographic image of underground reflectivity: Annali di Geofisica, 43, 1105-1118.

Godio A., and M. Naldi, 2003, Two dimensional electrical imaging for detection of hydrocarbon contaminants: Near Surface Geophysics, 1, 131-137.

Godio A., and S. Ferraris, 2005, Time lapse geophysics for monitoring an infiltration test in vadose zone: Bollettino di Geofisica Teorica e Applicata, 46, 201-216.

Godio A., and M. Naldi, 2009, Integration of Electrical and Electromagnetic Investigation for Contaminated Site: American Journal of Environmental Sciences, 5, 561-568, ISSN: 1553-345X.

Godio, A., A. Arato, and S. Stocco, 2010, Geophysical characterization of a nonaqueous-phase liquid–contaminated site: Environmental Geosciences, 17, 141-162.

Godio, A., A. Borsic, A. Arato, and L. Sambuelli, 2011, On the inversion of cross-hole resistivity data: Geophysical Research Abstracts, 13, EGU2011-7950.

Hyvonen, N., 2004, Complete electrode model of electrical impedance tomography: approximation properties and characterization of inclusions: SIAM Journal on Applied Mathematics, 64, No. 3, 902–931.

Kemna A., B. Kulessa, and H. Vereecken, 2002, Imaging and characterisation of subsurface solute transport using electrical resistivity tomography (ERT) and equivalent transport models: Journal of Hydrology, 267, 125-146.

Kemna A., A. Binley, and L. Slater, 2004, Crosshole IP imaging for engineering and environmental applications: Geophysics, 69, No. 1, 97-107.

LaBrecque, D.J., G. Morelli, W. Daily, A. Ramirez, and A. Lundegard, 1999, Occam's inversion of 3-D electrical resistivity tomography: in Three-Dimensional Electromagnetics, 575–590, eds Oristaglio, M. & Spies, B., Soc. Expl. Geophys., Tulsa , OK.

Maurer, H. and S. Friedel, 2006, Outer-space sensitivities in geoelectrical tomography, Geophysics, 71, No. 3, G93–G96.

Michelini, A., 1995, An adaptive-grid formalism for travel-time tomography: Geophysical Journal International, 121, No. 2, 489–510.

Morelli, G. and D.J. LaBrecque, 1996, Advances in ERT inverse modeling: European J. Environmental and Engineering Geophysics, 1, 171–186.

Oldenborger, G.A., P.S. Routh, and M.D. Knoll. 2007, Model reliability for 3D electrical resistivity tomography: Application of the volume of investigation index to a time-lapse monitoring experiment: Geophysics, 72, F167–F175.

Plattner, A., H. R. Maurer, J. Vorloeper, and M. Blome, 2012, 3-D electrical resistivity tomography using adaptive wavelet parameter grids: Geophysical Journal International, 189, 317–330, DOI:10.1111/j.1365-246X.2012.05374.x.

Rücker, C. and T. Günther, 2011, The simulation of finite ERT electrodes using the complete electrode model: Geophysics, 76, No. 4, F227-F238, DOI: 10.1190/1.3581356.

Sambuelli, L., L. V. Socco, A. Godio, G. Nicolotti, and R. Martinis, 2003, Ultrasonic, electric and radar measurements for living trees assessment: Bollettino di Geofisica Teorica ed Applicata, 44, No. 3-4, 253-279.

Somersalo, E., M. Cheney and D. Isaacson, 1992, Existence and Uniqueness for Electrode Models for Electric Current Computed Tomography: SIAM Journal on Applied Mathematics, 52, No. 4, 1023-1040.

Strobbia C., A. Godio, and G. De Bacco, 2006, Interfacial waves analysis for the geotechnical characterization of marine sediments in shallow water: Bollettino di Geofisica Teorica e Applicata, 47, 145-162.

Tikhonov, A. N., and V. Y. Arsenin, 1977, Solutions of Ill-Posed Problems: Winston & Sons Washington D.C.

Yeh, T.C.J., S. Liu, R. J. Glass, K. Baker, J. R. Brainard, D. Alumbaugh, and D. LaBrecque, 2002, A geostatistically based inverse model for electrical resistivity surveys and its applications to vadose zone hydrology: Water Resources Research, 38, No. 12, 1278, http: //dx.doi.org /10.1029/2001WR001204.

4. Time-lapse inversion of electrical resistivity data

This chapter is aimed to furnish an overview of the basics of inversion of resistivity data in time-lapse fashion, with further applications of a novel method on synthetic and real 2-D cross-hole data.

The dynamic characterization of a site is necessary when the inference of variations of geophysical parameters with time is needed. ERT, particularly in cross-hole configuration due to limited lack of resolution with depth, is a reliable technique for long-term monitoring of the effects of the groundwater fluctuations of an unconfined superficial aquifer in a contaminated site. Superficial water resources are the first sensible target of anthropogenic contamination, and this reason encouraged many authors (e.g. Slater et al., 2000; Cassiani et al., 2006) to study the applicability of ERT for monitoring controlled field infiltration tests. The results of such these tests provided qualitative and quantitative information on hydrological parameters of the soil, which mainly control flow and transport phenomena through the aquifer geological formations. Other authors (e.g. Godio and Naldi, 2003; Atekwana et al., 2004a, 2004b, 2004c, 2004d) have investigated the application of ERT to characterize and monitor hydrocarbon contaminated sites.

4-D analysis of electrical resistivity data has to take into account a series of factors that contribute to the overall spatial and temporal variability of the resistivity distribution in the considered soil system. Particular importance has to be attributed to those phenomena influencing the pore-fluid saturation and the fluid composition, under the assumption of invariance of the electrical characteristics of the soil matrix.

The most simple method for understanding the temporal behaviour of resistivity with ERT is to compare inversion results making the ratio of inverted resistivity from two subsequent datasets. However, this method can introduce severe errors in the interpretation of time-lapse changes. In fact, each resulting image is diversely affected by inversion artefacts that come from measurement errors and systematic errors (due, for instance, to misplacement of the electrodes), which are usually augmented by the optimization process.

In order to overcome this problem, Daily et al. (1992) proposed the so-called ratio method, with consists in inverting the dataset of fictitious resistances

$$R_r = \frac{R_t}{R_0} R(F_{hom}) \tag{4.1}$$

where the ratio resistance dataset is made up by dividing dataset of resistances at time t (R_t) with respect to the background dataset R_0, and multiplying this ratio by a synthetic dataset of resistance values $R(F_{hom})$. $R(F_{hom})$ comes from the solution of the direct problem for an electrically homogenous half-space, i.e. with constant resistivity of ρ_{hom}. The result of the inversion of R_r show a distribution of resistivity whose values are higher or lower than ρ_{hom} in correspondence of the zones of increment or decrement of resistivity from time 0 to time t. However, the ratio method only gives qualitative information on the resistivity changes, and it is difficult to give a quantitative interpretation of the time-lapse results.

Miller et al. (2008) proposed what they called “cascaded” time-lapse inversion algorithm. Cascaded inversion uses the result of a single inversion of the background dataset as starting and reference model during the inversion. The main hypothesis is that the resistivity distribution doesn’t change significantly with time, thus the subsequent model can be considered similar to the background model. The minimization is based on the difference between the model at time t and the background resistivity model, and the smoothing is applied to the difference between the two subsequent models, instead of being placed as a constraint to the second model. Naturally, this approach is robust when changes in the electrical condition of the soil system are small between the different time-steps.

A slightly different approach was studied by LaBrecque and Yang. (2001), who developed a time-lapse difference inversion method which is aimed to minimize the data differences from two subsequent datasets, and the difference between the forward response of the two models. As in Miller et al. (2008), the method requires a background resistivity model which comes from the inversion of the background dataset.

Both the cascaded and the difference method are then sensitive to noise amplification (artefacts) during inversion of the background datasets, and the solution of the time-lapse differences can be affected by artefacts from the background inversion result.

In 2009 Kim et al. provided a new formulation for time-lapse inversion, adding a parameter into the objective function to account for the temporal resistivity variations. The prerogative of this method is the assumption of temporal linearity, meaning that the global electrical characteristics of the investigated medium change linearly between one time step to the subsequent one.

Hayley et al. (2011) developed a time-lapse method based on the concept of the spatially constrained inversion, in order to ensure smooth changes from subsequent time steps. The smoothness constraints are placed within a single optimization problem, claiming for a limitation of the propagation artefacts from the background model.

Our necessity of dealing with systems characterized by highly dynamic changes forced us to find simple but reliable methods to perform time-lapse analysis of electrical resistivity data.

In Chapter 2.2, a demonstration of the possibility to check the precision of inversion result from SGERT has been provided. We take advantage from this peculiarity with the aim to apply the SGERT to time-lapse analysis of electrical resistivity data.

In presence of artefacts in the resulting image on the background dataset, unreal resistivity changes will propagate in the differences with respect to subsequent times. The best the definition of the background resistivity model is, the more reliable the time-lapse differences will be. As previously presented, the SGERT produces two resulting matrix, representing the distribution of average resistivity and the related standard deviation.

Standard deviation distribution is indicative of the precision (i.e. repeatability) of the inversion in each of the pixels resulting from the staggering and re-sampling of the different grids used for SGERT.

High standard deviation values were found in correspondence of high model sensitivity zones (mostly near the electrodes and along the boreholes) and in zones differently reconstructed on the various grids. This occurs along resistivity boundaries and in areas of the model where the resistivity features were inconsistent. For this reason, SGERT are usually characterized by less artefacts.

4.1 Application of SGERT to time-lapse Electrical Resistivity Tomography

The possibility to account for the precision of the final resistivity inversion, pixel per pixel, using the relative standard deviation distribution, encouraged us to use SGERT method for the inversion of time-lapse resistivity data. Obviously, standard deviation (referred to as σ, which has not to be confounded here with electrical conductivity) is intimately linked to the average resistivity distribution, since the grid staggering operates in a different way on the same dataset but on the different grids in the staggering process.

The 2-D distribution of the inversion precision from the SGERT method is given by

$$P(x,y) = 1 - \frac{\sigma(x,y)}{\hat{\rho}(x,y)} \tag{4.2}$$

Each pixel in the x- and y- direction is assigned a value of average resistivity $\hat{\rho}$, and standard deviation σ.

The parameter P gives a good estimate of the coherency of resistivity reconstruction on the different staggered grids. This was shown in Chapter 2 for the standard 2-D cross-hole inversion. This prerogative of the SGERT technique, accompanying a reduction of inversion artefacts and the characteristic to solve less under-determined problems, encouraged us to apply it to the time-lapse analysis of temporally varying electrical cases.

The basic relation for the time-lapse analysis between two different resistivity distributions ρ_t and ρ_0, respectively the resistivity at time t

$$\Delta\rho_{t-0} = \frac{\rho_t - \rho_0}{\rho_0} * 100 \ [\%] \tag{4.3}$$

Let P_t and P_0 be defined as the precision at time t and at the background time, respectively. The time-lapse precision can be defined as the product of P_t and P_0

$$P_{TL}(x,y) = P_t(x,y) \cdot P_0(x,y) \ \in [0,1] \tag{4.4}$$

P_{TL} combines the information about the precision for the background and the subsequent resistivity distributions, and it exhibits values in the range between 0 and 1. It is clear that low precision in the background result will influence the time-lapse precision, giving an indicator of the global repeatability of the time-lapse result, pixel per pixel.

A useful parameter for evaluating the behaviour of time-lapse resistivity is what we call here precision “accordance”, defined as

$$A_{TL}(x,y) = P_t(x,y) / P_0(x,y) \tag{4.5}$$

A_{TL} is a non-dimensional parameter, which shows a correlation between P_t and P_0 and it can be used to estimate the real spatial distribution of the precision values in time-lapse. A_{TL} = 1 obviously means equal precision values with respect to the background precision. Pixels characterized by $A_{TL} > 1$ will indicate the low-precision zones in the background case, viceversa $A_{TL} < 1$ will show the movement of the low-precision zones in the subsequent case. This can be utilized as a good estimate of the temporal evolution trend of the resistivity boundaries over the investigated domain.

4.2 Joint use of staggered grid and difference inversion

We used the difference inversion algorithm proposed by LaBrecque and Yang (2001), encoded in the R2 package code (Binley, 2010).

As stated in the previous paragraph, difference inversion is an extension of the traditional Occam's inversion, carried out by minimizing the objective function $\psi(\mathrm{m})$

$$\psi(\mathrm{m}) = \Delta\mathrm{D}^{\mathrm{T}}\mathbf{W_D}\ \Delta\mathrm{D} + \alpha\ (\mathbf{m} - \mathbf{m_0})^{\mathrm{T}}\mathbf{R}(\mathbf{m} - \mathbf{m_0}) \tag{4.6}$$

where $\mathbf{W_D}$ is the data weighting matrix, α is the damping factor, **R** the model regularization (or roughness) matrix, while m and m_0 correspond to the model parameter vectors at time t and 0, respectively.

The vector parameter $\mathbf{m_0}$ comes from a single inversion of the background dataset, and constitutes the starting and the reference model for the difference inversion process.

The data difference vector in the objective function of Equation (4.6) has the form

$$\Delta\mathrm{D} = (\mathbf{d}^{\mathbf{obs}} - \mathbf{d}_{\mathbf{0}}^{\mathbf{obs}}) - [\mathrm{g}(\mathbf{m}) - \mathrm{g}(\mathbf{m_0})] \tag{4.7}$$

where d^{obs} and g(m) represent the data vector and the forward response for the model m, respectively, and the subscript index "0" denotes the background dataset and forward response.

The model update $\Delta m=m_{k+1}-m_k$ is obtained by solving the following Equation as an optimization problem, usually with a conjugate-gradient approach,

$$(\mathbf{J}_{\mathrm{k}}^{\mathrm{T}}\mathbf{W}_{\mathrm{D}}\mathbf{J}_{\mathrm{k}} + \alpha\cdot\mathbf{R})\Delta\mathbf{m} = \mathbf{J}_{\mathrm{k}}^{\mathrm{T}}\mathbf{W}_{\mathrm{D}}\Delta\mathbf{D} + \alpha\cdot\mathbf{R}(\mathbf{m}_{\mathrm{k}} - \mathbf{m_0}) \tag{4.8}$$

where J is the Jacobian (i.e. sensitivity) matrix.

Difference inversion is computationally efficient since the method is based on the calculation of one Jacobian matrix, which is supposed to describe adequately the sensitivity distribution of both the model at time t and the background model. This assumption implies that the resistivity changes are not so great, and the process is oriented to find small perturbation with respect of the initial model.

However, LaBrecque and Yang (2001) demonstrated the effectiveness of the method in reducing inversion artefacts on real cases with highly contrasting resistivity layers, dealing with time-lapse data characterized by great resistivity changes and high percent of noise.

For this reason we make use of joint SGERT method with difference inversion algorithm (named SGDERT in the following) for highly dynamic environments, combining the benefits of difference inversion and the effect of time-lapse precision assessment coming from SGERT.

To demonstrate the effectiveness of this approach, we apply it both on synthetic and real cross-hole data.

4.3 Application to synthetic data

The performance of the SGDERT technique is evaluated by inverting datasets from two very simple synthetic time-lapse cases, shown in Figure 4.1 and Figure 4.2.

The electrode arrangement is the same as in 2-D cross-hole cases presented in chapter 2.

The first synthetic time-lapse case represents a common geological situation of sedimentary superficial aquifers, with a resistive (1000 ohm m)sandy layer overhanging a saturated half-space with a bulk resistivity of 100 ohm m. Any effect of smoothing due to the presence of a capillary fringe is neglected in these particular cases. The time-lapse resistivity evolution simulates the rise-up of the water table, from a depth of 9 to 6 m below the ground surface. The opposite situation characterizes the second time-lapse case, which simulates the water level drop from a depth of 6 to 9 m below ground surface (b.g.s).

The time-lapse differences for the two cases are completely different, with 90% negative relative decrease in the oscillation zone for the first case, while the resistivity increase in the second case implies a positive relative increase of about 900%.

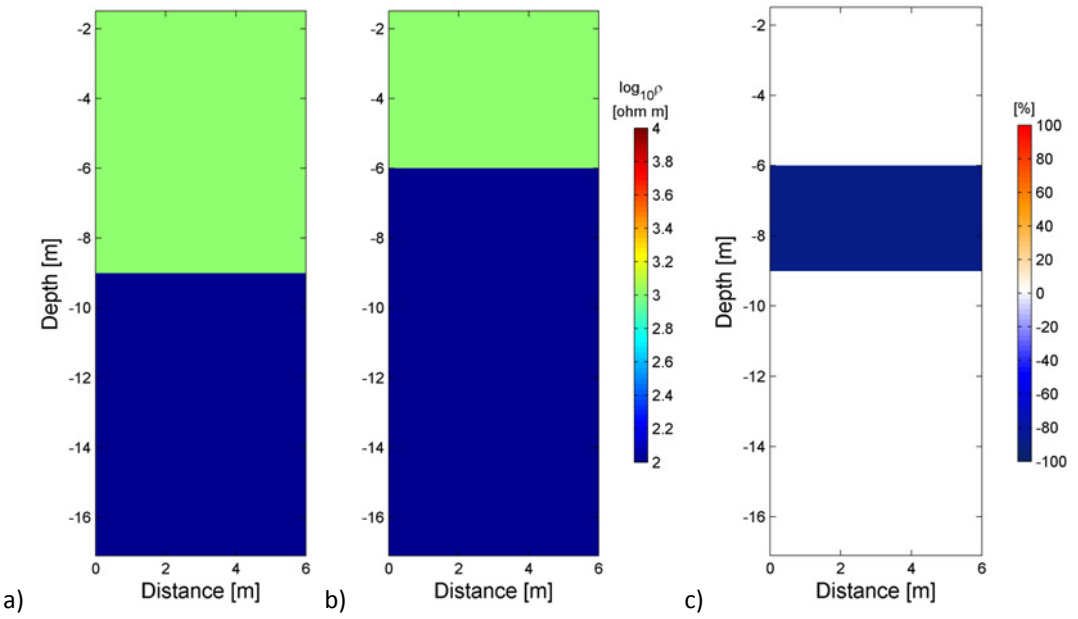

Fig. 4.1: Synthetic time-lapse model n. 1: a) background resistivity; b) resistivity at time t; c) relative resistivity difference.

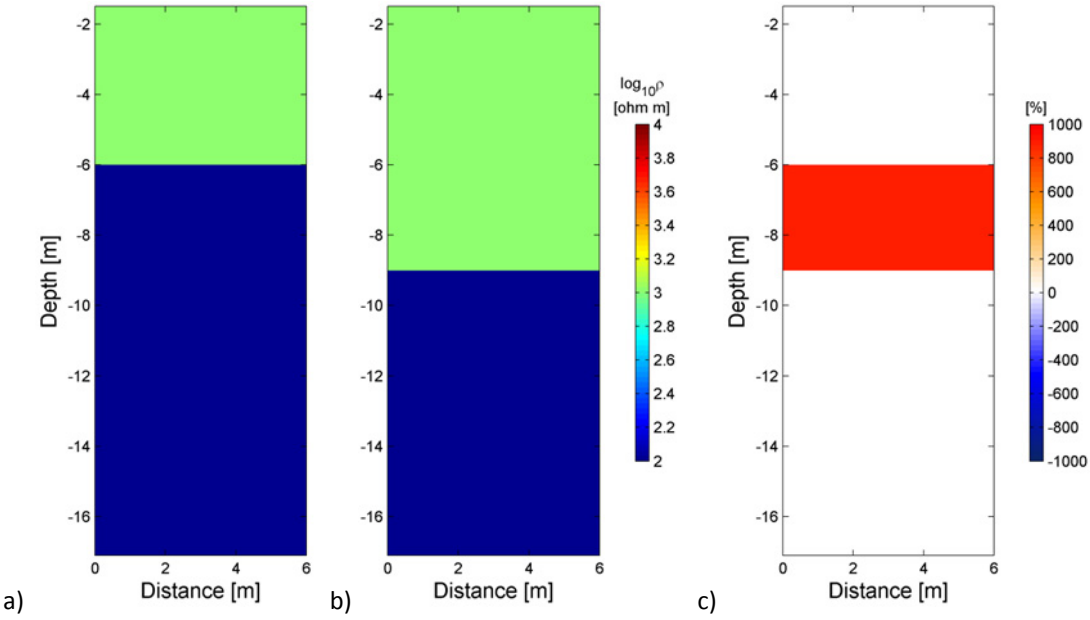

Fig. 4.2: Synthetic time-lapse model n. 2: a) background resistivity; b) resistivity at time t; c) relative resistivity difference.

Two separate data sets of 1200 resistance values (in Ω) were obtained for a pole-dipole array. We inverted the synthetic dataset using the R2 code fixing a data error to be slightly conservative (i.e. imposing error level slightly greater than the real error level in the data from the forward solution) on the real error level on the data. We choose the maximum number of iteration to be equal to 10. The optimal smoothing factor is updated by the code at each iteration, and it was

properly set to have a smooth model along the horizontal direction, as it is usually done to follow the horizontal geological layers.

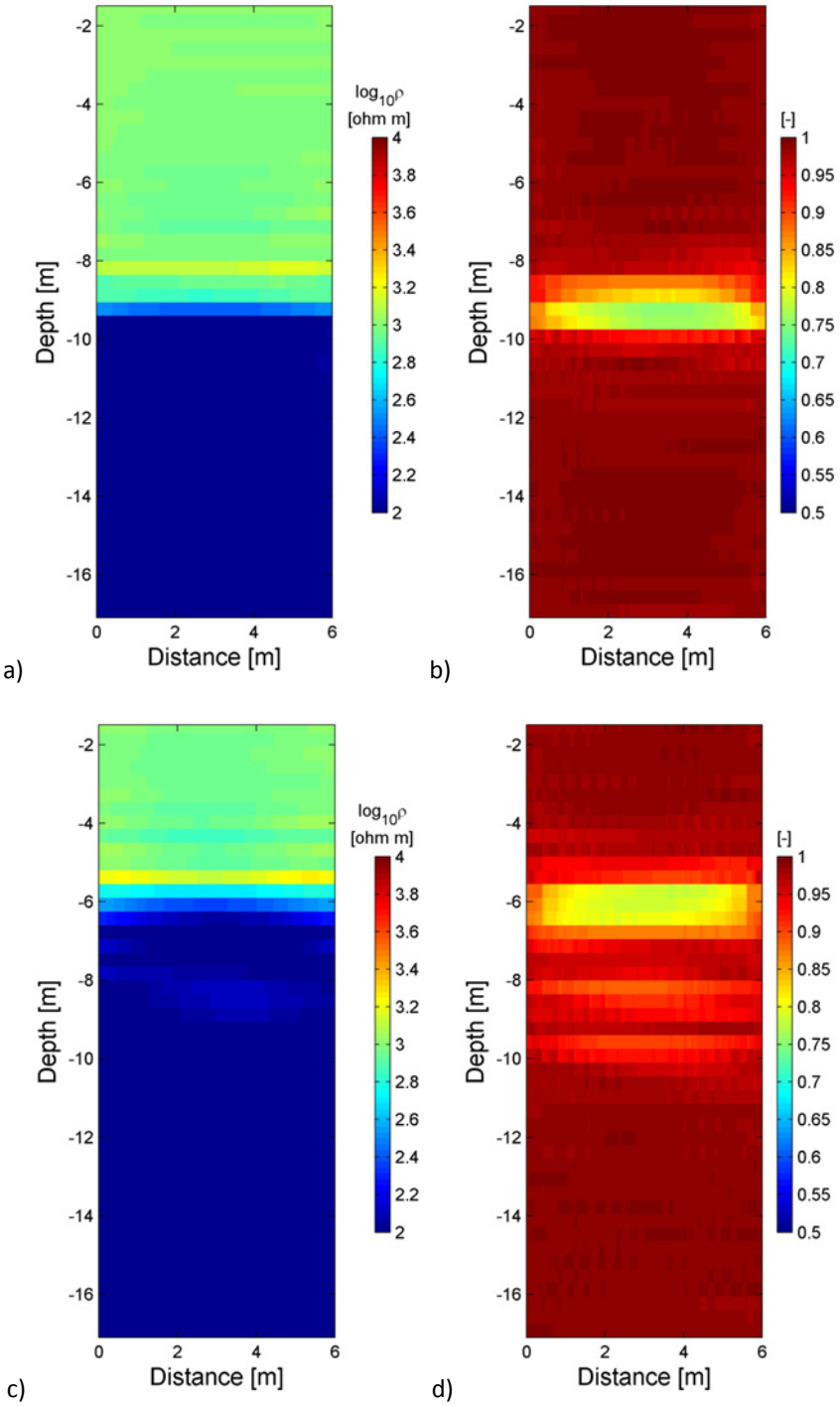

Fig. 4.3: Synthetic time-lapse model n. 2 (noise-free data), results from the SGERT inversion: image of average resistivity for the background (a) and the subsequent (c) case, precision P_0 (b) and P_t (d).

Results of the SGDERT on the first synthetic model are shown in Figure 4.3. Figure 4.4 reports the time-lapse resistivity differences and the time-lapse precision and accordance.

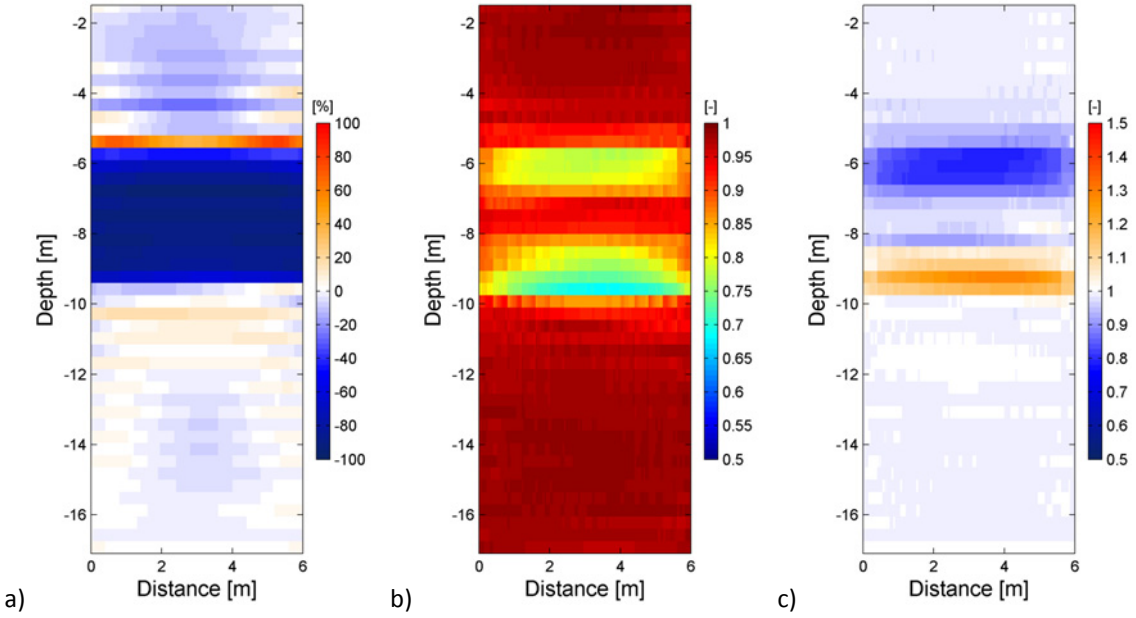

Fig. 4.4: Synthetic time-lapse model n. 1 (noise-free data), results from the SGERT inversion: image of (a) time-lapse percent resistivity difference (b) time-lapse precision P_{TL} and c) precision accordance.

Analogous considerations can be given for the synthetic time-lapse case n. 2, regarding the results of the application of the SGDERT method to noise-free resistance data. Results are shown in Figure 4.5 and 4.6.

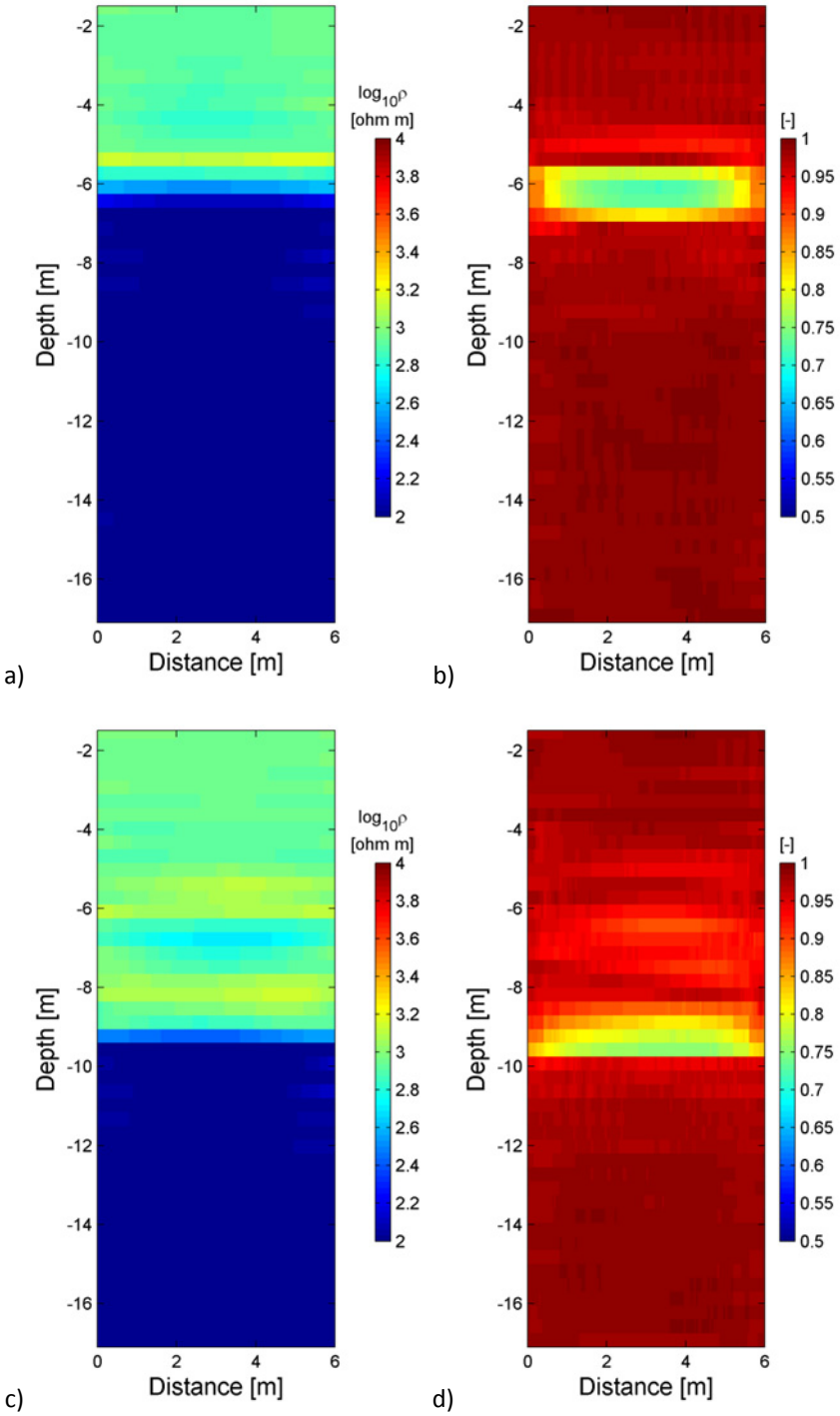

Fig. 4.5: Synthetic time-lapse model n. 2 (noise-free data), results from the SGERT inversion: image of average resistivity for the background (a) and the subsequent (c) case, precision P_0 (b) and P_t (d).

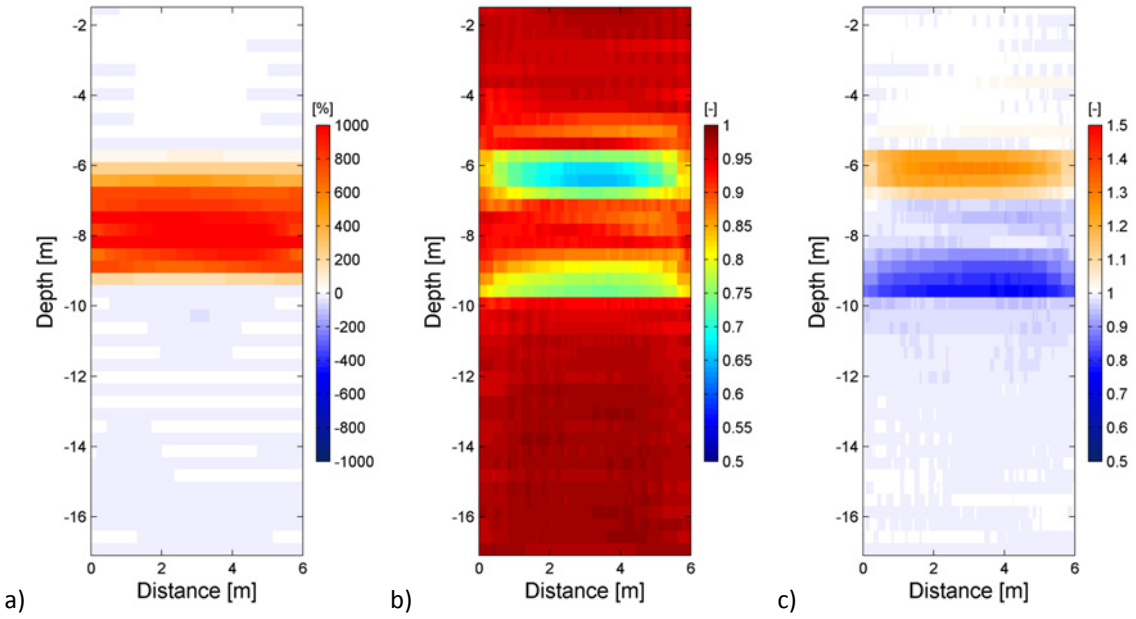

Fig. 4.6: Synthetic time-lapse model n. 2 (noise-free data), results from the SGERT inversion: image of (a) time-lapse percent resistivity difference (b) time-lapse precision P_{TL} and c) accordance.

The same approach has been applied to the same time-lapse cases, whose resistance data had been added of 10% Gaussian noise.

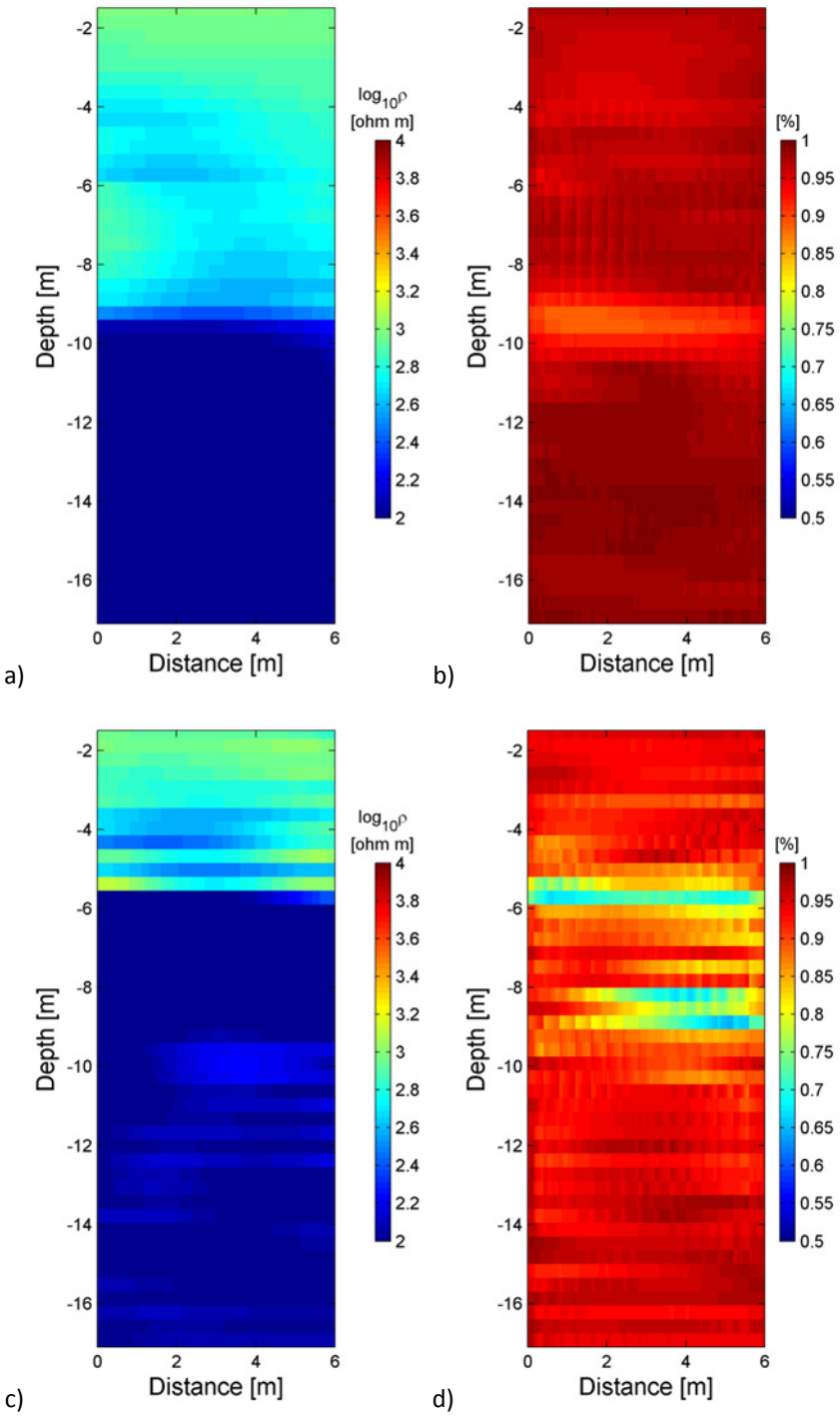

Fig. 4.7: Synthetic time-lapse model n. 1 (10% noise data), results from the SGERT inversion: image of average resistivity for the background (a) and the subsequent (c) case, precision P_0 (b) and P_t (d).

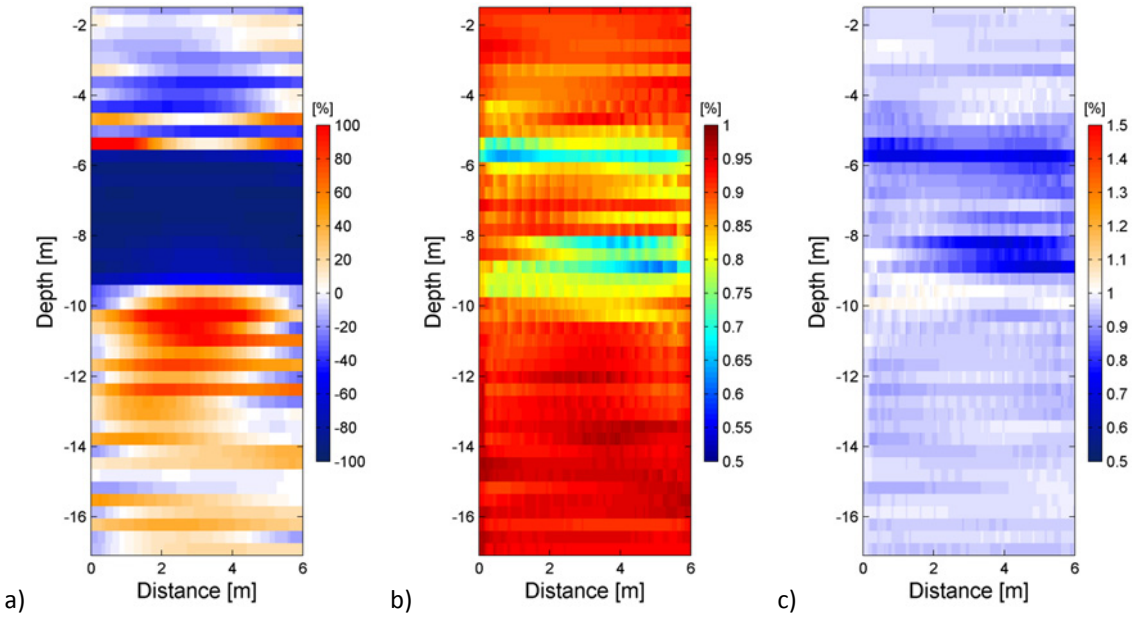

Fig. 4.8: Synthetic time-lapse model n. 1 (10% noise data), results from the SGERT inversion: image of (a) time-lapse percent resistivity difference (b) time-lapse precision P_{TL} and c) accordance.

The presence of noise on the data heavily affects the reconstruction, since the inversion method is a common least square formulation. Then the overall geometry arrangement of the electrical strata is preserved, and addressed by the precision and accordance distributions, but the method shows some limits in giving an accurate estimate of the resistivity differences.

Results of the application of SGDERT to the noisy data from the second synthetic case are shown in Figure 4.9 and 4.10.

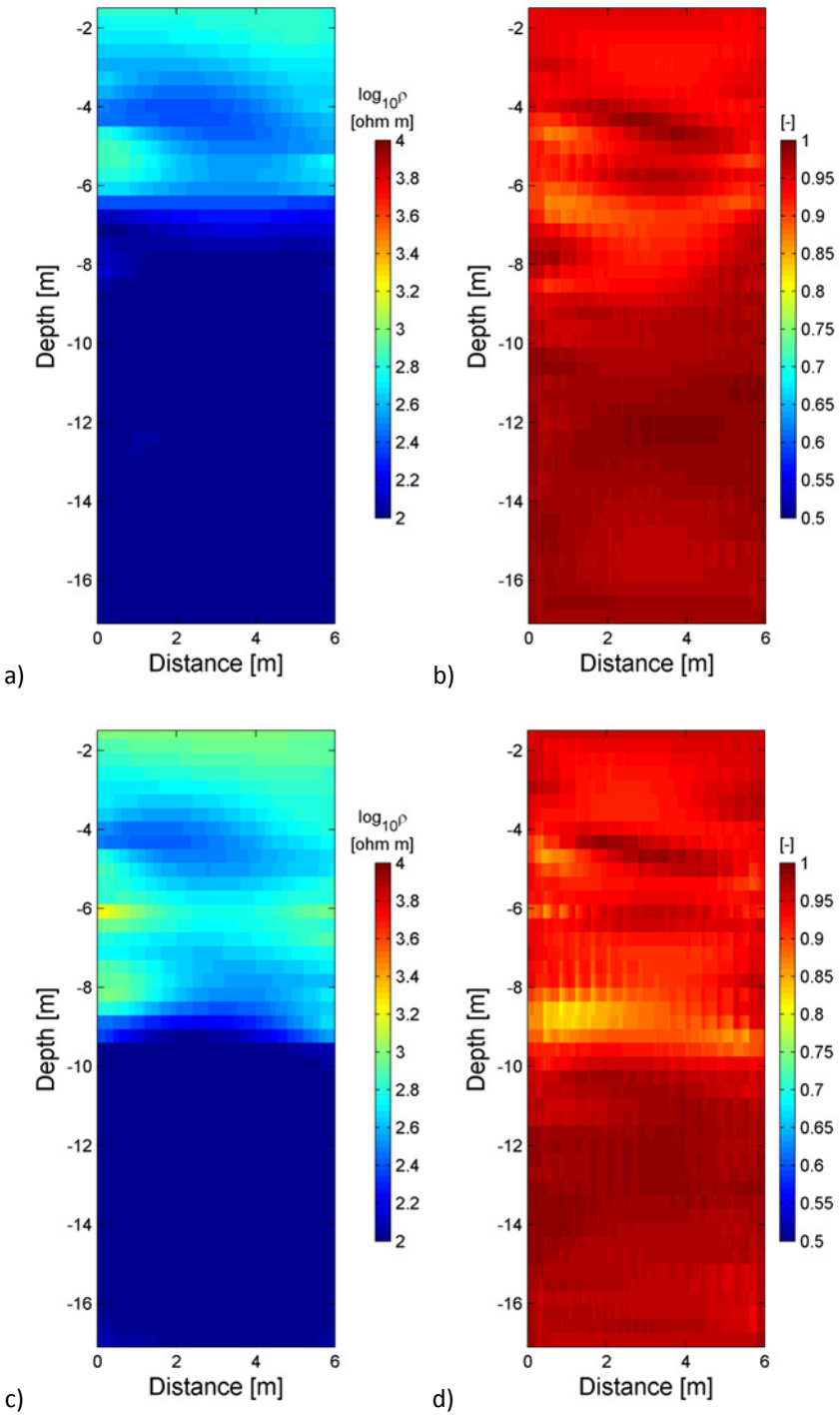

Fig. 4.9: Synthetic time-lapse model n. 2 (10% noise data), results from the SGERT inversion: image of average resistivity for the background (a) and the subsequent (c) case, precision P_0 (b) and P_t (d).

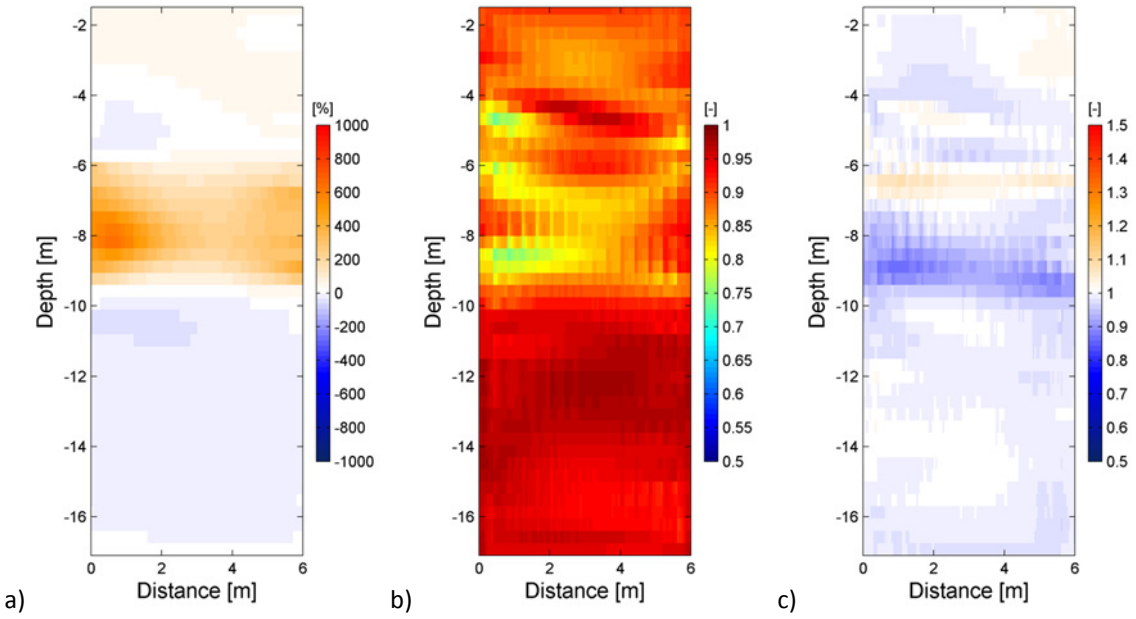

Fig. 4.10: Synthetic time-lapse model n. 2 (10% noise data), results from the SGERT inversion: image of (a) time-lapse percent resistivity difference (b) time-lapse precision P_{TL} and c) accordance.

4.4 Application to real data

The SGDERT method is applied to time-lapse data coming from Trecate site, contaminated by LNAPL after a oil-well blow out. The site is described in Chapter 2.

The resistivity changes with time at Trecate site are mainly governed by water table fluctuations. The contaminated site is located in an agricultural area characterized by an intensive irrigation activity, which starts in the early spring and terminates in the late summer. The superficial un-confined aquifer is directly influenced by this hydraulic forcing condition, with a consequent seasonal variation of the water table of 4-5 meters.

Even so, vertical aquifer recharge in correspondence of the test-site is not direct, because of a very low permeable clayey layer on the surface. It occurs through apposite infiltration pits located 100 m away from the test-site.

The time-lapse datasets herein used cover a period of time that ranges from April, 2010 to February, 2011. This is a sub-set of the whole data recorded at the site, in a time frame from August 2009 to May 2012. Four time steps are considered: April 2010, July 2010, October 2010 and February 2011. The choice of this four time-steps was made with the aim of covering 1 year period, with a with a quite homogeneous distribution of the campaigns over the four seasons. The objective of the study is to evaluate the sensitivity of time-lapse ERT in following the piezometric level oscillations and the consequent LNAPL smearing. Thus, resistivity data from the April 2010

campaign has been chosen as background, because of the lowest level of the water table at that time. Borehole direct measurements placed the water depth at 10 m from the surface.

Results from the SGERT inversion of the April 2010 dataset are shown in Figure 4.11.

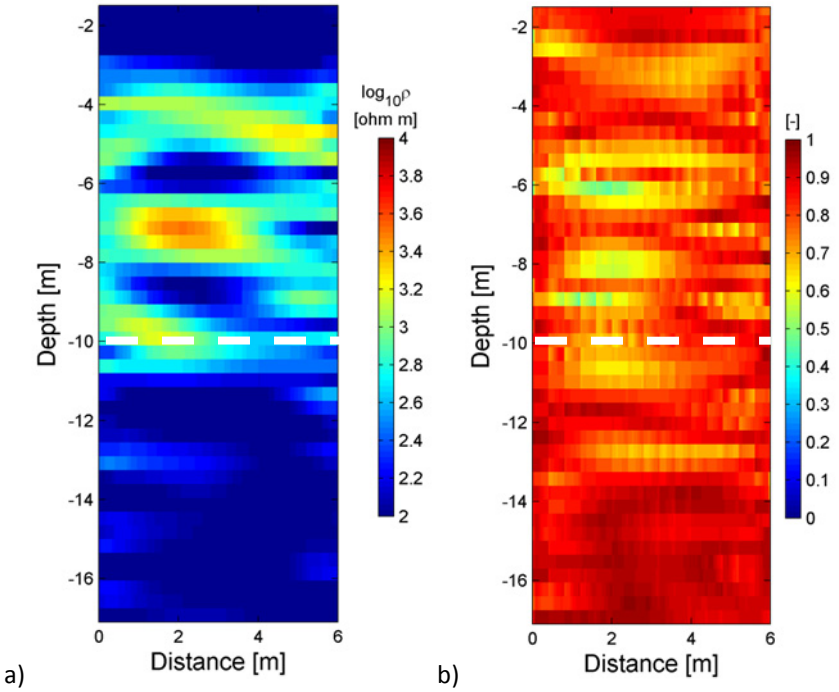

Fig. 4.11: resistivity data from Trecate site, April 2010: image of (a) averaged resistivity and (b) precision P image from the SGERT inversion. White dashed line indicates water table level. This resulting resistivity is used as background for the time-lapse inversion.

The resistivity panel in Figure 4.11 (a) points out three main resistivity horizons, one conductive layer on the top of the images, an alternance of resistive layers from 3 to 10 m b.g.l., overlying a conductive half-space. Those main layers respectively correspond to an upper silty layer, to an inhomogeneous vadose zone above the water table, and to the lower saturated zone, where no significant contamination has been found below 11 m b.g.l..

The result of the SGERT inversion on April 2010 data has been used as background for the SGDERT method, described above and applied to the datasets of July 2010, October 2010 and February 2011.

Results of the time-lapse SGDERT method are shown in Figures 4.12 to 4.17, organized as the ones from the synthetic cases.

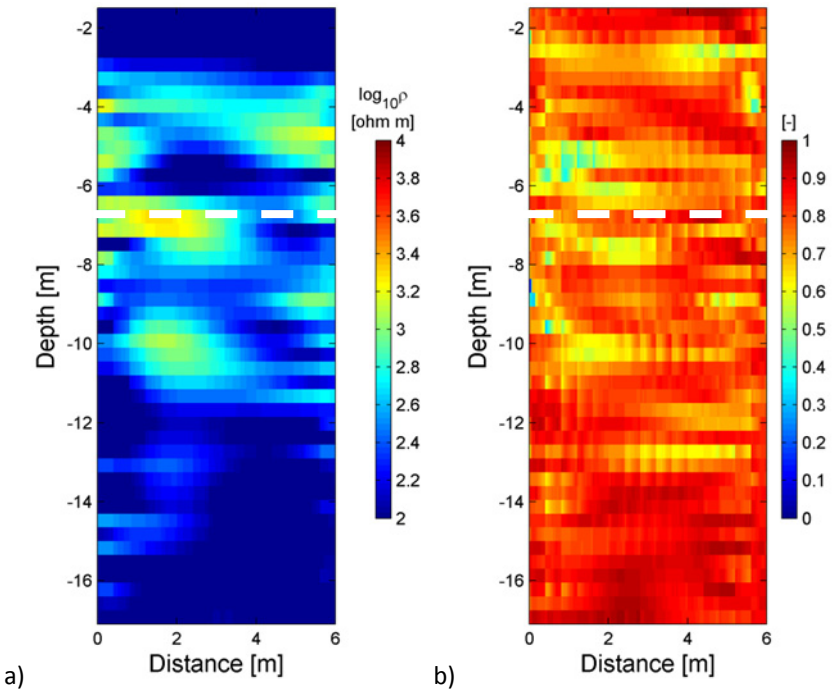

Fig. 4.12: resistivity data from Trecate site (July 2010): image of (a) averaged resistivity and (b) precision P image from the SGERT inversion. White dashed line indicates water table level.

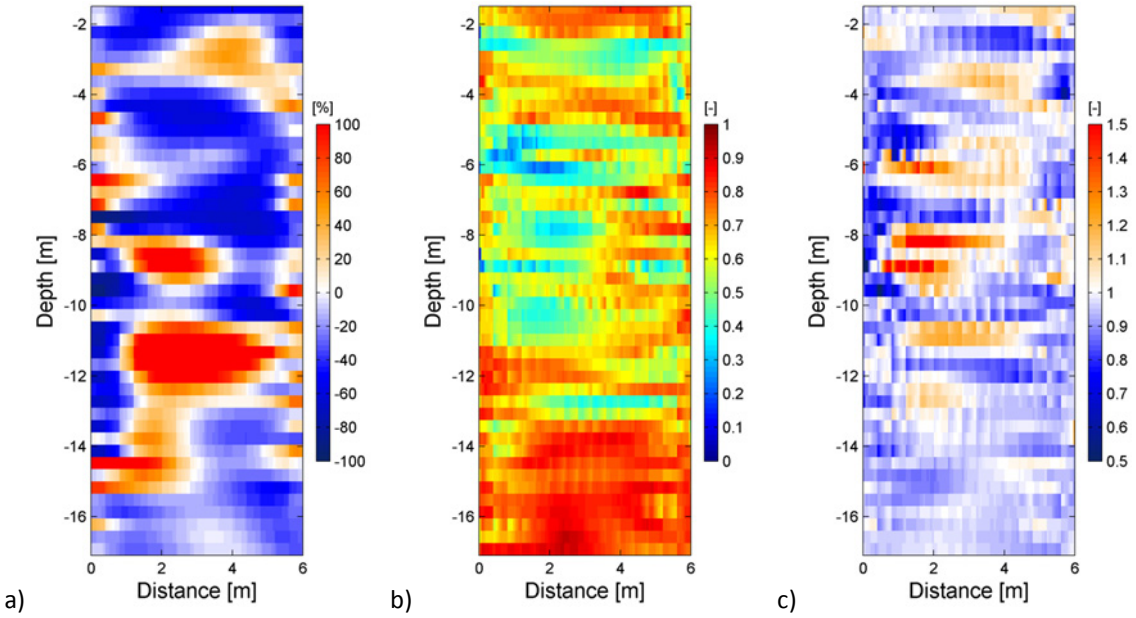

Fig. 4.13: resistivity data from Trecate site (July 2010), results from the SGERT inversion: image of (a) time-lapse percent resistivity difference (b) time-lapse precision P_{TL} and c) accordance.

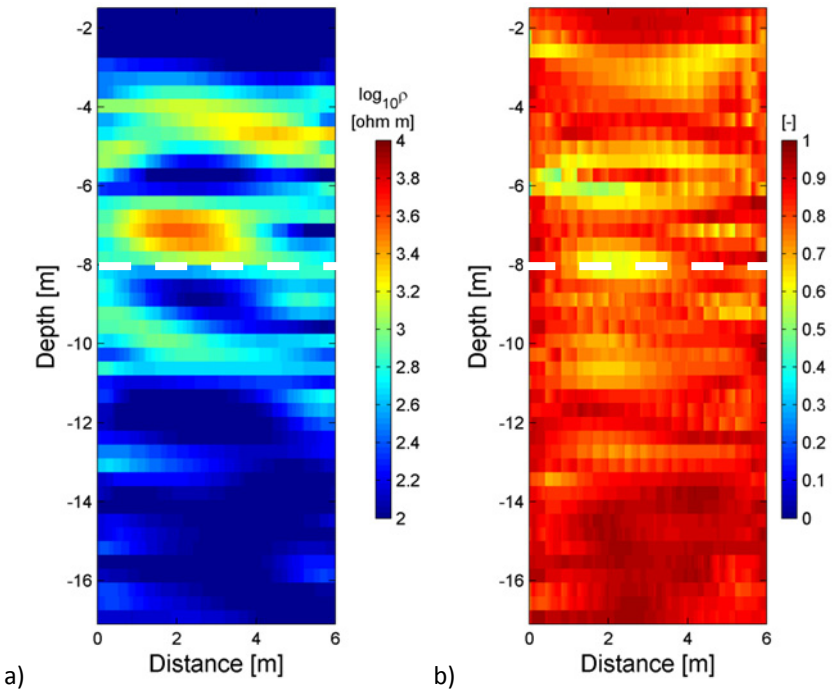

Fig. 4.14: resistivity data from Trecate site (October 2010): image of (a) averaged resistivity and (b) precision P image from the SGERT inversion. White dashed line indicates water table level.

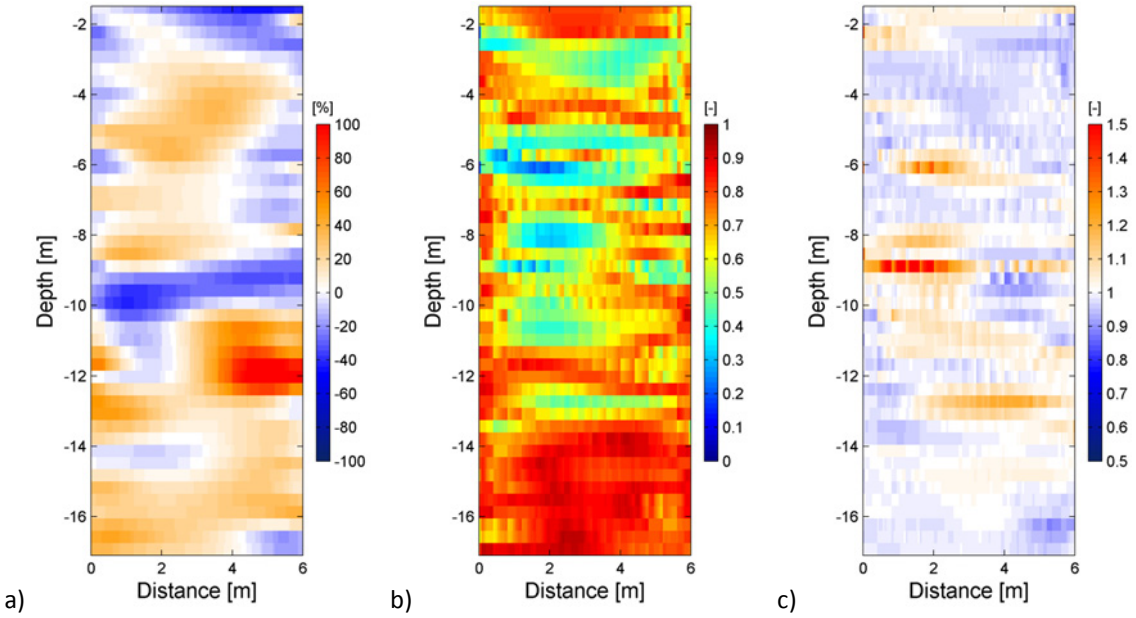

Fig. 4.15: resistivity data from Trecate site, October 2010; results from the SGERT inversion: image of (a) time-lapse percent resistivity difference (b) time-lapse precision P_{TL} and c) accordance.

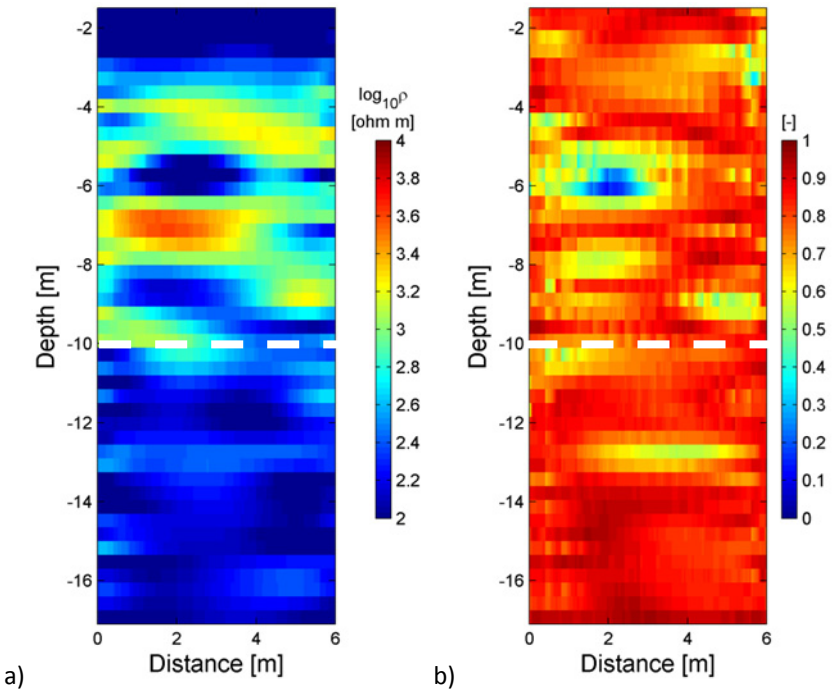

Fig. 4.16: resistivity data from Trecate site (February 2011): image of (a) averaged resistivity and (b) precision P image from the SGERT inversion. White dashed line indicates water table level.

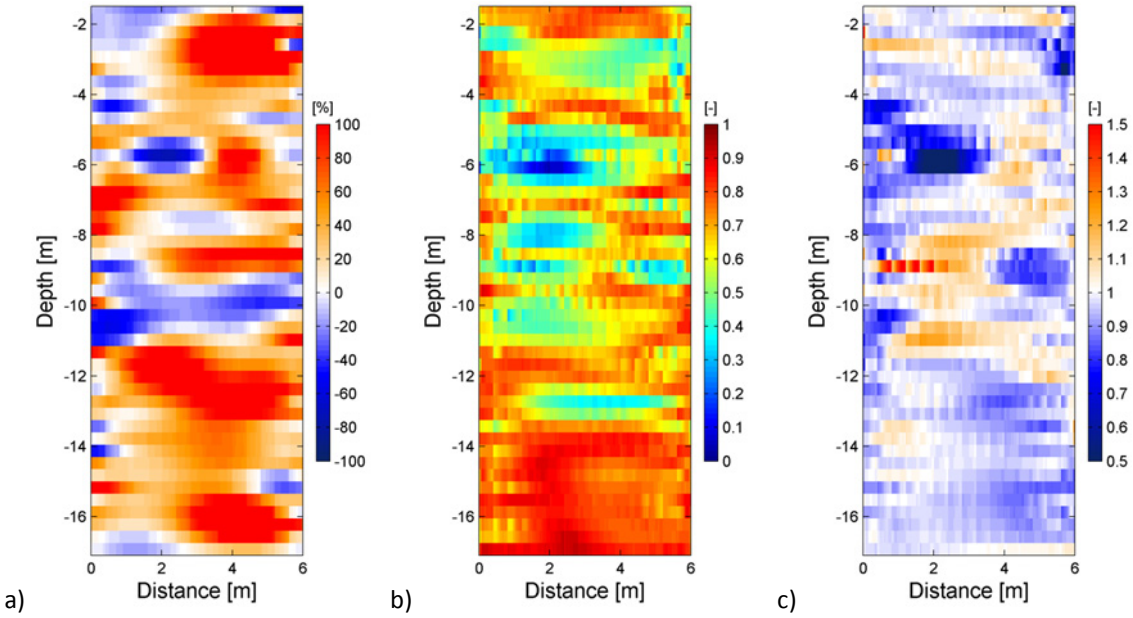

Fig. 4.17: resistivity data from Trecate site (February 2011), results from the SGERT inversion: image of (a) time-lapse percent resistivity difference (b) time-lapse precision P_{TL} and c) accordance.

Results of SGDERT inversion on the dataset of July 2010 point out that, despite a huge fluctuation of the water table, which was at 6.7 m b.g.s. at the time of the survey, the electrical properties of the saturated zone don't change significantly. In fact, a large resistive anomaly is located around

the depth of 10 m. this can't be explained by differences in the geological stratification. Deeper than 8 m (which is a layer richer in silt composition, up to 10%) the aquifer is mainly compounded by gravel and coarse sand. The most realistic hypothesis is that, considering that 11 m was the water table depth at the time the accident occurred, the oil reached this depth with no possibility to move further down. This caused the formation of a very oil-rich horizon (Atekwana et al., 2009), and the great water fluctuations created a smearing of the LNAPL. Then, in case of higher water table levels, we have a smear zone with high concentration of trapped oil; in the resistivity image this yields a resistive feature embedded in the most conductive zone (the saturated level). The time-lapse evolution of the overall geometry of the problem is also reflected in the precision and accordance distributions.

Results of dataset of October 2010 show a similar response with respect to the background case, both concerning the spatial distribution and the resistivity values (accordance values are, as a consequence, close to 1). In fact, resistivity difference is quite low, apart from the fluctuation layer between 8 and 10 m b.g.s..

February 2011 data were themselves higher, and the inversion results reflect this peculiarity. Again, the geometrical reconstruction of the resistivity strata is similar to the background case, but the resistivity value are quite high all over the section, when compared with the background values. This is reflected by the relative percent difference values, with higher resistivity value even in the deep saturated zone.

4.5 Conclusions

This Chapter has showed a novel approach for the inversion of time-lapse resistivity data, made up by combining the difference inversion algorithm (LaBrecque and Yang, 2001) and the SGERT method presented in Chapter 2.

The combination of an efficient method for time-lapse ERT inversion with a method to verify the consistency of the resulting resistivity distribution, allowed to test the reliability of the overall time-lapse inversion process. The resulting matrices are an average resistivity distribution and precision, both for the background and the subsequent dataset. Then, accompanying the relative percentage difference, the SGDERT method furnishes information about the time-lapse precision, which is obtained by Equation 4.4 as the product between the static precision for the background and subsequent cases. This parameter assumes importance in the time-lapse analysis of resistivity data, because the method allows to take into account the precision of the inversion of the background data and even its influence on the inversion of the subsequent data.

Finally, the precision accordance (Equation 4.5) can be utilized for checking the evolution of the spatial disposition of resistivity layers in the subsoil. In fact, where A_{TL} is greater than the unity, the background precision is dominating, and we can observe the geometry of the background case. Viceversa, for A_{TL} values lower than 1, precision values from the subsequent case prevail, giving an indication of the movement of the resistivity boundaries with time. This is of particular importance to point out the most significant resistivity boundaries, even when many inhomogeneities are present in the result.

The SGDERT method has been tested on two synthetic datasets, one simulating a 3m-raise of the water table (i.e. corresponding to a resistivity decrease from 1000 to 100 Ω·m) and the other simulating the opposite case (i.e. corresponding to a resistivity decrease from 100 to 1000 Ω·m). The SGDERT method worked quite well on both clean synthetic data and on resistance data added by 10% of gaussian noise. Of course, applying a data weighting matrix to account for the 10% data errors provoked a smoother result, and this was also indicated by the A_{TL} distribution. In fact, it was more difficult to highlight the true sharp resistivity boundary.

The time-lapse method was also tested on real data coming from a NAPL-contaminated site. Results from the time-lapse analysis of resistivity data collected at Trecate site give a significant contribution to the comprehension of the resistivity variation phenomena on a very challenging real situation. In fact, it was possible to verify the precision of the background resistivity model, and to check for the time-lapse precision and accordance for the subsequent cases. In this real case, precision inversion is lower than in results of synthetic data inversion, and this information has to be taken into account when making quantitative interpretation of the results.

References

Binley, A., 2010. Resistivity Software R2, profile Version 2.6 (November 2010).

Cassiani, G., Bruno, V., Villa, A., Fusi N., and Binley, A. M., 2006. A saline tracer test monitored via time-lapse surface electrical resistivity tomography. Journal of Applied Geophysics, 59, No. 3, 244-259.

Daily, W.D., Ramirez, A.L., LaBrecque, D.J., Nitao, J., 1992. Electrical resistivity tomography of vadose water movement. Water Resources Research, 28, 1429-1442.

Hayley, K., Pidlisecky, A., Bentley, L.R., 2011. Simultaneous time-lapse electrical resistivity inversion. Journal of Applied Geophysics, 75(2), 401-411.

Kim, J H., M J. Yi, S G., Park, and J.G. Kim, 2009. 4 D inversion of DC resistivity monitoring data acquired over a dynamically changing earth model, Journal of Applied Geophysics 68,522-532.

La Brecque, D. J., Yang, X., 2001. Difference inversion of ERT data: a fast inversion method for 3-D in situ monitoring. Journal of Environmental and Engineering Geophysics, 6, 83–89.

Miller, C. R., Routh, P., Brosten, T., McNamara, J., 2008. Application of time-lapse ERT imaging to watershed characterization. Geophysics, 73(3), 7-17.

Slater, L., A.M. Binley, W. Daily, R. Johnson, 2000. Cross-hole electrical imaging of a controlled saline tracer injection, Journal of Applied Geophysics, 44, pp. 85–102.

5. Integration of geophysical and geochemical data for the characterisation of biological degradation at an aged LNAPL-contaminated site

The experimental activity presented in this chapter has been carried out at Trecate site over a two year time period, from 2009 to 2011. After a preliminary geophysical characterization of the site (2008-2009), described in Godio et al. (2010), a test-site for cross-hole monitoring has been set-up in December 2008 within the most contaminated area of the site.

The test-site has been specifically designed to monitor time-lapse changes in electromagnetic properties both in the vadose and in the saturated zone. More specifically, it has been specifically designed for cross-hole ERT and GPR, and completed with two PVC screened boreholes (2" diameter), named B-S3 and B-S4 as they were installed under the framework of EU project SoilCAM. The two boreholes are 6 m spaced and reach a depth of 18 m b.g.s.. The two boreholes allow to perform cross-hole GPR surveys and even geochemical monitoring of groundwater quality, with multi-electrode probes. Each borehole addressed with 24 electrodes, 0.7 m spaced, from the depth of 1 m to 17.1 m b.g.s..

In December 2009, a multi-level sampling system has been installed in the vicinity of B-S3 and B-S4. Solinst Continuous Multi-channel Tubing (CMT) system has been set up in Jena and installed in-situ with a direct push Geoprobe device. The CMT system consists of 4 multi-channel boreholes, with 7 separate micro-tubes in each. A transect of twenty-eight sampling ports is then available for mapping vertically and horizontally the most important physico-chemical parameter of interstitial filling fluid in the saturated zone.

From the drilling of two boreholes of the CMT system, soil columns were extracted in transparent PVC liners, for laboratory characterization of lithological features, presence of contaminant and laboratory measurements of chemico-physical parameters.

In addition, microbial count analysis and in vitro growth experiments were performed to assess the presence of active colonies of hydrocarbon-degrading bacteria.

5.1. Material and methods

5.1.1 Geophysical characterization

Several geophysical surveys have been carried out at the SoilCAM test-site. More specifically, 1-D and 2-D electrical resistivity measurements have been performed on a monthly base. In-hole resistivity and IP logs were acquired shifting the quadripole along the total length of the boreholes. We used a Wenner configuration, with a=0.7 m (i.e. the electrode separation). 2-D resistivity tomography have been performed with a pole-dipole array, using the 48 electrodes along the two boreholes and a 49^{th} electrode as the remote pole, which was placed 300 m far in the eastern direction.

Measurements have been carried out with the complex resistivity device, PASI Polares, previously described in Chapter 2.

Measured resistance and phase data from 1-D borehole profiles are just transformed to apparent resistivity and phase logs, while the 2-D complex impedance data have been inverted using the framework presented in Chapter 3.

A least-squares minimization formulation is used, then the L2-norm is minimized on both the data and the regularization term of the Occam's objective function.

5.1.2 Monitoring of chemico-physical parameters in soil and groundwater samples

To better understand the small scale geophysical response at the test-site, two measurement campaigns of the major chemico-physical parameters were carried out in October 2010 and May 2011.

The analysis of soil samples involved a grain size characterization, water content measurements (and derivation of related quantities such as bulk electrical conductivity and bulk dielectric permittivity), pH, Cation Exchange Capacity (CEC) and measurements of Total Carbon (TC), Total Organic (TOC) and Total Inorganic Carbon (TIC). Analysis of metal oxides, such as Fe, Mn and Al, were also performed.

Groundwater sampling was carried out at very low flow rate with submersible double valve pumps, at the sampling ports of the multi-channel system. Each port was previously depurated from stagnant water by means of pumping several litres of water with a peristaltic pump.

To avoid oxygen exchange through air and the sample, the double-valve pumps were operated with nitrogen gas. During the second campaign some samples had to be drawn with air pressure again, due to lack of nitrogen gas. To avoid sample cross contamination, pumps and tubings were cleaned thoroughly between two sampling events in a tested procedure. Additionally to the multilevel piezometers, a well located outside the contaminated zone was sampled in order to derive the background values.

Dissolved oxygen, electrical conductivity, redox potential, pH and CO2 was analyzed on-line in flow through-cells with ion selective electrodes (WTW, Weilheim) during pumping on site. Nitrate (NO_3^-), Nitrite (NO_2^-), Sulfide (S^{2-}), Iron (Fe^{2+}), Manganese (Mn^{2+}; only for the 2nd campaign) and turbidity were determined photometrically on site immediately after sampling. Samples for laboratory analysis were kept refridgerated immediately after sampling during all time. Sulfate(SO_4^{2-}) and Chloride (Cl^-) were analysed in the laboratory with ion chromatography. The samples were filtered in the laboratory with a 0.45 µm filter with supor membrane and acidified immediately after sampling. Total organic carbon (TOC) and dissolved organic carbon (DOC) was determined as non-purgeable organic carbon. Samples were acidified immediately after sampling and DOC samples were filtered with a 0.45µm filter.

5.1.3 Microbial counts of bacteria in below-ground soil layers in Trecate

Microbial counts and growth experiments have been performed on several contaminated and uncontaminated samples from the Trecate site (Figure 5.1), in the laboratories of the RISSAC (Budapest, Hungary). Samples at different depths were analyzed in order to obtain a vertical distribution of the bacterial degrading activity.

Fig. 5.1: Location of sampling points for laboratory biological analysis.

The isolation and enumeration of soil microorganisms were performed using the dilution plate-counting technique. For each depth, two series of diluted specimens were used, for the estimation of both aerobic and anaerobic microbial components in the soil samples.

The catabolic enzymatic activity, through which is possible to infer the presence of extra-cellular enzymes and thus to verify the presence of additional sources of energy, was characterized by Fluorescent diacetate hydrolysis (FDA). FDA consists of a colourless transformation to colours fluorescein by both free and membrane-bound bacterial enzymes. FDA hydrolysis was measured because it is related to general microbiological activity, as stated by Villányi et al. (2006). Furthermore, the measure of FDA activity provides a description of the microbiological state of the soils, and can be compared to the amount of the contaminants (Domonkos et al. 2009).

5.2 Results and discussion

We present here the results of the integrated geophysical and geo-chemical characterization at the contaminated site of Trecate.

The chemico-physical analysis points out high values of TOC (both in soil and groundwater) and DOC in the depth range between 8 to 12 m; this states a high NAPL concentration as organic substrate. Moreover, values of Fe^{++}, manganese, hydrogen carbonate exceeding background values by far, and low redox potential values were detected, indicating that a degradation activity is still in progress.

5.2.1 Borehole 1-D profiling

Results of 1-D apparent resistivity and IP logs are shown in Fig. and Fig. , for the borehole B-S3 and B-S4 respectively.

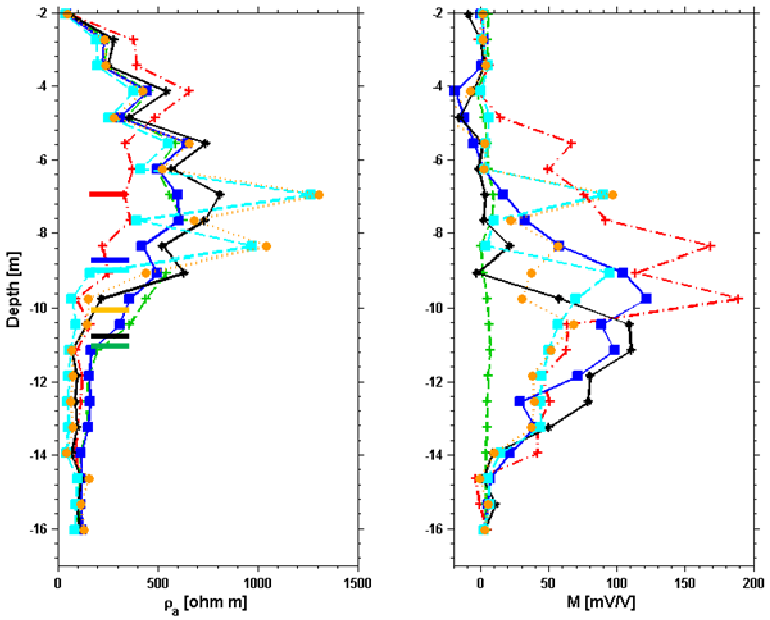

Fig. 5.2: borehole B-S3. Logs of apparent electrical resistivity (a), apparent chargeability (b). Colored bars on the right side of panel (a) indicate water table level at each time-step.

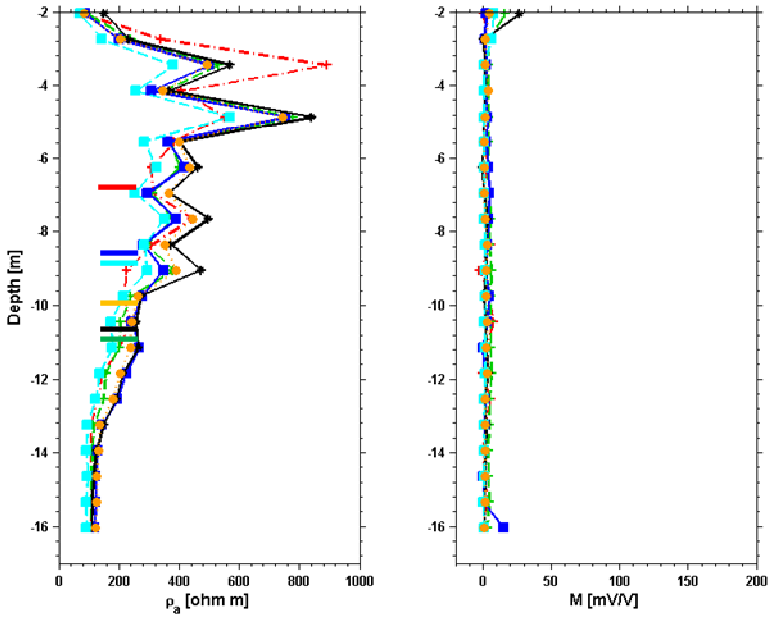

Fig. 5.3: Borehole B-S4. Logs of apparent electrical resistivity (a), apparent chargeability (b). Colored bars on the right side of panel (a) indicate water table level at each time-step.

It is clear from plots of Figures 5.2 and 5.3 that the electrical behaviour, in particular the IP response, of the two boreholes of the test-site is dramatically different.

The resistivity profiles point out three main levels:

- a conductive layer at the top, corresponding to a silty superficial layer;

- a medium resistive layer above the piezometric surface, which presents oscillations due to various fluid saturation, and probable hydrocarbon smearing;

- a conductive layer below the water table, corresponding to the saturated zone.

It has to be noted that the vertical resistivity profiles are quite insensitive of the water table fluctuations, and especially in B-S3 the resistivity values tend to decrease only below 12 m b.g.s..

IP logs show a complex behaviour, in particular along the borehole B-S3. It is reasonable to neglect IP effects encountered above the water table, because of well known capacitive effects from bad electrode-ground contact which originate anomalous and fictitious polarization responses. The main significant apparent IP anomaly is in the depth range between 8 to 12 m b.g.s.. It is interesting to notice the accordance between the position of the IP peak and the water table level.

On the contrary, almost null IP values were found in B-S4.

There is a good correlation between apparent chargeability measures and phase values from complex resistivity measurements. In Figure 5.4 an example of the application of Equation 1.12 is presented for vertical logs in borehole B-S3 (dataset acquired in February 2011). Log of apparent chargeability measured with a DC georesistivimeter (IRIS Syscal Pro) is compared to logs of apparent phase angle, measured in the frequency range of [0.5-100 Hz] with Polares. It is worthy to notice that inductive coupling effects perturb the phase measurements in the vadose zone, provoking a phase response which can't be considered indicative of the true phase values of the surrounding soil.

In the following, complex resistivity data are inverted using NES geoelectric software, in order to obtain 2-D tomographic images of the subsoil between boreholes B-S3 and B-S4.

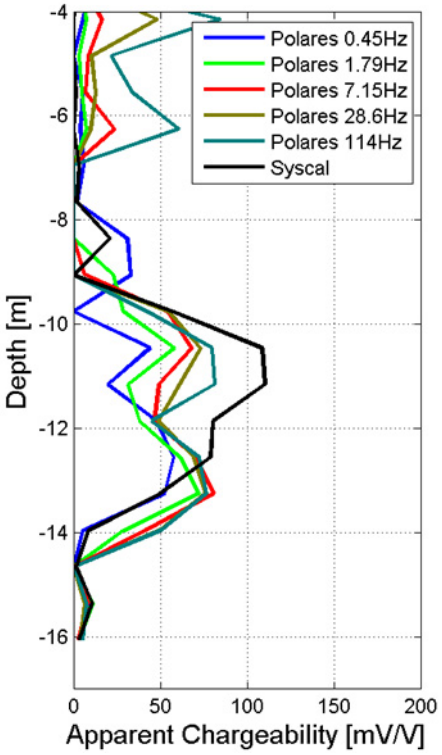

Fig. 5.4: comparative plot of vertical phase and chargeability logs (February 2011), related through Equation (1.12).

5.2.2 2-D complex resistivity tomography

2-D inversion of complex resistivity data can provided useful information of the bi-dimensional distribution of resistivity and phase in the transect between borehole B-S3 and B-S4. This can help to understand the anomalous differences in the apparent geophysical response between the two boreholes.

Inversion results, shown in Figures 5.5 and 5.6, point out a lateral variability in both the module and phase of the complex resistivity, even for the October 2010 data and for the May 2011 data.

The inversion process of the 2-D data greatly reduces the overall IP values, and the anomalies in B-S3 are in the order of -10 mradians, in the depth range between 6 to 10 m.

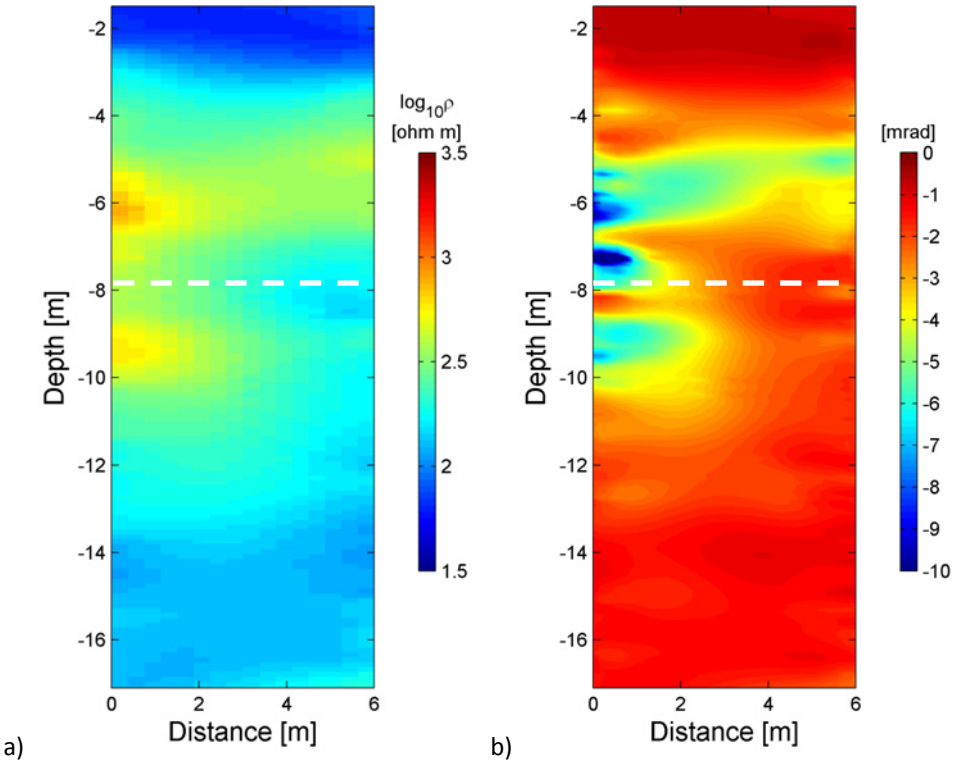

Fig. 5.5: October 2010. Module (a) and phase (b) of the complex resistivity (1.79 Hz) distribution at Trecate site. The white dashed line indicates the level of the piezometric surface.

The resulting map of complex resistivity for the dataset of May 2011 shows a relatively more prominent phase response, with a phase anomaly extended at a depth of 12 m b.g.s.. It is interesting to notice that the groundwater level is almost the same for the two campaigns, but the global electrical properties in the section is different between the two time series. This is mainly due to the fact that, after a maximum depth of 11 m b.g.s. reached at the end of February

2011, the piezometric level is being forced to raise as a consequence of the abundant amount of water used for irrigation of the fields.

This huge rise produces the so-called “smearing” of the free phase of the hydrocarbon, and is responsible for the origin of an isolated blob of trapped LNAPL (Atekwana et al., 2009). This, in addition to the recharging fresh water from irrigation, can contribute to enhance bio-degradation processes of the available organic matter (i.e., the LNAPL).

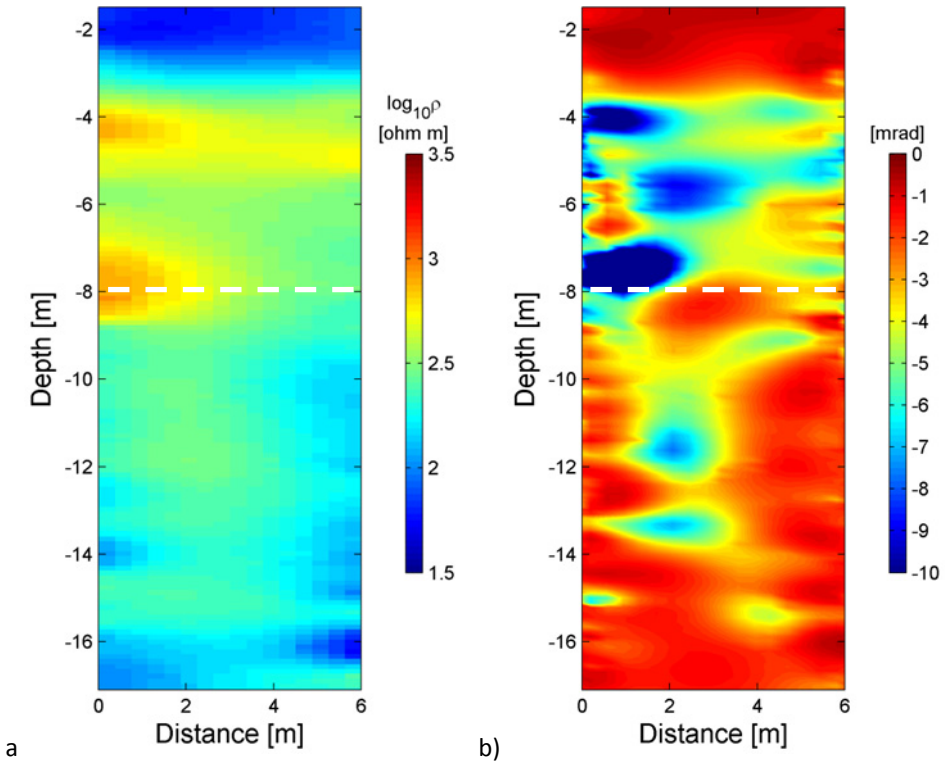

Fig. 5.6: May 2011. Module (a) and phase (b) of the complex resistivity (1.79 Hz) distribution at Trecate site. The white dashed line indicates the level of the piezometric surface.

In fact, the bulk resistivity below the water table is globally higher than in October, and a phase anomaly can be distinguished at a depth of 11 m b.g.s..

5.2.3 Distribution of chemico-physical parameters

Figure 5.7 and Figure 5.8a shows the TOC and DOC concentrations in the groundwater during three sampling campaigns in the four piezometer wells BS5 to BS8 and in the solid phase (Figure 5.8b).

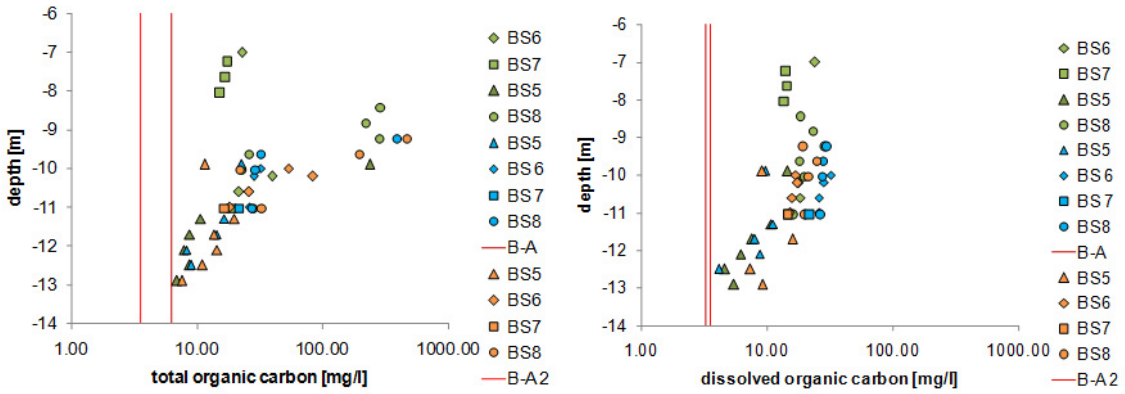

Fig. 5.7: TOC and DOC in the three sampling campaigns (green 1st , blue 2nd and yellow 3rd campaign) in the four wells. The background values are indicated by the wells in the uncontaminated location. The first campaign is not treated in the integrated analysis (Courtesy M. Wehrer, Jena).

The difference between TOC and DOC in the groundwater is a good representative of free phase oil in the groundwater. Figure 5.6 shows that it is obviously located in large amounts in depths of around 8.5 m to 10m on each of the three campaigns. On campaign 2 and 3, this depth is just below the groundwater level, during campaign 1 groundwater level is more than 1.5m higher. Obviously, a large amount of oil remains in place, despite the large groundwater fluctuations. The buoyancy of the oil in the groundwater is not large enough that the oil floats on top of the water level. It is also not completely trapped as residual phase, because in the depths from 8.5m to 10m free phase oil was discovered. It is important to note that the large TOC concentrations are quite variable and depend very much on the pumping conditions, so it is difficult to delineate and amount of free phase present in the groundwater.

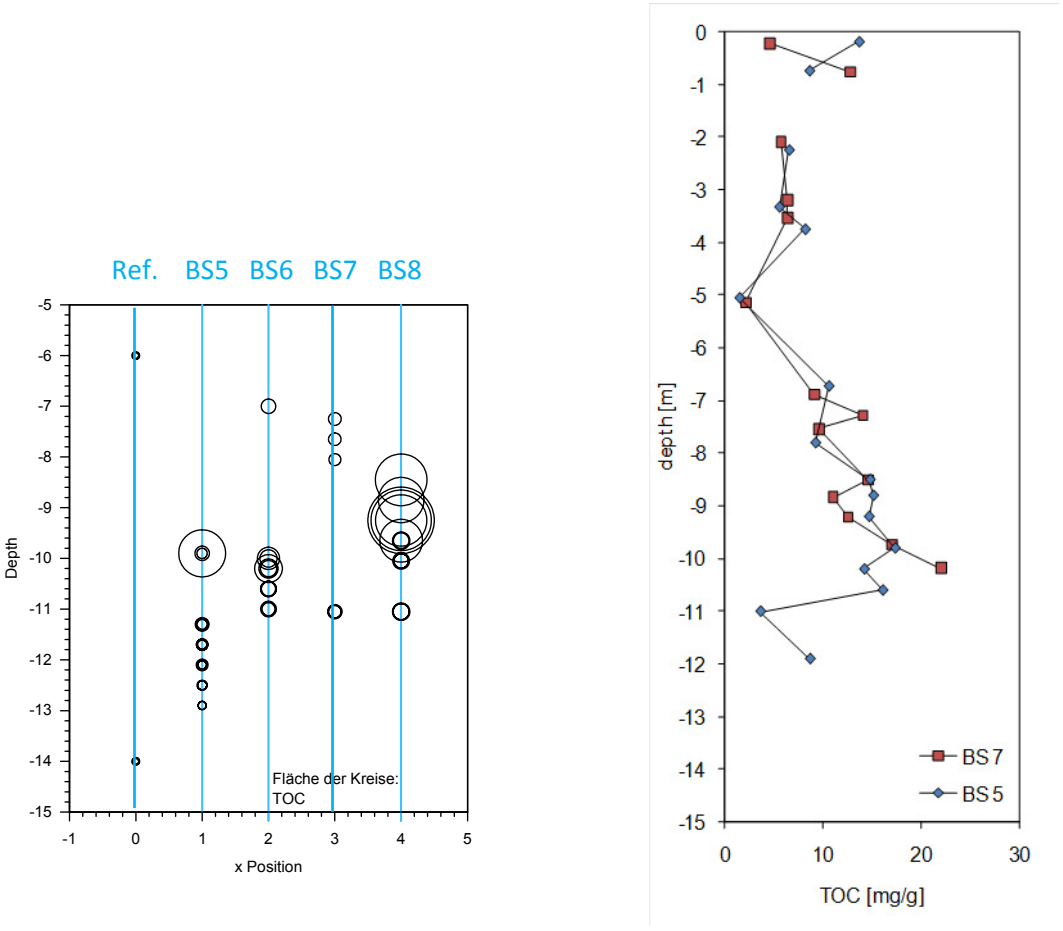

Figure 5.8: TOC a) in the groundwater in the ports of BS5 to BS8 on three sampling campaigns and b) in the solid phase of liners from BS 5 and BS 7. Area of the circles corresponds to TOC concentration in mg/l in the pore water. Background values were measured in the uncontaminated location, about 200m distance far (Courtesy M. Wehrer, Jena).

Below 10 m the amount of free phase is greatly reduced with a quite sharp boundary and most of the hydrocarbons are present as dissolved phase (at least droplets<0.45µm) with diminishing concentrations towards deeper zones. The depth of 10m also coincides with the groundwater level beginning of February, which was the month when the oil blowout occurred. It seems that the present situation is still highly influenced by the initial conditions of the spreading oil immediately after the blowout. From Figure 5.8a) it can be assumed that the extension of the residual NAPL phase may be located more in the direction of well BS8. However, the data is a little sparse for such a conclusion. Figure 5.8b shows that TOC concentrations in the solid phase (which correspond to NAPL contamination in deeper layers) generally correspond to the TOC concentrations measured in the groundwater. It seems, however, that the layer of oil contamination is spread over a larger area than 8.5m to 10m. It may be that the groundwater

concentrations reflect rather the presence of free phase oil, while from the solid phase concentrations alone it is not possible to distinguish trapped NAPL and free phase.

Generally, degradation of hydrocarbons results in the production of CO_2, when hydrocarbons are completely mineralized. CO_2 dissolves in water and forms carbonic acid, which dissociates into protons and hydrogen carbonate (measured as Total Inorganic Carbon). This lowers the pH and increases the electrical conductivity of the pore water. Also, other ionic species are produced during oxidation of hydrocarbons by different electron acceptors. First, oxygen and nitrate are depleted. Then, manganese and iron oxides are reduced, which results in the production of manganese and iron ions. Subsequently, sulfate is reduced to sulfide species and finally methanogenic conditions may occur. The occurrence of the relevant species is shown in Figure 5.9.

It can be seen that the microbiological activity results in most pronounced changes of the geochemistry in the depths from 8.5m to 11m. In this area, the microbial activity leads to a change of conductivity of the pore water, which may be observable by ERT. More pronounced than for TOC, it seems that the zone of largest activity is shifted towards BS8 (Figure 5.9). However, the whole observed aquifer is affected, which can be seen in redox sensitive species and also in the redox potential. Concomitantly to the production of TIC, the redox sensitive species iron and manganese show their most pronounced increases in the depths from 8.5m to 11m. Shown are the concentrations of total iron, which is mostly Fe^{2+}. Manganese is not shown here but it is highly correlated with iron. Nitrate and nitrite (both not shown here) are mostly below detection limit and sulfate concentrations are greatly reduced compared to the background concentration, almost over the entire depth of the water column (not shown). Only small amounts of sulfide were detected, which cannot explain the missing sulfate. It seems that other reduced sulfur species are more abundant, for example HS^- or H_2S, which is to be expected at a circumneutral pH. Consequently, the conditions can be characterized as ferrogenic on the limit to sulfidogenic.

Figure 5.9 show a data interpolation of the most relevant chemico-physical parameter of the contaminated groundwater:

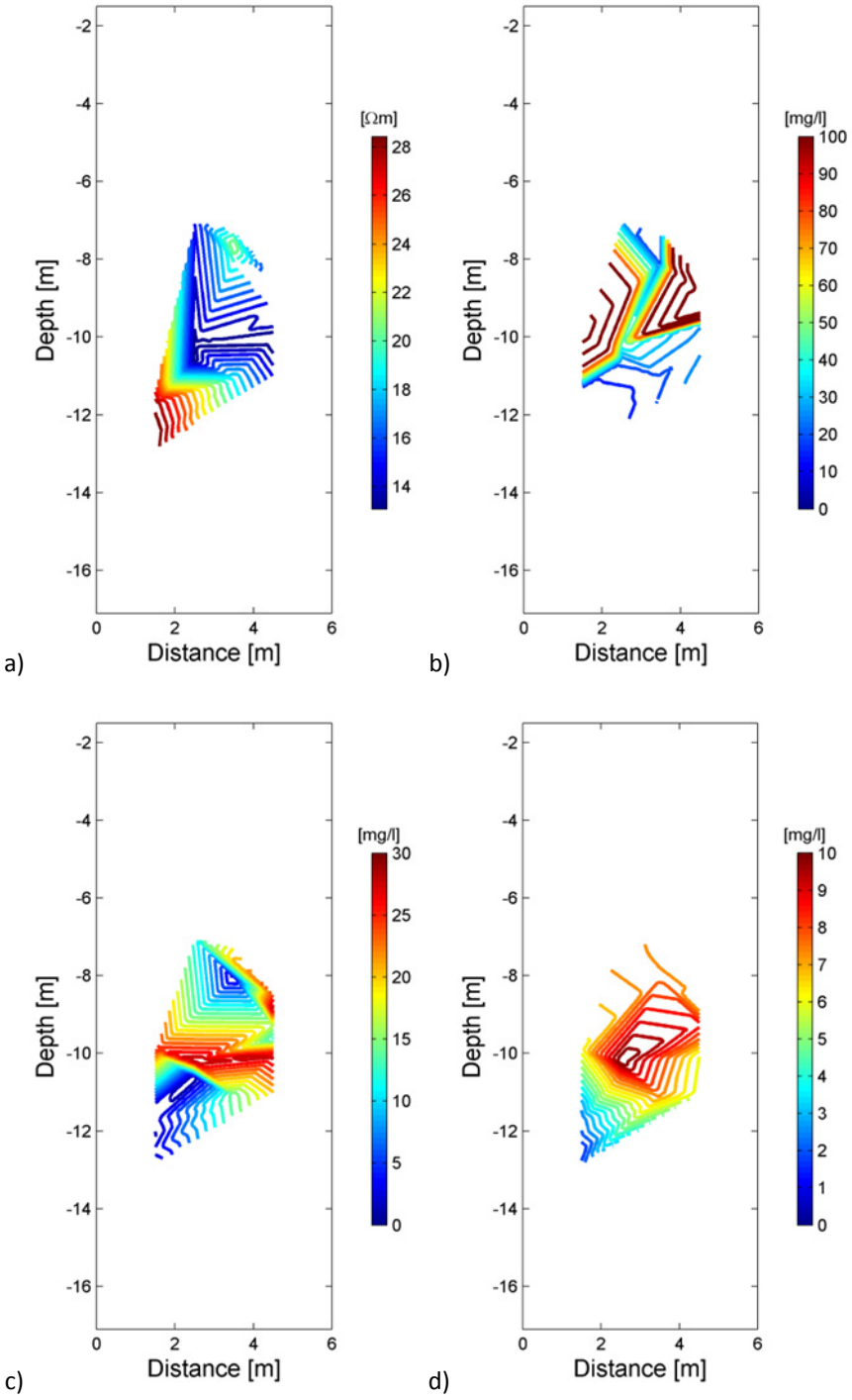

Fig. 5.9: 2-D interpolation from punctual data of a) specific resistivity, b) TOC concentration, c) Fe++ ion concentration and d) Mn++ concentration.

5.2.4 Microbial Counts

Results of microbial counts are presented for the sampling position S1 and S4, respectively located outside the contaminated area and in the vicinity of the test-site used for geophysical and geochemical monitoring. Figure 5.10 and Figure 5.11 show respectively the microbial counts for both the aerobic and anaerobic microbes.

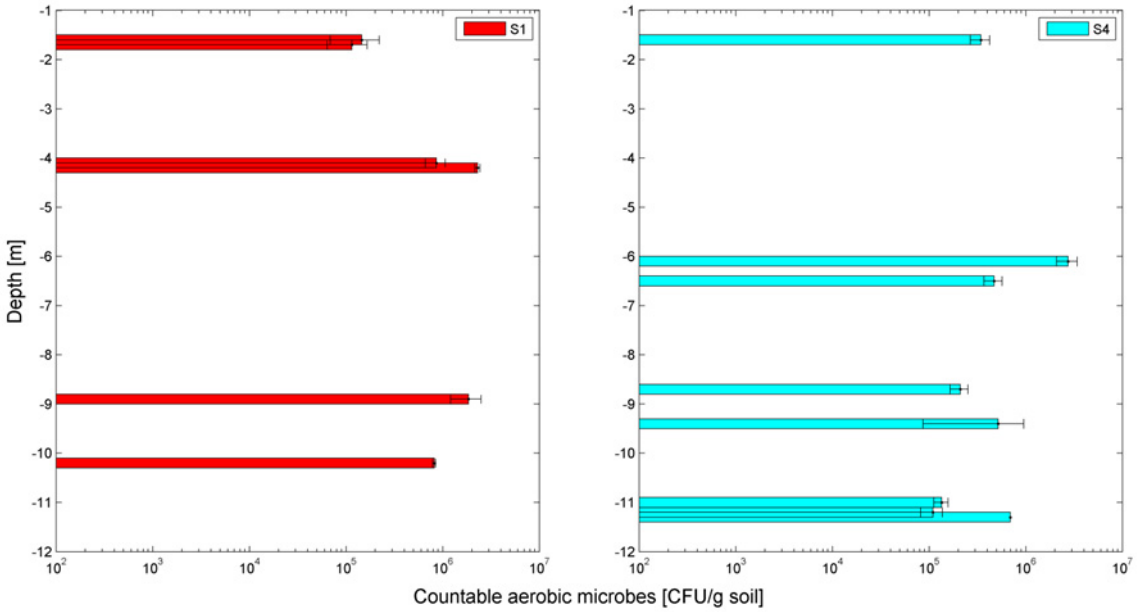

Fig. 5.10: Colony Forming Units for aerobic microbes, measured at different depths in the sampling point S1 (left) and S4 (right) (Courtesy B. Biró, RISSAC, Budapest).

From the bar-plot of Figure5.10 it is clear that no significant differences on aerobic microbe CFUs can be found in S4 with respect to the uncontaminated location. More interesting is the information coming from counting of anaerobic biomass colonies, in Figure 5.11. The production of metallic ions is indicative of anoxic, and anaerobic, conditions and then anaerobic bacteria find in this reductive environment optimal place to grow. Anaerobic CFUs are more than two order of magnitude greater than the anaerobic CFUs in the control location.

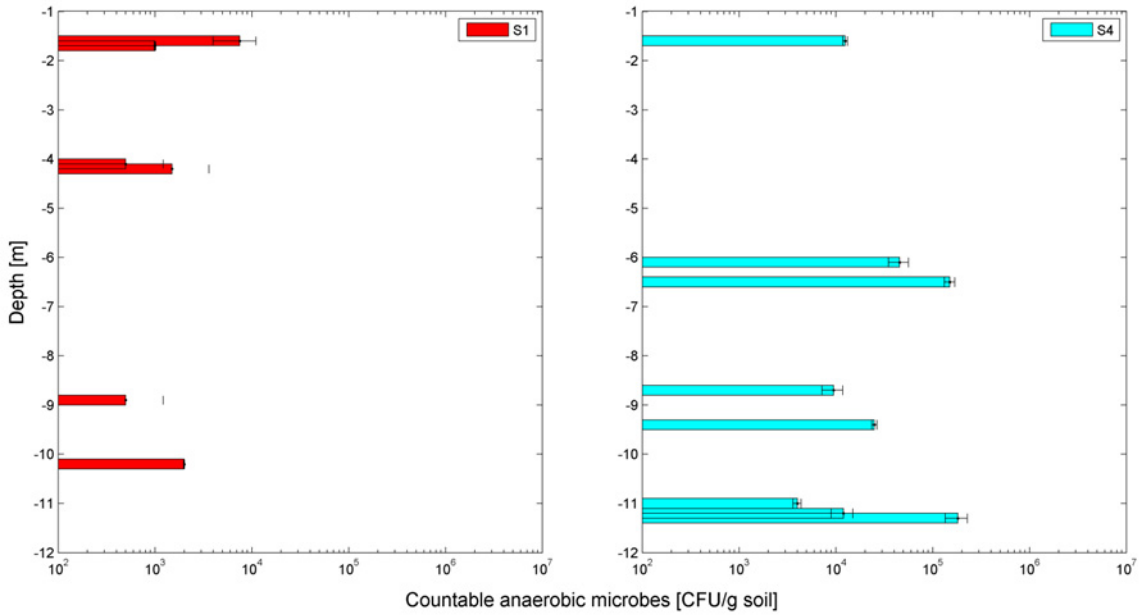

Fig. 5.11: Colony Forming Units for anaerobic microbes, measured at different depths in the sampling point S1 (left) and S4 (right) (Courtesy B. Biró, RISSAC, Budapest).

The results of FDA analysis , presented in Figure 5.12, are important to check whether the soil condition are favorable or not for a conspicuous bacterial growth. The amount of fluorescein produced in the analyzed samples, which is related to the presence of additional energy sources (in this case the contaminant), is 10 times greater in the deeper samples of S4. The depth range between 6 to 11 m depth corresponds in fact to the hydrocarbon smearing zone.

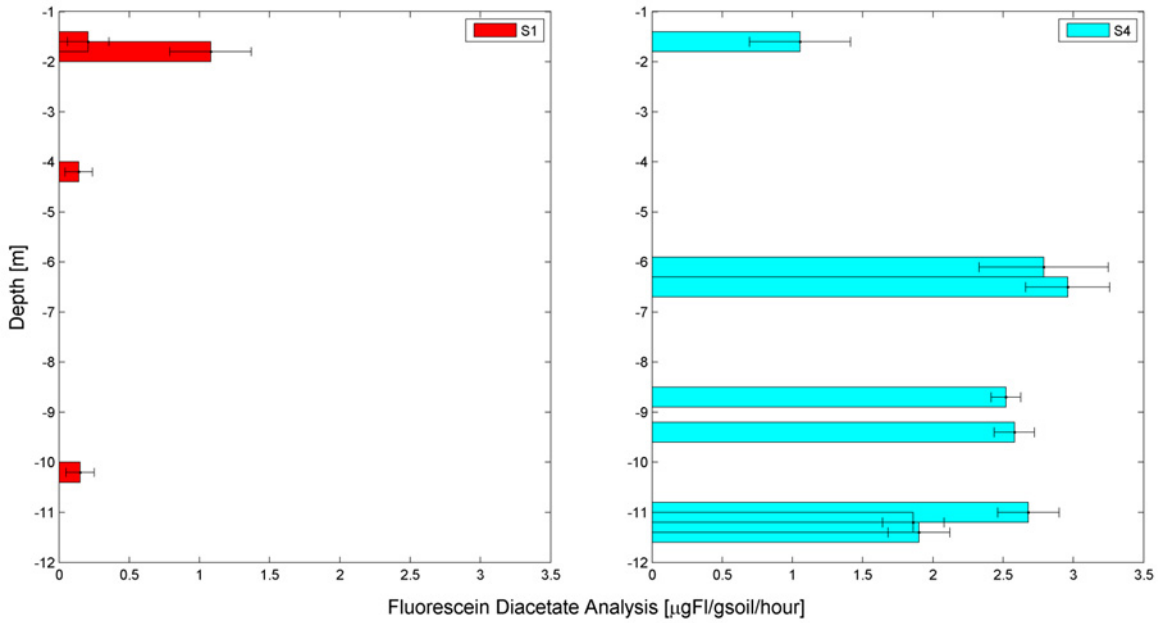

Fig. 5.12: Fluorescein Diacetate Analysis, measured at different depths in the sampling point S1 (left) and S4 (right) (Courtesy B. Biró, RISSAC, Budapest).

5.3 Conclusions

The integrated characterization of the hydrocarbon-contaminated site of Trecate permitted to achieve a complete knowledge of the various and complex phenomena which are undergoing at the site. The results of the geophysical surveys (both ERT and vertical resistivity and IP logs) pointed out anomalous response in the saturated upper saturated zone, in the depth range between 8 to 11 m b.g.s.. Despite an expected resistivity decrease, and low IP values, the tomographic survey pointed out an altered zone, whose values are neither dependent on different geological features nor on differences in fluid saturation. The zone is then interested by huge water fluctuations during on a yearly base, responsible for the smearing of the free hydrocarbon phase which is present in a huge amount.

This hypothesis coming from the interpretation of the geophysical characterization was in good agreement with the results of the chemico-physical monitoring. It demonstrated, through the measure of the Total Organic Carbon and the Total Petroleum Hydrocarbons, that the smearing zone is the most contaminated level at the site, and that those products serve as additional source for biological degradation. From a chemical point of view, this has been addressed by the presence of metabolic by-products such as Fe++ and Mn++, in an anoxic and reductive environment. The results of micro-biological laboratory analysis come to support this thesis,

indicating that the smearing zone is rich of anaerobic bacteria. Both CFUs and enzymatic activity tests pointed out that there is an abundance of microbial communities and that the smearing zone is rich of additional organic matter for the bacteria to proliferate.

References

Domonkos, M., 2009. Vertical and horizontal evaluation of pollutants in airport soils. (Szennyezőanyag vertikális és horizontális értékelése repülőtéri talajban). Diploma work, University Szent István, SZIE MKK, Gödöllő. (in Hungarian).

Godio, A., Arato, A., Stocco, S., 2010. Geophysical characterization of a nonaqueous-phase liquid–contaminated site. Environmental Geosciences 17, pp. 141-162.

Villanyi, I., Füzy, A., Angerer, I., Biró, B., 2006. Total catabolic enzyme activity of microbial communities. Fluorescein diacetate analysis (FDA). In: Understanding and modelling plant-soil interactions in the rhizosphere environment. Handbook of methods used in rhizosphere research. Chapter 4.3. Microbiology, Biochemistry and molecular biology. p. 441-442.

CONCLUSIONS

Besides the traditional usages, such as mineral exploration and hydrogeological characterization, electrical resistivity and induced polarization methods are widely accepted for being, amongst the large number of geophysical techniques, the most suitable for environmental applications. In fact, due to their sensitivity to pore fluid saturation and interstitial fluid composition, at small to medium scale, and thanks to their capability to stimulate “induced” responses in soils, fluids and in the living part of the subsoil (i.e., the microorganisms), they are usually preferred for the characterization of contaminated sites. Also, a new branch of geophysics, called “bio-geophysics”, gained a great popularity in the last decade, utilizing electrical and electromagnetic methods to infer the bio-degradation processes which undergo at contaminated sites.

The research activity presented in this thesis has been focused on the application of electrical and electromagnetic techniques for geological, hydrological and environmental characterization of contaminated sites, with particular attention on hydrocarbon contamination.

In this context, one of the purposes was to improve the reliability of the information resulting from geophysical inversion, when used to support integrated characterization and/or remediation strategies. Then, innovative approaches have been developed with the aim of reducing the possible non-uniqueness of the solution of the geophysical inverse problems. Knowing that, by definition, geophysical inverse problems are ill-posed and ill-conditioned, we worked on the possibility to check for the consistency of the resulting resistivity image, coming from various inversion on different FEM grids on the same dataset. The main goal of the Staggered Grid Electrical Resistivity Tomography (SGERT) approach is actually to improve the reliability of the inversion by enhancing the S/N ratio and preserving, in the largest part of the domain, the conditioning of the selected inversion scheme. Stated that the resistivity value has to be constant in each element of a FEM mesh, the grid staggering has a different effect on homogeneous resistivity zones and in correspondence of high-gradient limits. Furthermore, the averaging operation allows to reduce the formation of possible inversion artifacts. The standard deviation distribution, pixel per pixel, permits to evaluate the reliability of the resulting resistivity distribution, and to highlight the presence of the predominant resistivity boundaries. In fact SGERT, presented in chapter 2, has been shown to be a useful technique for site characterization.

SGERT has been also applied to time-lapse resistivity data, jointly with the advantages of the difference inversion algorithm proposed by LaBrecque and Yang (2001). Difference inversion is computationally efficient and it has been demonstrated to provide good results in many different situations, both in cases of slowly changing environments and when the data differences reflected huge variations in the geo-electrical properties of the subsoil. The combination of difference inversion and SGERT gives the possibility for the user to check the static and time-lapse precision of the results, by analyzing the precision and accordance information. The first one indicates the level of repeatability of the inversion result on the different grids, while the second one can be used to interpret the spatial (i.e. geometrical) changes of resistivity distribution over time. Those two parameter can be effectively used when quantitative information has to be retrieved by geo-electrical measurements.

Another approach has been developed with the aim of improving the robustness of the inversion procedure, in terms of sensitivity to the presence of outliers in the data and of a more rigorous solution of the direct problem. A novel software for inversion of complex resistivity data, based on the Primal-Dual Interior Point formulation, has been tested in Chapter 3 on both synthetic and real datasets. The software allows a mathematically flexible approach on the search for the optimal solution (i.e. the minimization of the objective function), by choosing either the L1- or the L2- norm on both the data and regularization term of the objective function to be minimized. Results confirmed that the use of L2- norm on the data term is effective on normally distributed data, and a least square regularization offers a smooth resistivity distribution. Instead, the L1-norm is much more robust in presence of outliers in the data, and its use on the regularization term acts to preserve sharp resistivity boundaries.

A more rigorous solution of the direct problem comes from the internal mesh generator, which builds triangular or tetrahedral FEMs (in 2-D or 3-D) and accounts also for the finite extent of the electrodes and the boreholes. In fact, appropriate boundary conditions have been set up on the electrode surface, from which the current is injected non-uniformly into the ground.

Moreover, the possibility to invert complex resistivity data, makes the code a useful tool for environmental characterization of contaminated sites. Imaginary part of the complex resistivity (coming from the measure of the phase shift between current and potential sinusoids) is influenced by the presence of polarizing materials (such as silt and clay), degradation by-products and the degrading activity of the present microbial communities.

In the last Chapter, the integrated characterization of the hydrocarbon-contaminated site of Trecate is treated. Geophysical, chemico-physical and biological methods are combined together to provide a complete description of the contamination and of the bio-degradation phenomena

occurring at the site. In-hole logs and 2-D resistivity and IP sections have been used to map the distribution of electrical properties in the subsoil, at metric scale. To support the geophysical anomalies, measures of the most relevant chemico-physical parameters, such as Total Organic Carbon, Total Petroleum Hydrocarbon, iron and manganese ions, have been carried out. High values of Total Petroleum hydrocarbon have been found in correspondence of the resistive anomalies, while high values of anaerobic degradation by-products gave a convincing explanation to the weird induced polarization response. Laboratory measure of biological colonies counting and enzymatic activity showed that the site is interested by a slow natural degradation of the contaminant.

The integrated characterization approach, made up by adding information from various and independent techniques, permitted to obtain a very complete description of the situation for the analyzed case study. This comes from the possibility to combine the strength and, more important, to make up the limits of the different methods.